PHOTON EMISSION IN HADRONIC EVENTS AT LEP

Michael Gordon Smith

Department of Physics and Astronomy

The University of Glasgow

Thesis submitted for the degree of

Doctor of Philosophy

September, 1994

ProQuest Number: 11007894

ProQuest 11007894

Abstract

From a sample of almost 1.2 million hadronic events collected with the ALEPH detector at LEP during 1990–92, events containing an energetic final state photon attributable to quark bremsstrahlung are selected after clustering all the constituent particles into jets and identifying photons with a fraction $z > 0.7$ of their associated jet's energy. Unlike previous analyses which used a two-step, isolation cone algorithm to select only *isolated* photons, this new 'democratic' algorithm allows the selection of photons *within* resolved hadronic jets, corresponding to emission at a much later stage of the hadronisation process. After verifying that the dominant backgrounds arising from non-prompt photons are reliably simulated by a parton shower Monte Carlo model, their contribution to the selected sample is estimated and subtracted statistically from the measured photon + n-jet rates. The quark-to-photon fragmentation function, $D_{q \to \gamma}(z)$, is then extracted directly from the measured prompt photon production rate in events comprising one 'photon' jet and one other hadronic jet. Working with an $\mathcal{O}(\alpha \alpha_S)$ matrix element calculation in the $\overline{MS}$ renormalisation scheme, the unknown non-perturbative contribution to $D_{q \to \gamma}(z)$ is determined at high z. This measurement provides a better description of quark bremsstrahlung than hitherto employed in high energy electron-positron collisions and may prove useful in describing inclusive prompt photon production at hadron-hadron colliders. Isolated photon production rates are measured as a function of the jet resolution parameter, y_{cut}. Good agreement is found with predictions from the above $\mathcal{O}(\alpha \alpha_S)$ matrix element calculation. Comparisons are also made with the rates predicted by the parton shower models JETSET, HERWIG and ARIADNE. A set of global event variables are calculated for the hadronic system in events comprising an energetic isolated photon and plotted as a function of the hadronic centre of mass energy. Comparisons are made with equivalent predictions from parton shower models where the events comprise an isolated photon and with events generated over a range of centre of mass energies.

Preface

This thesis describes a study of photon emission in hadronic events collected with the ALEPH detector at LEP during the period 1990–92.

The work of the ALEPH collaboration depends directly and indirectly on the participation of many people over a long period of time. The author's contribution to the experiment included the operation and maintenance of a laser calibration system for the time projection chamber and regular spells 'on shift', monitoring the quality of the data as it was collected.

The material presented in this thesis reflects the author's own individual analysis of the ALEPH data, developed as part of a small working group.

No portion of the work described in this thesis has been submitted in support of an application for another degree or qualification in this, or any other, institute of learning.

Acknowledgements

Contents

List of Figures

List of Tables

Chapter 1

Photon Emission in Hadronic Events

1.1 Introduction

Particle physics is the study of matter using high energy interactions to probe at increasingly smaller distance scales. The goal is to obtain a complete understanding of the ultimate constituents of matter and their interactions. A combination of theoretical predictions and experimental discoveries has led to the development of the Standard Model, a mathematical description of our current knowledge of elementary particles in terms of fields and their interactions.

1.2 The Standard Model

Quarks and Leptons

The Standard Model postulates that matter is composed of two families of structureless, spin-$\frac{1}{2}$ fermions: quarks and leptons. The fractionally charged quarks were originally invented to help explain the patterns emerging in the multitude of short-lived particles discovered during the latter half of this century. Experimental evidence that they correspond to physical entities came from deep inelastic scattering of electrons from protons, some of the electrons being deflected through large angles indicating that the structure of the proton could not be homogeneous, but must be composed of small, point-like *partons*. The leptons carry integral charge: the electron, muon and

1

First Generation

Particle	Symbol	Spin	Charge	Mass (GeV)
Electron Neutrino	ν_e	1/2	0	$< 7.2 \times 10^{-9}$
Electron	e	1/2	-1	0.51×10^{-3}
Up Quark	u	1/2	2/3	$\sim 5 \times 10^{-3}$
Down Quark	d	1/2	$-1/3$	$\sim 9 \times 10^{-3}$

Second Generation

Particle	Symbol	Spin	Charge	Mass (GeV)
Muon Neutrino	ν_μ	1/2	0	$< 2.7 \times 10^{-4}$
Muon	μ	1/2	-1	0.106
Charm Quark	c	1/2	2/3	~ 1.35
Strange Quark	s	1/2	$-1/3$	~ 0.175

Third Generation

Particle	Symbol	Spin	Charge	Mass (GeV)
Tau Neutrino	ν_τ	1/2	0	$< 3 \times 10^{-2}$
Tau	τ	1/2	-1	1.78
Top Quark (?)	t	1/2	2/3	174 ± 17
Bottom Quark	b	1/2	$-1/3$	~ 4.5

Table 1.1: The quarks and leptons of the Standard Model

tau having a charge of -1 with their corresponding neutrinos having charge 0. The fermions are grouped into three generations with remarkably similar features. Indeed, the masses of the quarks and leptons represents the only significant difference between the generations. Table 1.1 lists the quarks and leptons of the Standard Model.

The first generation contains the constituents of ordinary matter. The second and third include heavy unstable elementary particles, which can only be studied in high energy processes.

Recent precision measurements of the total width of the Z^0, measured by scanning around the resonance at LEP, have constrained the number of light neutrino generations to be three [1]. In the context of the Standard Model, this also constrains the number of generations of quarks and leptons to be three, thus leaving only the top quark remaining to be unambiguously identified, although first evidence for its production has been recently presented by the CDF collaboration [2].

Four Forces

During the nineteen-forties, the Maxwellian idea of charged particles interacting through electromagnetic *fields* was combined with the then recent developments in relativistic quantum mechanics to form the theory of Quantum Electrodynamics (QED). This *local gauge theory* (the theory is invariant under *local* symmetry transformations) describes interactions between charged fermions as an exchange of bosonic particles, the *gauge bosons* of the theory. In the case of the electromagnetic interaction, the gauge bosons are identified as photons. The coupling constant, α, which characterises the strength of these interactions is small, so perturbation theory can be safely applied to calculate cross-sections for electromagnetic processes.

$$\alpha = \frac{e^2}{4\pi\hbar c\epsilon_0} \sim \frac{1}{137}$$

Given the success of QED in describing precision measurements of the magnetic moments of the electron and muon, it was used as a model for describing the other forces or interactions which were observed between particles.

The *weak* force, which was first postulated to explain β-decays of nuclei, has also been formulated as a gauge theory, analogously to QED. The weakness of the interactions at low energies arises because the gauge bosons, the $W^{\pm}$ and the Z^0, are massive. These massive particles were introduced when the weak interaction was first developed as a gauge theory during the nineteen-sixties, and their discovery by the UA1 and UA2 experiments at CERN's SPS collider in 1983 [3] was strong supporting evidence for the theory. Within the framework of the Standard Model, the electromagnetic and weak interactions have been unified, that is described as different aspects of the same force, the *electroweak* interaction [4].

The *strong* interaction, responsible for binding quarks together to form hadrons, and in principle hadrons together to form composite particles such as nuclei, is described by the gauge theory known as Quantum Chromodynamics (QCD). This name arises from an additional quantum number assigned to quarks, *colour*, introduced to ensure that several quarks of the same flavour could co-exist in the same angular momentum state yet still obey Fermi-Dirac statistics. Quarks can have any one of three colours (and

the anti-quarks the corresponding anti-colours), while the gauge bosons of the theory, gluons, have eight possible colour states. No 'coloured' state has been observed – only combinations of quarks which are 'colourless': hadrons are composed of either a quark and a corresponding anti-quark (mesons) or three quarks, one of each colour (baryons).

Unlike the electrically neutral photons of QED, the gluons of QCD carry a colour charge themselves, thus can interact with each other through the so-called three and four gluon vertices. Whereas in QED an electron is surrounded by a polarised cloud of virtual e^+e^- pairs which 'screen' its charge (the positrons are preferentially attracted to the electron thus the 'measured' charge depends on the distance scale at which the electron is probed), the effect of the triple gluon vertex in QCD is to reverse this screening effect so, for example, a 'red' colour charge will be preferentially surrounded by other red colour charges. The net result is that the coupling constant α_s appears to decrease at small distances. This is referred to as *asymptotic freedom* – at very small distances two quarks will interact through colour fields of reduced strength and thus behave as essentially free, non-interacting particles. Only in this regime is α_s small enough for perturbation theory to be valid. Even at separations of $\sim 1\,\text{fm}$, the typical size of hadrons, $\alpha_s \sim 1$ and the quarks are tightly bound through gluon exchange. This mechanism is believed to be related to the non-observation of coloured states.

The distance scale to which a 'probe particle' can penetrate is related to its energy (higher energy particles can probe at smaller scales), thus the energy dependence of α_s can be expressed in first order by:

$$\alpha_s \left(Q^2 \right) = \frac{12\pi}{(33 - 2\text{N}_F) \ln \left(\frac{Q^2}{\Lambda^2} \right)}$$

where Q^2 characterises the energy scale of the process, N_F is the number of quark flavours which can be produced at this scale, and Λ is a 'reference' energy scale.

The quantum treatment of the fourth fundamental force, gravity, is still an open question but the Einstein field equations indicate that it should be transmitted by massless, spin-2 *gravitons*. However, although important in describing the interactions between large bodies, the gravitational force is so weak that it can be safely neglected on the scales at which nuclear and particle physics are studied.

Force	Gauge Boson	Spin	Mass
Electromagnetic	photon (γ)	1	0
Weak	$W^{\pm}$, Z^0	1	$80.1\,GeV$, $91.2\,GeV$
Strong	gluon (g)	1	0
Gravitational	graviton (G)	2	0

Table 1.2: The gauge bosons of the four fundamental forces

The gauge bosons which are believed to transmit the four fundamental forces are listed in Table 1.2.

1.3 Hadron Production in e^+e^- Annihilation

A schematic diagram of a typical multi-hadronic event arising from an e^+e^- annihilation is shown in Figure 1.1. In the first stage, an e^+e^- pair annihilates into a virtual γ^* or Z^0 resonance which subsequently decays into a $q\bar{q}$ pair. This process and its higher order corrections are well described by perturbation theory within the electroweak interactions of the Standard Model.

In the second stage, the initial quark-antiquark pair may radiate hard gluons, which in turn may radiate further gluons or split into $q\bar{q}$ pairs. This step may be described by strong perturbation theory, but since α_s is relatively large compared to α_{em} of the electroweak theory, the degree of accuracy obtained from a limited perturbation expansion is considerably less.

Stage three of the process represents the coloured partons (quarks and gluons) fragmenting into colourless hadrons. Although this mechanism should pertain to QCD, it is not perturbatively calculable, and any attempts to describe it have been through phenomenological models. The final state hadrons tend to be collimated in *jets* along the directions of the parent partons.

Finally, unstable hadrons decay producing experimentally observable particles. These can be used to determine the branching ratios of the various resonances and heavy flavour decays.
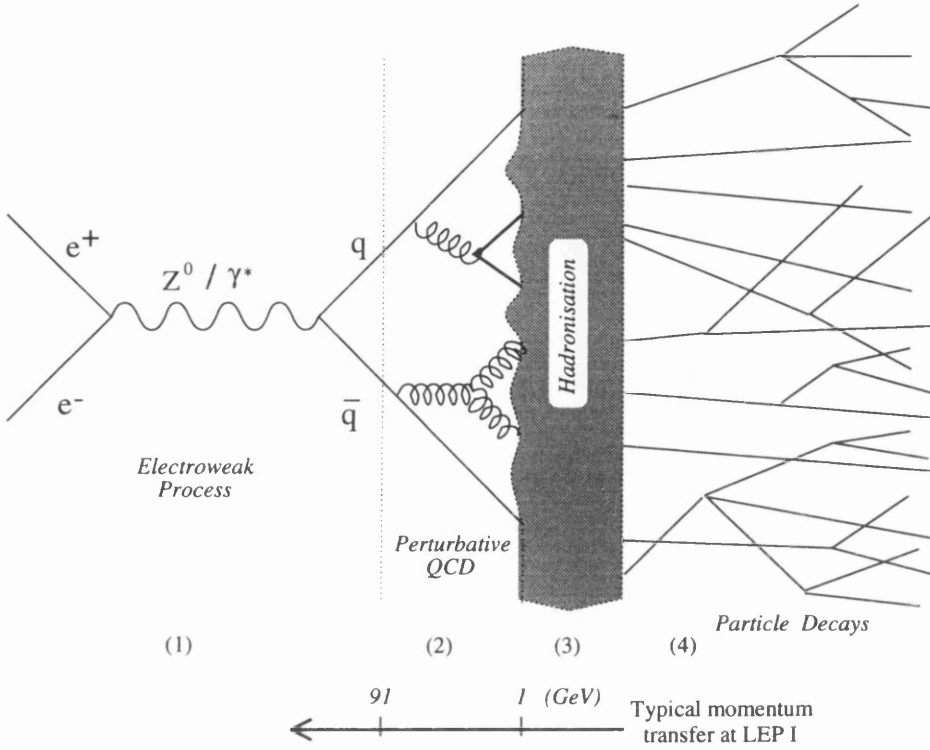
Figure 1.1: Schematic illustration of an e^+e^- annihilation event

1.3.1 e^+e^- Annihilation into Quark–Antiquark Pairs

The differential cross section to first order in QED for the production of a massless quark–antiquark pair is

$$\frac{\mathrm{d}\sigma_{q\bar{q}}}{\mathrm{d}\Omega} = \frac{N_C\alpha^2}{12s}e_e^2 e_q^2(1 + \cos^2\theta)$$

where e_q is the quark charge, $\sqrt{s}$ is the centre of mass energy and θ is the angle between the incoming electron and the outgoing quark. The colour factor $N_C = 3$ comes from the fact that quarks can be produced in any of three colour states.

The total cross section is conventionally expressed as a ratio with the $\mu^+\mu^-$ pair-production cross section:

$$R = \frac{\sigma_{q\bar{q}}}{\sigma_{\mu^+\mu^-}} = N_C \sum_{\text{flavour}=1}^{5} e_q^2.$$

The number of allowed, or *active*, quark flavours depends on the centre of mass energy;

above the $b\bar{b}$ production threshold ($\sim 9\,GeV$) five flavours are assumed.

If electroweak effects are included, the reaction may proceed via the exchange of a virtual Z^0 in addition to the photon of QED, and interference between the Z^0 and γ propagators must be taken into account. The cross section becomes

$$\frac{d\sigma_{q\bar{q}}}{d\Omega} = \frac{N_C \alpha^2}{12s} \left[a(1 + \cos^2 \theta) + b \cos \theta \right],$$

where

$$
\begin{aligned}
a &= e_e^2 e_q^2 + 2e_e e_q v_e v_q \Re(\chi) + (v_e^2 + a_e^2)(v_q^2 + a_q^2)\,|\chi|^2 \\
b &= 4e_e e_q a_e a_q \Re(\chi) + 8 v_e v_q a_e a_q\,|\chi|^2
\end{aligned}
$$

The $v_{e,q}$ and $a_{e,q}$ are the vector and axial-vector weak coupling constants respectively and χ represents the Z^0 propagator, normalised to the γ propagator

$$\chi = \frac{1}{16 \sin^2 \theta_W \cos^2 \theta_W} \frac{s}{(s - M_Z^2 + i M_Z \Gamma_Z)}$$

where M_Z and Γ_Z are the mass and width of the Z^0 resonance, $\sin^2 \theta_W$ is the weak mixing parameter and s is the square of the centre of mass energy. Terms proportional to $|\chi|^2$ in the cross section are due to Z^0 exchange and are dominant for $\sqrt{s} \to M_Z$. Terms proportional to the real component, $\Re(\chi)$ arise from the interference between the Z^0 and γ propagators.

1.3.2   Perturbative QCD

As the primary quark and antiquark move apart, interacting through gluon exchange (stage 2 in Figure 1.1) they may radiate one or more hard gluons. Such events are characterised by a number of collimated jets of hadrons in the final state. Three approaches to describing this process have been developed.

The matrix element approach, in which Feynman diagrams are calculated order by order. In principle, this is the correct approach as it includes exact kinematics with full interference and helicity structures. Figure 1.2 shows the two tree-level
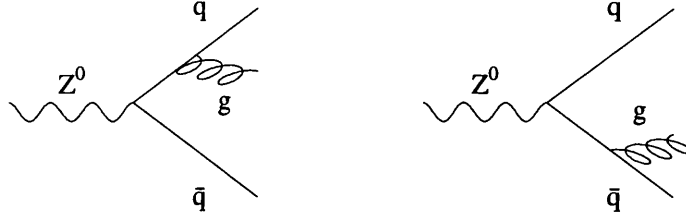
Figure 1.2: The $\mathcal{O}(\alpha_S)$ tree level diagrams for gluon emission

diagrams for gluon emission from a quark at $\mathcal{O}(\alpha_s)$ and Figure 1.3 shows some of the correction terms which must be added to these tree level processes. The number of such diagrams which must be calculated in higher order calculations increases rapidly, thus the calculations quickly become very difficult, and have only been performed to $\mathcal{O}(\alpha_s^2)$, corresponding to the production of at most two partons in addition to the primary $q\bar{q}$ pair.

In terms of the scaled energy variable, $x_f = 2E_f/E_{cms}$ (E_f is the energy of the relevant fermion and E_{cms} the centre of mass energy), the differential cross section for the process corresponding to radiation of a single gluon from a quark or anti-quark reads

$$\frac{d\sigma}{dx_q\, dx_{\bar{q}}} = \sigma_0 \frac{\alpha_s}{2\pi} C_F \frac{x_q^2 + x_{\bar{q}}^2}{(1 - x_q)(1 - x_{\bar{q}})},$$

where σ_0 is the lowest order cross section and $C_F \equiv 4/3$ is a factor representing the colour charge of a quark.

Parton shower models use simplified approximations to the full matrix element expressions, allowing an arbitrary number of parton branchings. This is done by keeping only the leading terms in a rearranged perturbative expansion; sub-
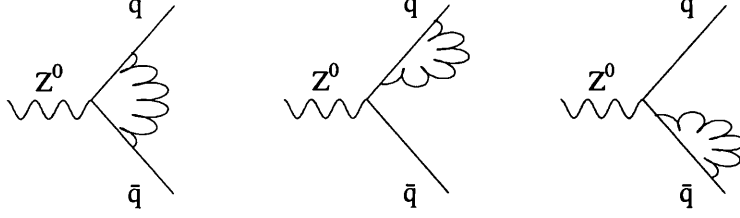
Figure 1.3: Some loop diagrams at $\mathcal{O}(\alpha_S)$

leading corrections, which are down in order by factors of $\log Q^2$ or $\log z \, \log(1 - z)$, or by powers of $1/Q^2$ are neglected (the leading-logarithm approximation). Different schemes have been devised to take into account some of the larger sub-leading corrections and it is believed that the neglected effects are small.

Most parton shower algorithms are based on an iterative use of the basic parton branchings: $q \rightarrow qg$, $g \rightarrow gg$ and $g \rightarrow q\bar{q}$. The probability, $\mathcal{P}$, of a branching $a \rightarrow bc$ occurring during an interval dt of some evolution parameter t is given by the Altarelli-Parisi equations [5]:

$$\frac{d\mathcal{P}_{a \rightarrow bc}}{dt} = \int dz \frac{\alpha_s(Q^2)}{2\pi} P_{a \rightarrow bc}(z),$$

where z specifies the sharing of four-momentum between the daughters, with daughter b taking fraction z and c taking $1 - z$. Q^2 defines the energy scale of the branching process, and $P_{a \rightarrow bc}(z)$ are the Altarelli-Parisi splitting kernels:

$$P_{q \rightarrow qg}(z) = C_F \frac{1 + z^2}{1 - z},$$
$$P_{g \rightarrow gg}(z) = C_A \frac{(1 - z(1 - z))^2}{z(1 - z)},$$
$$P_{g \rightarrow q\bar{q}}(z) = T_R \left(z^2 + (1 - z)^2 \right),$$

with $C_F = 4/3$, $C_A = 3$ and $T_R = n_f/2$, *i.e.* T_R receives a contribution of $1/2$ for each allowed $q\bar{q}$ flavour. The branching of a parton is stopped when t becomes less than some cut-off, $t_{\min}$.

The colour dipole model supposes that the initial $q\bar{q}$ pair is a colour dipole and that gluon emission from either of the initial partons can be represented as radiation from the dipole [6]. Subsequent emission of a softer gluon is assumed to be radiation from one of two independent dipoles, one joining the quark to the gluon and the other between the gluon and the antiquark. This is generalised so that emission of a third, again softer, gluon is given by three independent dipoles, *etc.* The dipoles can be thought of as forming links in a chain, such that one gluon connects two dipoles and one dipole connects two partons. Three distinct dipole types are thus possible: quark–antiquark, quark–gluon and gluon–gluon. The cross section for gluon emission from each is given by the corresponding first order matrix element:

$$\mathrm{d}\sigma_{q\bar{q}\to qg\bar{q}} \; \propto \; \frac{2\alpha_s}{3\pi} \frac{x_q^2 + x_{\bar{q}}^2}{(1 - x_q)(1 - x_{\bar{q}})} \mathrm{d}x_q \, \mathrm{d}x_{\bar{q}}$$

$$\mathrm{d}\sigma_{qg_3\to qg_2 g_3} \; \propto \; \frac{3\alpha_s}{4\pi} \frac{x_q^2 + x_{g_3}^3}{(1 - x_q)(1 - x_{g_3})} \mathrm{d}x_q \, \mathrm{d}x_{g_3}$$

$$\mathrm{d}\sigma_{g_1 g_3\to g_1 g_2 g_3} \; \propto \; \frac{3\alpha_s}{4\pi} \frac{x_{g_1}^3 + x_{g_3}^3}{(1 - x_{g_1})(1 - x_{g_3})} \mathrm{d}x_{g_1} \, \mathrm{d}x_{g_3}$$

This emission procedure is iterated until the transverse momentum of radiated gluons is less than a predefined cut-off.

1.3.3   Hadronisation Models

As mentioned above, the transformation of partons to hadrons can only be described using phenomenological models. The most simple, but nowadays outdated, is the *independent fragmentation* model [7], which gained widespread popularity with the paper by Field and Feynman [8]. The fragmentation of a system of partons is described as an incoherent sum of independent fragmentation procedures for each parton separately. Each outgoing quark generates a chain of secondary quark-antiquark pairs: at each

step a meson is formed comprising the initiating quark and one of the newly generated quarks, with the chain being continued by the remaining quark. Baryons are formed by occasionally generating a pair of 'di-quarks' (a qq and a $\bar{q}\bar{q}$) instead of a quark-antiquark pair. Once the energy of the remaining quark becomes too low to produce a futher $q\bar{q}$ pair, the branching chain is stopped. Within the model there is, however, no unique recipe for handling gluon jet fragmentation. One possibility is to treat it exactly like quark fragmentation, with the initial flavour chosen at random; another is to split the gluon jet into a pair of parallel quark and anti-quark jets and fragment these separately. Models based on independent fragmentation do not generally reproduce the data well; for instance, the expected softer fragmentation of gluon jets is not well described, nor is the particle flow between the jets of hadrons.

A more successful approach is the *string fragmentation* model [9]. This is based on the *linear confinement* of QCD at large distances — the energy stored in the colour dipole field between two colour charges increases linearly with the separation between them. Thus, the partons produced during the perturbative QCD phase are joined by a 'colour flux tube', or string, with transverse dimensions of the order of typical hadronic sizes (~ 1 fm). As the partons move apart, the string stretches and its potential energy increases; the energy per unit length, κ, is deduced from hadron spectroscopy to be $\sim 1\,\mathrm{GeV/fm}$. At some point the string may break, with the subsequent production of a new $q\bar{q}$ or di-quark pair. This break-up continues until only on-shell hadrons remain, each corresponding to a short piece of the string.

In order to generate the quark–antiquark pairs which lead to string breakups, the model invokes the idea of quantum mechanical tunnelling. In terms of the transverse mass, m_T of the new quark, the tunnelling probability (the probability that the new $q\bar{q}$ pair will appear) is given by

$$\exp\left(-\frac{\pi m_T^2}{\kappa}\right) = \exp\left(-\frac{\pi m_q^2}{\kappa}\right)\exp\left(-\frac{\pi p_T^2}{\kappa}\right).$$

The presence of the quark mass, m_q, in this formula implies a suppression of heavy quark production. The p_T distribution is Gaussian, with a local compensation between the quark and antiquark of a pair. The total p_T of a final-state hadron is taken from the

Generator	Perturbative QCD	Evolution Parameter (t)	Hadronisation Model
JETSET	Parton Shower	$\log\left(\frac{m^2}{\Lambda^2}\right)$	String
HERWIG	Parton Shower	$E_a\sqrt{\frac{p_b p_c}{E_b E_c}}$	Cluster
ARIADNE	Dipole	$p_\perp^2$	String

Table 1.3: Some basic features of commonly used hadronic event generators at LEP

separate p_T contributions of its constituent quarks.

An alternative hadronisation mechanism is the *cluster fragmentation* model proposed by Marchesini and Webber [10], in which after a parton shower any remaining gluons are forced to split into $q\bar{q}$ pairs. Adjacent quarks and antiquarks are then combined to form colourless clusters which subsequently decay into hadrons.

The clusters typically have a mass of a few GeV and can be thought of as superpositions of broad (*i.e.* short-lived) resonances. They decay isotropically in their own rest frame, the selection of decay channels being determined by phase-space. Very large mass clusters are first broken up using a string-type mechanism, while very light clusters may produce a single hadron.

The most commonly used QCD Monte Carlo programs at LEP involve various combinations of these perturbative QCD approximations and fragmentation models. JETSET [11] uses a parton shower followed by string fragmentation. ARIADNE [12] relies on a colour dipole model to produce a set of partons which are subsequently hadronised using string fragmentation. HERWIG [13] employs a parton shower followed by cluster hadronisation. Some basic features of these models are summarised in Table 1.3.

1.4   Photon Emission from Quarks

In a small fraction of $Z^0 \rightarrow q\bar{q}$ events, one may observe an energetic photon in addition to jets of hadrons [14]. These photons may have been radiated by one of the primary quarks early in the parton shower development ('prompt' photons), in which case they are generally well separated from the hadronic debris produced in the subsequent quark fragmentation. Alternatively, the photon may be produced somewhat later during the hadronisation process: either by emission almost collinearly from the parent quark or

through non-perturbative effects. Such photons are not generally well isolated from the accompanying hadrons in the event.

Naively, the fractional production rate of events containing a radiated photon should be of the order of the electromagnetic coupling constant, α (i.e. $\sim 1\%$). However, if one considers the relative probabilities of the competing photon and gluon radiation processes (q $\rightarrow$ qγ and q $\rightarrow$ qg) where

$$\frac{\mathcal{P}_{q \rightarrow q\gamma}}{\mathcal{P}_{q \rightarrow qg}} = \frac{\alpha_{em} \overline{e_q^2}}{\alpha_s C_F} \approx \frac{\frac{1}{137} 0.22}{0.2 \frac{4}{3}} \approx \frac{1}{200},$$

then a quark is clearly much more likely to radiate a gluon than a photon. ($\overline{e_q^2}$ is the mean quark charge squared and $C_F = 4/3$ is the quark colour factor.) Noting that a quark which has already radiated a fraction of its energy to gluons has a reduced phase space available for subsequent photon emission, the fraction of Z^0 hadronic decay events containing a radiated photon is expected to be only a few per mille.

1.5 Photon Emission in QCD Models

Using perturbative QCD, matrix element calculations describing photon radiation from a quark have been performed to $\mathcal{O}(\alpha\alpha_S)$, corresponding to the radiation of one photon and one gluon at tree level (i.e. the diagram has no loops) [15, 16].

In parton shower models, photon radiation from a quark is treated analogously to gluon radiation. The q $\rightarrow$ qg splitting function is modified to include a term corresponding to q $\rightarrow$ qγ

$$d\mathcal{P} = \left\{ \underbrace{\frac{\alpha_s}{2\pi} C_F}_{\text{gluon emission}} + \underbrace{\frac{\alpha_{em}}{2\pi} e_q^2}_{\text{photon emission}} \right\} \frac{dQ^2}{Q^2} \underbrace{\frac{1+z^2}{1-z}}_{\text{splitting kernel}} dz.$$

As illustrated above, the relative largeness of α_s means that a q $\rightarrow$ qg splitting is much more probable than q $\rightarrow$ qγ.

The colour dipole model is extended to include photon radiation by considering the initial q$\bar{q}$ pair not only as a colour dipole, but also as an electromagnetic dipole. Photon

radiation can thus be described in a similar manner to gluon radiation.

Each Monte Carlo program has a set of parameters whose values are fixed by adjusting them to reproduce the event shape variables and particle production rates measured in hadronic Z^0 decays. Due to the similarity between the photon and gluon emission processes, this leaves no more free parameters with which to adjust the photon emission, so comparisons with data are an invaluable method to discriminate between the various models, hopefully leading to an improved understanding of the mechanisms behind parton cascades.

1.6   Previous Studies of Photon Emission

Previous studies of events containing an energetic bremsstrahlung photon were focussed on almost completely isolated photons [17, 18]. Besides the comparisons with parton shower models mentioned above, efforts were made to measure the electroweak quark couplings [19]. Since photons couple to quarks in proportion to the square of the quark's electric charge, events containing a bremsstrahlung photon are enriched with up-type quarks of charge $2/3$. Explicitly, denoting the coupling of the Z^0 to quarks of species i as $c_i = v_i^2 + a_i^2$ where $v_i = 2I_3 - 4e_i \sin^2 \theta_W$ is the vector and $a_i = 2I_3$ is the axial coupling (I_3 is the third component of weak isospin for the fermion in question: $+1/2$ for up-type quarks and $-1/2$ for down-type),

$$\Gamma(Z^0 \to q\bar{q}\gamma) \propto 3c_d + 8c_u.$$

Combining a measurement of this quantity with a measurement of the total hadronic width of the Z^0,

$$\Gamma(Z^0 \to \text{hadrons}) \propto 3c_d + 2c_u$$

results in two equations for the two unknowns, c_d and c_u. Solving these equations led to results consistent with predictions from the Standard Model, but dominated by large statistical errors.

In these analyses, events were selected by allowing only a minimal amount of residual hadronic energy within a geometrical cone centred on the candidate photon.

The photon was then excluded from the event before the application of a jet clustering algorithm which attempts to reconstruct the original hard partons by combining the four-momenta of the final-state particles. Thus any particles which were more naturally associated with the photon were incorporated into the other jets. An event was retained only if the candidate photon remained apart from the jets after a second application of the clustering algorithm.

As far as the QCD calculations are concerned, in order to cancel the infrared singularities associated with soft gluon radiation, the soft gluon must be allowed within the photon cluster. However, if all coloured partons are to be treated equally, the quarks within the event should also be allowed to cluster with the photon, introducing the possibility that the photon may be radiated collinearly by the quark. This results in an additional singularity which must be regularised and subsequently factorised into the uncalculable photon fragmentation function. To eliminate the uncertainty due to the unknown contribution from this fragmentation function, the calculations have adopted a compromise and allow a small amount of gluonic energy into the photon cluster, but do not allow quarks to cluster with the photon. However, when analysing the experimental data, it is generally unknown whether any hadronic energy accepted into the photon isolation cone originated from a quark or a gluon at the parton level, thus making accurate comparisons with the calculations difficult.

It was pointed out [15] that a safer approach would be to apply a jet clustering algorithm to all the particles in an event, including the photon, with events being retained only if the photon possessed a large enough fraction of its associated jet's energy. At the parton level, this 'democratic' approach allows the equal treatment of quarks and gluons giving an unambiguous phase space matching between experiment and theory for all event topologies, while handling more naturally the hadrons associated with the photon. It does, however, necessitate the introduction of the photon fragmentation function, resulting in a significant non-perturbative contribution to the cross section which depends upon the amount of accompanying energy allowed within the 'photon jet'. This would, at first sight, appear to prevent an accurate comparison between the data and QCD predictions, but this previously unknown parton fragmentation contribution can be measured, thus adding new information to the dynamics of quark
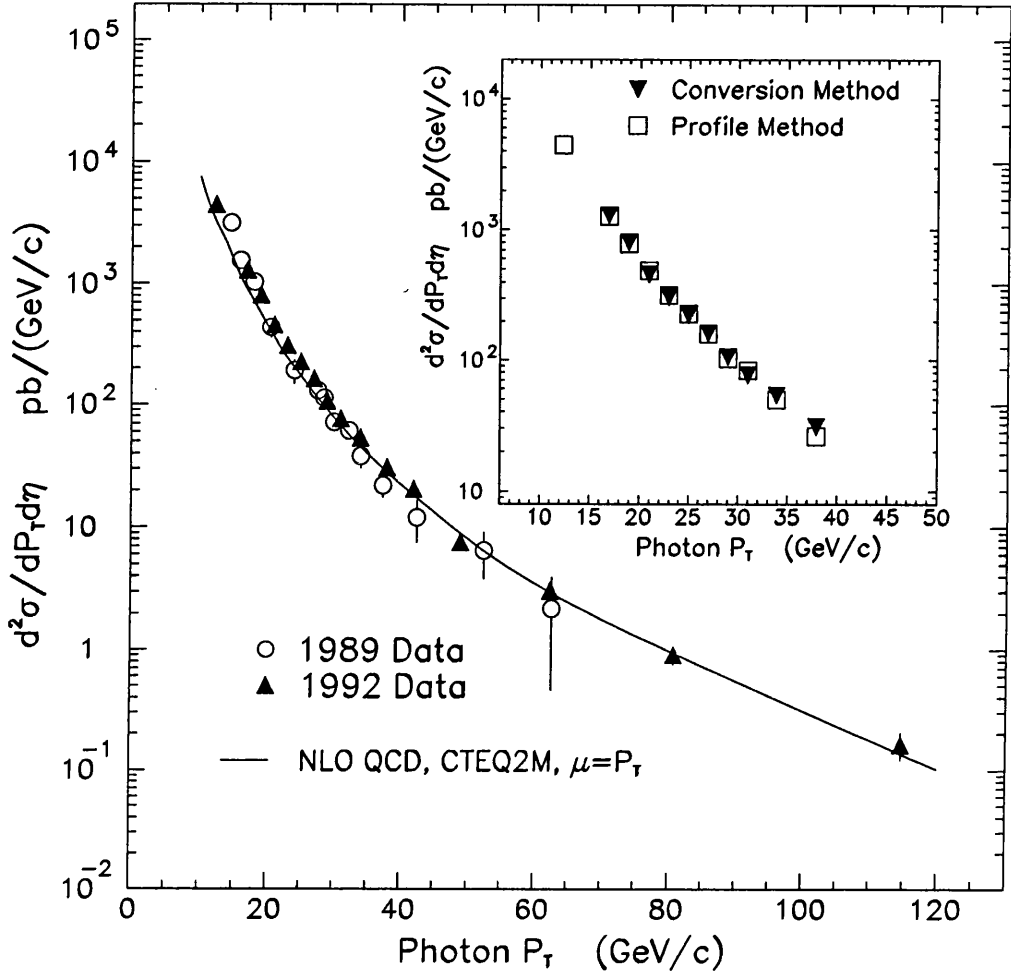
Figure 1.4: The inclusive isolated prompt photon cross section measured by CDF compared with a next-to-leading order QCD prediction

radiation.

Measurements of direct photon production at hadron colliders have shown sizeable deviations from theoretical predictions, especially in the low p_T regime (Figures 1.4 and 1.5) [20]. Recent calculations have attempted to address this discrepancy [16] and it is hoped that this situation can be further improved by such a direct measurement of the photon fragmentation function.
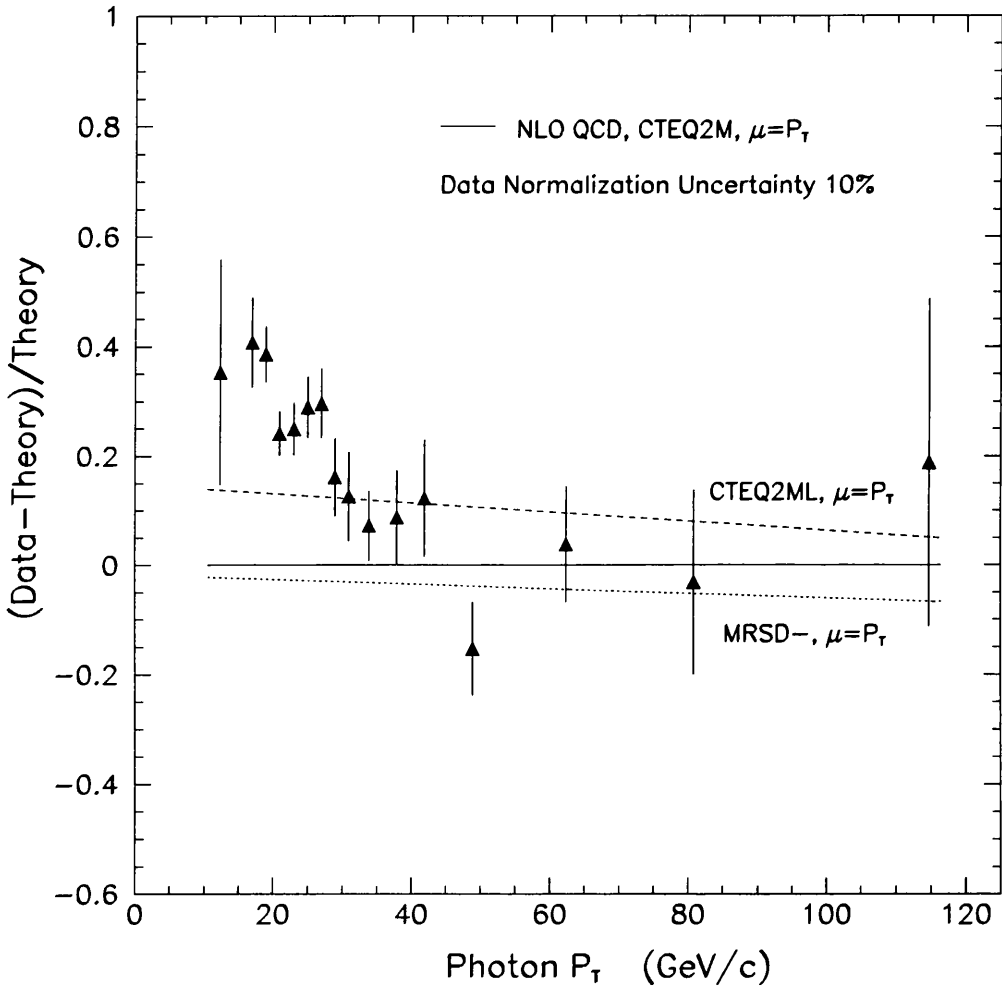
Figure 1.5: The inclusive isolated prompt photon cross section measured by CDF compared with next-to-leading order QCD predictions with variations of parton distributions

Chapter 2

The ALEPH Detector at LEP

2.1 The LEP Collider

The ALEPH detector is one of the four large experiments at LEP, CERN's Large Electron Positron collider, designed for studying electron–positron annihilations.

The 27 km circumference LEP storage ring is the last accelerator in a chain of five [21]. The electrons are created using a high intensity electron gun, and subsequently passed to a 200 MeV linac. At this point the electrons can either be passed through a 600 MeV linac and stored in the 600 MeV Electron-Positron Accumulator (EPA), or they can be fired onto a tungsten converter to create e^+e^- pairs from shower photons. These positrons are then transferred to the EPA via the 600 MeV linac.

After accumulating sufficient intensities of particles, the EPA injects into the Proton Synchrotron (PS), operating as a 3.5 GeV e^+e^- synchrotron, which in turn injects into the SPS, acting as a 20 GeV electron positron injector for LEP. Eight bunches each of electrons and positrons circulate in opposite directions around the LEP ring, their orbits being controlled by about 4000 dipole, quadrupole and sextupole magnets. The beams are steered to collide at the four experimental points but remain separated over the remainder of the circumference by forcing a series of closed oscillations in the horizontal orbit (the *Pretzel* scheme). This chain of accelerators forming the LEP injection scheme is illustrated in Figure 2.1.

The beams currently collide with a centre of mass energy around the Z^0 mass
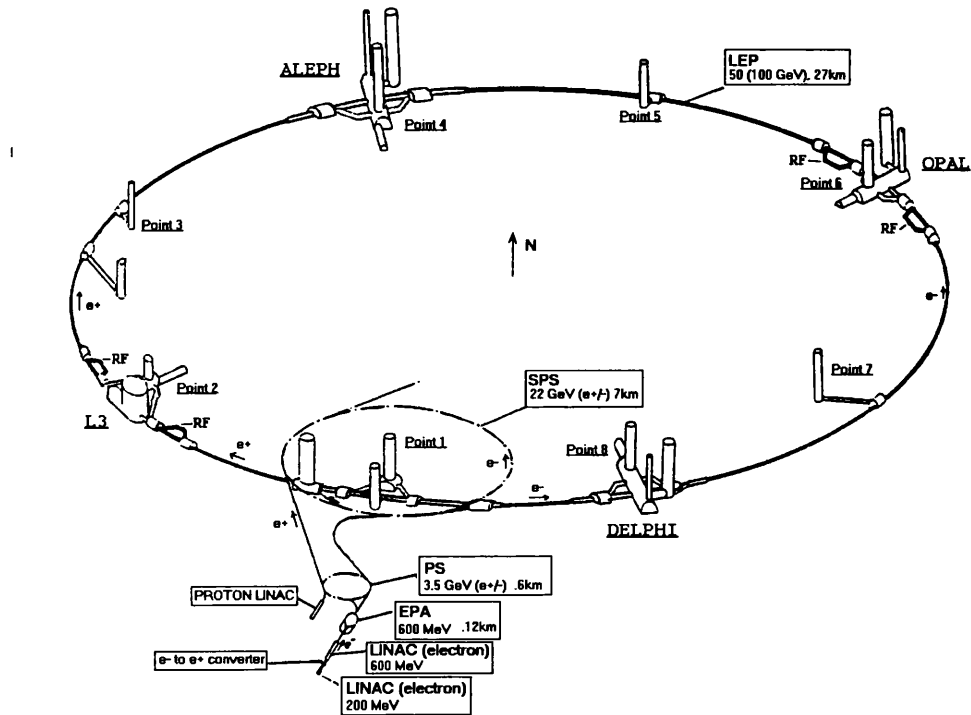
Figure 2.1: The LEP storage ring and the chain of accelerators used to create and inject particles into it

(91.2 GeV), although it is planned to increase this to above the W^+W^- threshold (~ 160 GeV) after 1995. Typical luminosities are approximately 10^{31} cm$^{-2}s^{-1}$ giving around 800 Z^0 per hour when running at the Z^0 peak.

2.2 The ALEPH Detector

Given the relatively low event rate at LEP (compared with ep and $p\bar{p}$ colliders) the ALEPH detector has been designed to gather as much interesting information as possible about any event. However, a typical hadronic Z^0 decay is complex, with around 20 charged particles and a similar number of neutrals distributed over the entire solid angle. By constructing ALEPH as a modular collection of independent subdetectors it is sensitive to all Z^0 decay products except neutrinos

Figure 2.2 shows a cut-away view of the ALEPH detector. The tracking detectors, closest to the beam pipe, are surrounded by the calorimeters. The electromagnetic calorimeter is contained within the superconducting solenoid, while the hadron calorimeter makes use of the iron magnet return yoke as an absorber.

The coordinate system used by ALEPH has its origin at the nominal interaction point in the centre of the detector. The positive z-axis is along the electron direction, the x-axis points towards the centre of the LEP ring and the y-axis points upwards. Spherical coordinates, when used, are defined as

$$x = r \sin \theta \cos \phi$$
$$y = r \sin \theta \sin \phi$$
$$z = r \cos \theta$$

The following is a brief overview of the ALEPH detector and data acquisition system. A full description can be found in [22, 23].
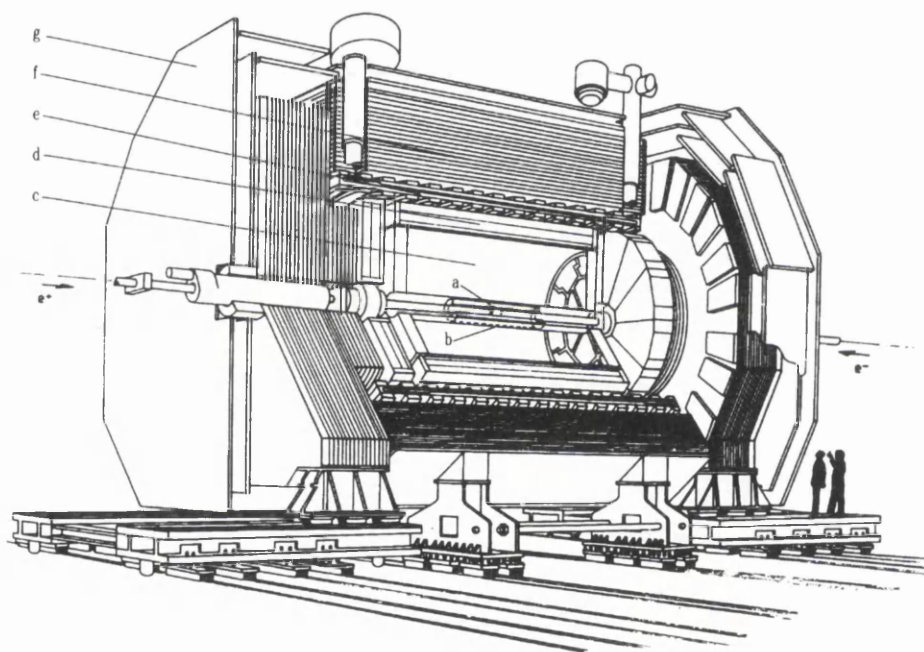
Figure 2.2: A cut-away view of the ALEPH detector: (a) vertex detector, (b) inner tracking chamber, (c) time projection chamber, (d) electromagnetic calorimeter, (e) superconducting solenoid, (f) hadron calorimeter / magnet return yoke, (g) muon chambers.
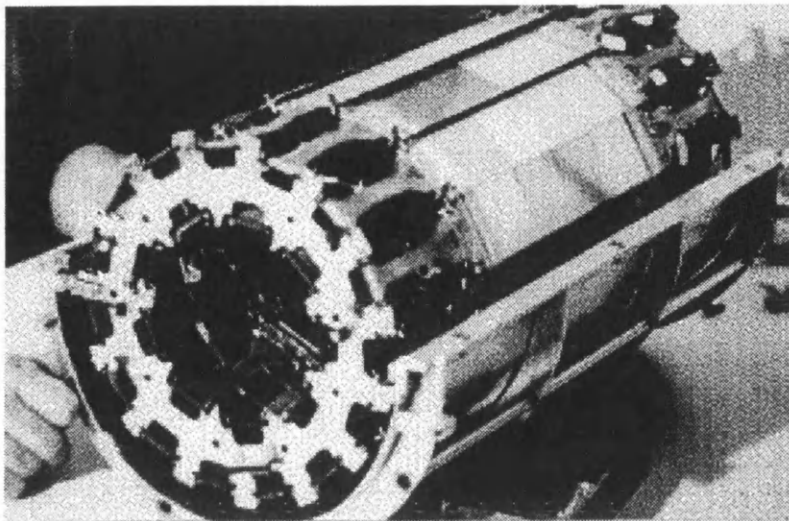
Figure 2.3: The silicon vertex detector

2.2.1   Tracking Detectors

Vertex Detector: VDET

The VDET [24] comprises two cylindrical layers of silicon wafers surrounding the interaction point at radii of 6.3 and 11.0 cm; each layer is 20 cm long. Figure 2.3 shows the VDET before being inserted into ALEPH.

Particles passing through a wafer deposit ionisation energy, producing electron-hole pairs which are collected on either side of it; on one side, the wafer is read out in the z direction, while on the other it is read out in the $r\phi$ direction. However, hits from the two sides are *not* associated by the read-out hardware, but are added separately to track fits during event reconstruction (see Section 2.3.1).

Inner Tracking Chamber: ITC

The ITC (see Figure 2.4) is a 2 metre long, cylindrical, multi-wire drift chamber extending radially from 160 to 260 mm from the beam. It comprises 8 layers of sense wires running parallel to the beam direction, spaced $1 - 1.5$ cm apart, which detect ionisation from particles passing close by. An $r\phi$ coordinate can be determined with a precision of $\sim 100\,\mu$m by measuring the drift time to adjacent wires, while z coordinates are determined from the difference in arrival times of pulses at either end
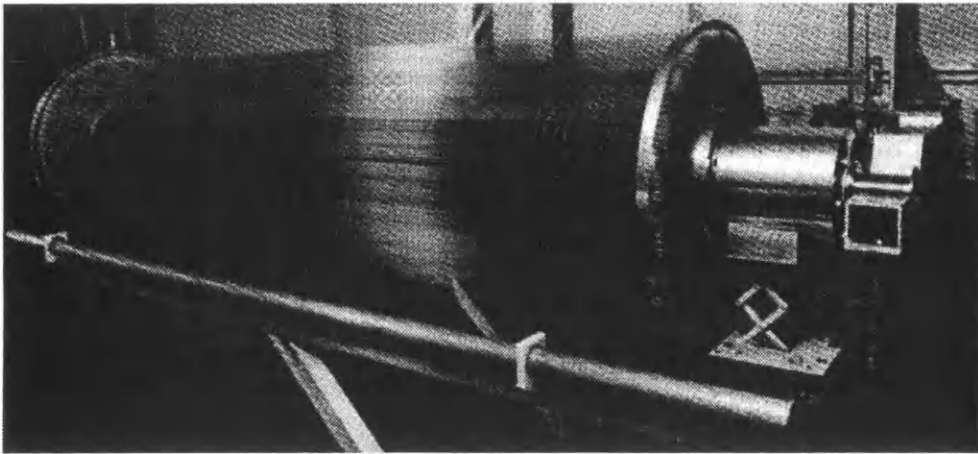
Figure 2.4: The inner tracking chamber

of the sense wires, with a precision of ~ 3 cm.

The rôle of the ITC in ALEPH is two-fold: it provides up to eight accurate $r\,\phi$ coordinates for track finding and it provides the tracking information for the Level 1 trigger (see Section 2.2.4), utilising its fast read-out time ($\sim 2\,\mu$s)to ensure that non-interesting events are quickly discarded.

Time Projection Chamber: TPC

The central tracking chamber in ALEPH is a large, three-dimensional imaging drift chamber, or TPC, immersed in an axial magnetic field of 1.5 T. It is about 4.7 m long and extends to a radius of 1.8 m from the beam. Figure 2.5 shows a cut-away view. The central membrane is held at a potential of around -27 kV while the end-plates are grounded, resulting in an axial electric field of ~ 115 V/cm. The inner and outer field cages, comprising circular copper electrodes linked by resistor chains to the central membrane, ensure the electric field is uniform.

Each end-plate consists of 18 wire chambers (sectors) comprising three planes of wires: the gating grid, a cathode plane, and the sense wires. About 4 mm behind the sense wires is a plane of 21 concentric rows of finely spaced cathode pads, interspersed with long trigger pads, as shown in Figure 2.6. Electrons produced by the ionisation from traversing charged particles drift towards either end-plate, causing ionisation
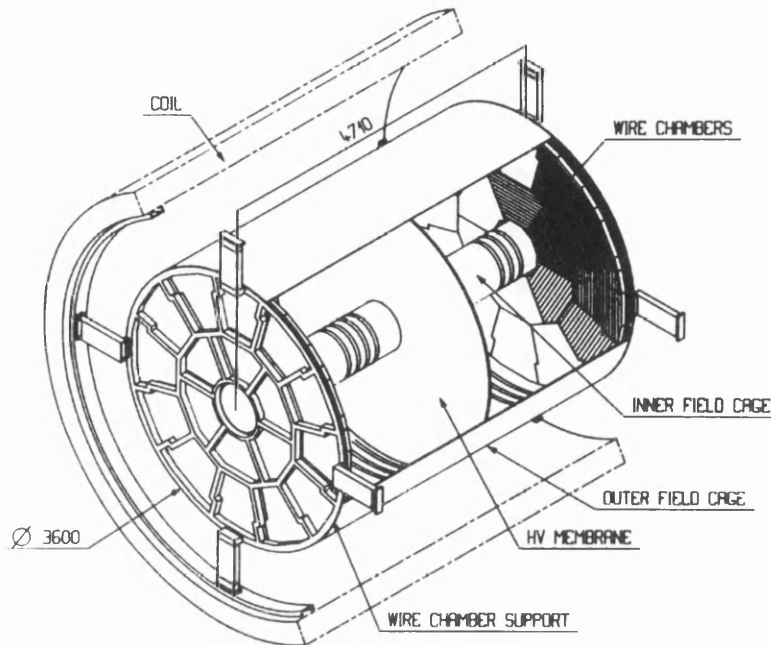
Figure 2.5: A cut-away view of the time projection chamber

avalanches around the sense wires and inducing signals on the cathode pads. A three-dimensional coordinate is obtained from the impact point of the pulse ($r\,\phi$ coordinate) and its arrival time (z coordinate). The pulse height on the sense wire is used to determine the ionisation density, dE/dx.

If the TPC were operated in a continuously sensitive mode, the positive ions produced in the avalanches around the sense wires would migrate towards the central membrane and alter the drift field, resulting in track distortions. The gating grid is used to minimise this effect. When the grid is *open* a potential of V_g ($\sim -67\,\mathrm{V}$) is placed on all the wires, leaving the gate transparent to the passage of electrically charged particles. The grid is *closed* by applying a voltage $V_g \pm \Delta V_g$ ($\Delta V_g \approx 40\,\mathrm{V}$) to alternate wires: the resulting dipole field renders the grid opaque to the passage of charged particles. Figure 2.7 shows schematically the situation for the gate both open and closed. The gate is switched synchronously with the bunch-crossing timing. It is opened a few microseconds before a bunch-crossing: a Level 1 trigger NO results in the gate being closed until just before the next bunch-crossing; a Level 1 YES holds the gate open for the $50\,\mu s$ necessary for all the ionisation electrons to drift to the wire
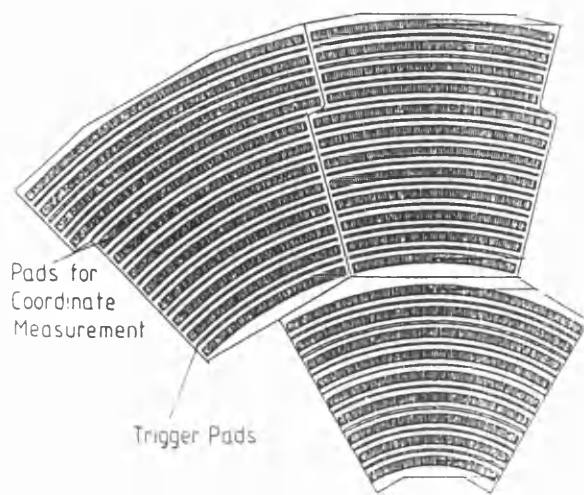
Figure 2.6: The arrangement of pad-rows on TPC sectors: finely spaced cathode pads interspersed with longer trigger pads.

chambers.

A laser calibration system, built and maintained by the Glasgow group, is used to provide information on possible distortions of particle tracks and to measure the drift velocity vector, necessary for an accurate z coordinate determination. Two ultra-violet lasers are used to produce thirty straight ionisation tracks originating from near the interaction point. Since the laser beams should be unaffected by either the electric or magnetic fields, any measured curvature in the tracks can be used to correct the sagitta of particle tracks. The drift velocity is calculated from the reconstructed polar angles of the laser tracks.

2.2.2 Calorimetry

Electromagnetic Calorimeter: ECAL

The ECAL is a lead/proportional wire-chamber sampling device with 45 layers, corresponding to a nominal thickness of 22 radiation lengths. It is constructed as a barrel region plus two separate sections, one on each end cap, as shown in Figure 2.8. These are each divided into twelve modules, each covering an azimuthal angle of 30°. The structure of a typical layer is shown schematically in Figure 2.9. The lead sheets cause
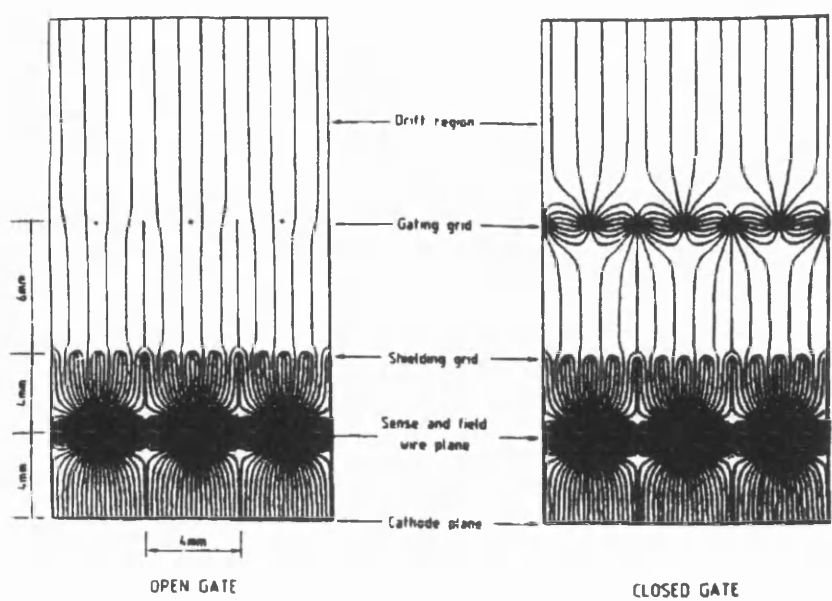
Figure 2.7: The resulting electric field configuration when the TPC gating grid is in the open (left hand diagram) and closed (right hand diagram) states.
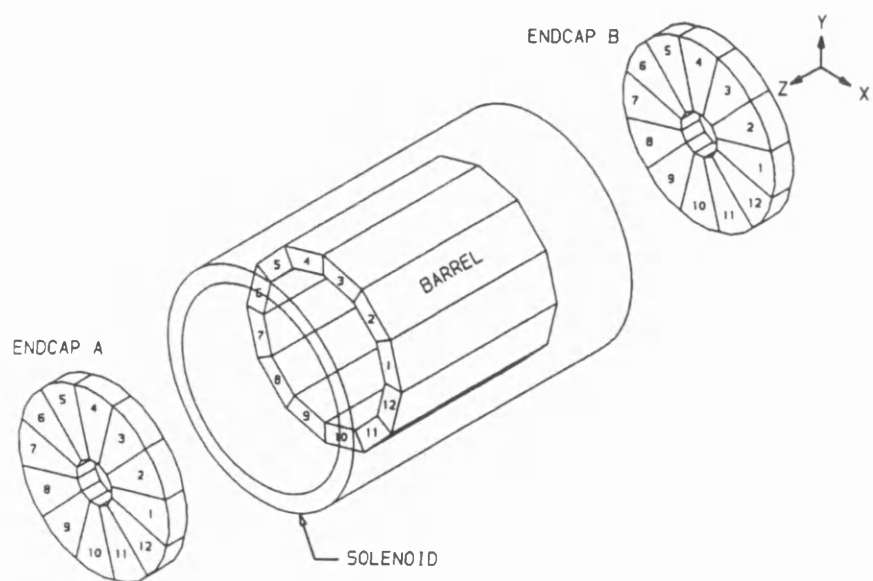
Figure 2.8: The layout of ECAL barrel and endcap modules
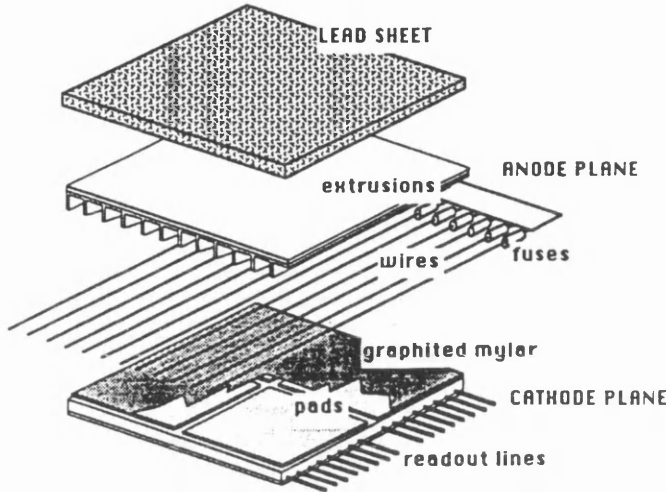
Figure 2.9: A schematic view of an ECAL layer

electrons, positrons and photons to produce showers of many more electromagnetic particles, causing large signals on the proportional wire chambers. The signals are read out capacitively using cathode pads placed behind a highly resistive graphite-coated Mylar 'window'. The pads from consecutive layers are connected internally to form towers projecting towards the interaction point. Each of the 77 000 such towers subtends an angle of $1° \times 1°$ and is read out in 3 segments of depth, known as 'storeys', corresponding respectively to $(4, 9, 9)$ radiation lengths. The ECAL was designed to have the best possible granularity in order to simplify the identification of electrons inside hadronic jets and to facilitate the measurement of photon energies in a background of hadrons. In addition, signals are also available from the wire planes of each module, providing redundancy in the energy measurement.

The energy resolution, determined by comparing the measured energy to the corresponding track momentum is found to be $\Delta E/E = 0.18/\sqrt{E/GeV} + 0.009$.

Hadron Calorimeter: HCAL

The HCAL is similar in construction to the ECAL with 23 alternate layers of iron and limited streamer tubes, the iron serving as a return yoke for the magnetic field. (Streamer, or Iarocci, tubes [25] are similar to proportional counters, but operate at a slightly higher voltage. An incident charged particle thus produces a signal which is independent of the amount of primary ionisation it creates). Cathode pads behind the streamer tubes are connected in projective towers, each subtending a solid angle of $3.7° \times 3.7°$, corresponding to about 14 ECAL towers. The signals from the streamer tube anode wires are used as a measure of energy deposition for triggering, while cathode strips running along the tubes are used to form a digital image of the path of a particle through the HCAL.

Outside the HCAL, two further double layers of limited streamer tubes form the muon chambers. The tubes are instrumented with orthogonal cathode strips rather than pads, which allows simple tracking of charged particles escaping from the HCAL.

2.2.3 Luminosity Measurement

The luminosity delivered by LEP is determined from the rate of Bhabha scattering events at small scattering angles, where the interference between Z^0 and γ exchange terms is almost negligible, and the cross-section is well known from QED. To obtain an accurate luminosity measurement, a precise determination of the Bhabha scattering angle is essential since the cross-section is a steep function of this angle.

Since September 1992, the ALEPH luminosity measurement has been performed with a silicon–tungsten luminosity calorimeter (SiCAL), and previous to that with a lead-wire sampling calorimeter (LCAL); a fast relative luminosity measurement is available online using a very small angle Bhabha calorimeter (BCAL).

LCAL

The design of the LCAL is very much analogous to that of the ECAL: it is a lead/wire-chamber sampling device with a nominal thickness of 24.6 radiation lengths. The total energy and position of electromagnetic showers are measured using small cathode pads

connected internally to form towers, giving an energy resolution of $\sigma_E = 0.014\,E +$ $0.20\sqrt{E}$ (where E is in GeV) and a position resolution of $\sigma_x = \sigma_y = 1.4\,\text{mm}$.

SiCAL

To enable a more precise luminosity measurement than was possible with the LCAL, the SiCAL was installed in ALEPH during 1992 [26]. It comprises two homogeneous, cylindrical modules surrounding the beam-pipe at distances of $\pm 250\,\text{cm}$ from the interaction point. Twelve layers of silicon pad detectors, each segmented into 16 radial pad rows and 32 azimuthal sectors are interleaved with tungsten sheets forming a sampling electromagnetic calorimeter of 23.4 radiation lengths in depth. The active volume subtends a region in polar angle between 24 and 58 milli-radians. The precision of this device is such that even after only two months of data-taking, the largest uncertainty in the luminosity measurement was that due to lack of theoretical precision in $\mathcal{O}(\alpha^2)$ leading-log and sub-leading terms in the photon exchange cross-section. Using data collected during 1990 and 1991, the measurement of the hadronic Z^0 decay cross section using LCAL alone was 41.68 ± 0.21 nb; the value obtained from the two months of SiCAL running in 1992 was 41.56 ± 0.146 nb [27].

BCAL

Online monitoring of the relative luminosity from LEP is provided by four calorimeters which detect very small angle Bhabha events with an expected rate of 5 Hz at a luminosity of $10^{31}\,\text{cm}^{-2}\text{s}^{-1}$. The modules are located on either side of the beam-pipe at distances of $\pm 7.8\,\text{m}$ from the interaction point. Each calorimeter comprises tungsten converter sheets interspersed with sampling layers of plastic scintillator and a plane of vertical silicon strips. The luminosity value measured by the BCAL is also passed to the LEP control room to aid in optimising the collision rate in ALEPH.

2.2.4 The Trigger

Given the relatively low luminosity (and hence event rate) at LEP one aims to accept *all* genuine e^+e^- interactions. This goal must be realised within the constraints that

backgrounds should be kept to a manageable level, the TPC must be gated at an acceptably low rate and any dead time induced by detector read-out should be negligible. The ALEPH trigger was designed to be sensitive to single particles or jets while keeping the overall rate acceptable for data writing ($\sim 1 - 2$ Hz). The trigger comprises four main detector components: ITC, TPC, ECAL and HCAL. The signals from each are grouped into 60 logical segments: the ECAL and HCAL are subdivided into 60 projective towers, the ITC wires are grouped into 60 ϕ segments and the TPC as 60 segments in $\theta - \phi$. Luminosity triggers originate from the LCAL and SiCAL: each LCAL module is subdivided into 12 overlapping towers and, similarly, each SiCAL module into 8 towers. To obtain maximum efficiency, the trigger has been subdivided into three levels, ensuring that non-interesting events are discarded as quickly as possible.

Level 1 Trigger

The Level 1 trigger makes a fast decision about an event, based on the logical OR of several conditions:

- a coincidence between ITC tracks and ECAL energy deposits

- a coincidence between ITC tracks and HCAL energy deposits

- an energy deposit in the ECAL only

- a single-arm or coincidence hit in the luminosity chambers.

A decision is available within $5\,\mu s$ of the bunch crossing: a YES initiates digitisation of the subdetectors, a NO results in the readout being cleared and readied for the next bunch crossing.

Level 2 Trigger

Following a Level 1 YES decision, about $50\,\mu s$ are required for all the ionisation trails to drift to either end of the TPC. During this time, TPC track processors search the incoming data from the coarse trigger pads for charged track patterns. The Level 2

decision is made by replacing the ITC mask from Level 1 with the new TPC mask. A Level 2 YES initiates a full read-out of the detector, while a NO causes all data conversion to be aborted and the detector to be re-enabled for the sixth bunch crossing after that which produced the initial Level 1 YES.

Level 3 Trigger

The Level 3 trigger is an analysis process running within the DAQ system before the data are recorded. A series of dedicated event processors look at the full digitisations of an event to verify the Levels 1 and 2 decisions. Rather than aiming for an excellent event reconstruction precision, the processors have a high pattern recognition efficiency.

In general, events are triggered by more than one trigger condition. This redundancy enables the trigger efficiency to be measured: it is found to be 100% for hadronic and leptonic Z^0 decays, and at least 99% for Bhabha events.

2.2.5 Data Acquisition

The ALEPH detector has over 700 000 read-out channels, the signals from which are digitised every time a trigger is produced, generating over 500 MegaBytes of raw data each second. The read-out system must reduce this data volume by eliminating uninteresting information, and format it into convenient data structures suitable for further analysis.

The design of the ALEPH DAQ system has been based on a hierarchical tree-like structure, utilising the natural sub-division into distinct subdetectors [28]. Figure 2.10 shows a schematic view. Data are passed between layers of the tree using FAST-BUS [29]. The *Main Trigger Supervisor* (MTS) synchronises the read-out electronics through *Fan In/Out* (FIO) units and informs the associated *Read Out Controllers* (ROCs) of an imminent bunch crossing. The ROCs initialise the front-end modules, read them out (performing zero suppression by comparing the measured values with pre-defined thresholds) and format the data into a standard tabular format (*BOS banks* [30]). The
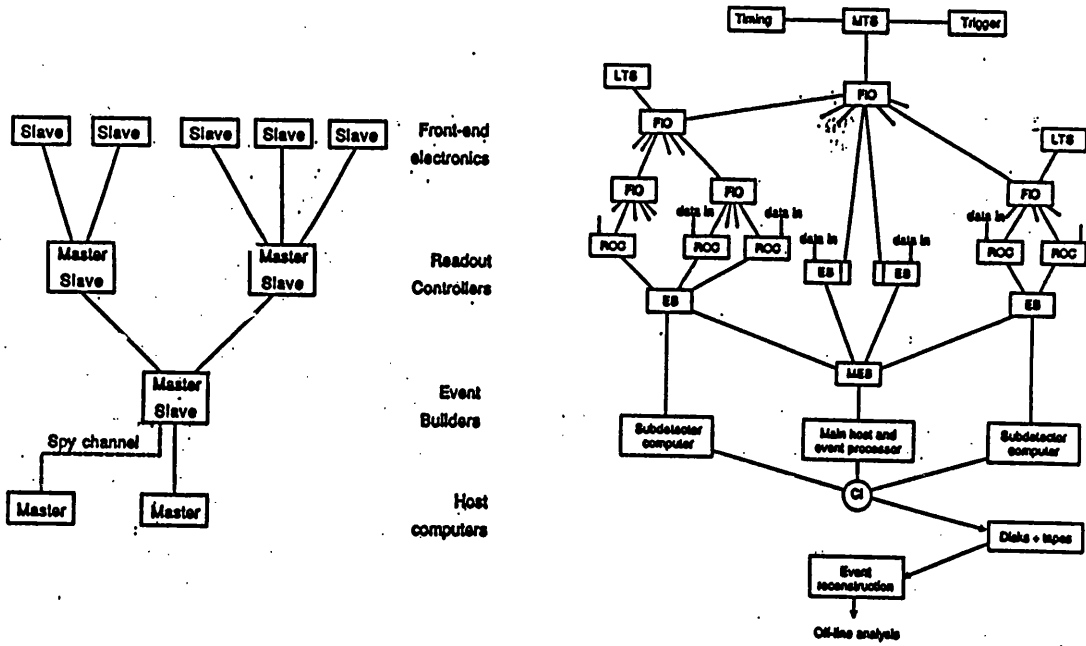
Figure 2.10: The basic ALEPH readout architecture

banks are passed to *Event Builders* which construct sub-events at the subdetector level before passing them to the Main Event Builder which collects and formats complete events then transmits them to the online computers. After the initial synchronisation with a bunch crossing, the data flows up the tree asynchronously, with several sub-events being buffered at each stage, until reaching the main event builder where they are re-synchronised. Simulations have shown that this approach minimises the overall dead-time.

Another feature of the ALEPH DAQ system is that any subset of the system can be configured to run independently of the rest, allowing individual subdetectors to switch easily from the ALEPH read-out configuration to stand-alone mode. This is achieved by re-programming the FIO units so that only selected ROCs see the main trigger signals while others can derive their timing information from *local* triggers [31].

2.3 Event Reconstruction

All events passing the levels one, two and three trigger selection are written to disk. At the end of a run (after approximately 180 MegaBytes of data have been collected) the disk-resident data are written to tape and sent to the computer centre on the main CERN site. Control of the disk is passed to a second VAX cluster at Echenevex, FALCON (*Facility for ALeph COmputing and Networking*), where events are reconstructed in a quasi-online environment. FALCON is a cluster of 10 VAX stations plus 2 micro-VAX bootnodes, dedicated to running the ALEPH reconstruction program, JULIA (*Job to Understand Lep Interactions in Aleph*). As a first step, one of the micro-VAXes performs a preliminary scan of the run to evaluate constants necessary for the event reconstruction (*e.g.* the TPC drift velocity), while simultaneously constructing an *event directory*, containing the address of each event within the file. Using the event directory, events can be efficiently assigned to individual VAX-stations to be reconstructed in parallel. Immediately after all events in a run have been reconstructed, analysis tasks are automatically performed which allow the quality of the data to be monitored and potential problems investigated by the shift crew. The processed output is then sent via an optical link to the offline computers on the Meyrin site, where the events are filtered to remove those not useful for further analysis (*e.g.* no tracks or energy). The resulting files are the Data Summary Tapes (DSTs).

2.3.1 Track Reconstruction

Track reconstruction is performed as a multi-step process. Beginning with the TPC, the pad hits are examined for *clusters* in space-time which are subsequently decomposed into (r, ϕ, z) coordinates. A search is then performed for *chains* of coordinates which are consistent with a helix. Track candidates are formed by linking together individual chains. The next step is to project the track candidates back to the ITC, searching for coordinates within an $(r\phi, z)$ *road* around the trajectory. By performing a series of track fits of increasing complexity with these coordinates, which eventually include all coordinate errors, possible multiple scattering and kinks from in-flight particle decays, a set of tracks with excellent momentum and directional resolution can be obtained.

However, due to the large distance through which these tracks must be extrapolated to the interaction point, their spatial resolution is not good. This can be greatly improved by re-fitting the tracks after including $r\,\phi$ and z hits from the VDET which lie close to the extrapolated tracks. After the full track fit has been done, a typical track has a momentum resolution, $\Delta p/p^2 = 0.6 \times 10^{-3}(\mathrm{GeV}/c)^{-1}$ and a spatial resolution of around 30 μm.

After finalising the track candidates, the TPC wire hits are examined to determine ionisation rates. Wire hits are associated with a charged track if the track projects onto the wire and the hit is in a time window consistent with the track. Once hits have been associated with tracks, the measured pulses can be corrected for attenuation during drift and other known effects.

2.3.2   Calorimeter Object Reconstruction

Clusters are formed in the electromagnetic and hadronic calorimeters separately from spatially connected storeys which register an energy deposition. Track candidates are then extrapolated outwards through the calorimeters; if a track extrapolates through a fired storey, then the corresponding cluster is associated with the track. After merging any overlapping ECAL and HCAL clusters, neutral clusters are identified as those not associated with a charged track or where the calorimetric energy is in excess of that of the charged track. In this way, a set of charged and neutral calorimeter objects is obtained.

For an electromagnetic shower, the polar and azimuthal angles are calculated from an energy-weighted mean of the polar and azimuthal angles of individual storeys in the cluster. Using the extrapolation of electron tracks in Bhabha events, the deviation of the expected value can be obtained, as shown in Figure 2.11. The observed 'S-shape' effect is due to the calorimeter granularity being comparable to the electron shower size. This is corrected for using a periodic function of the tower coordinates.
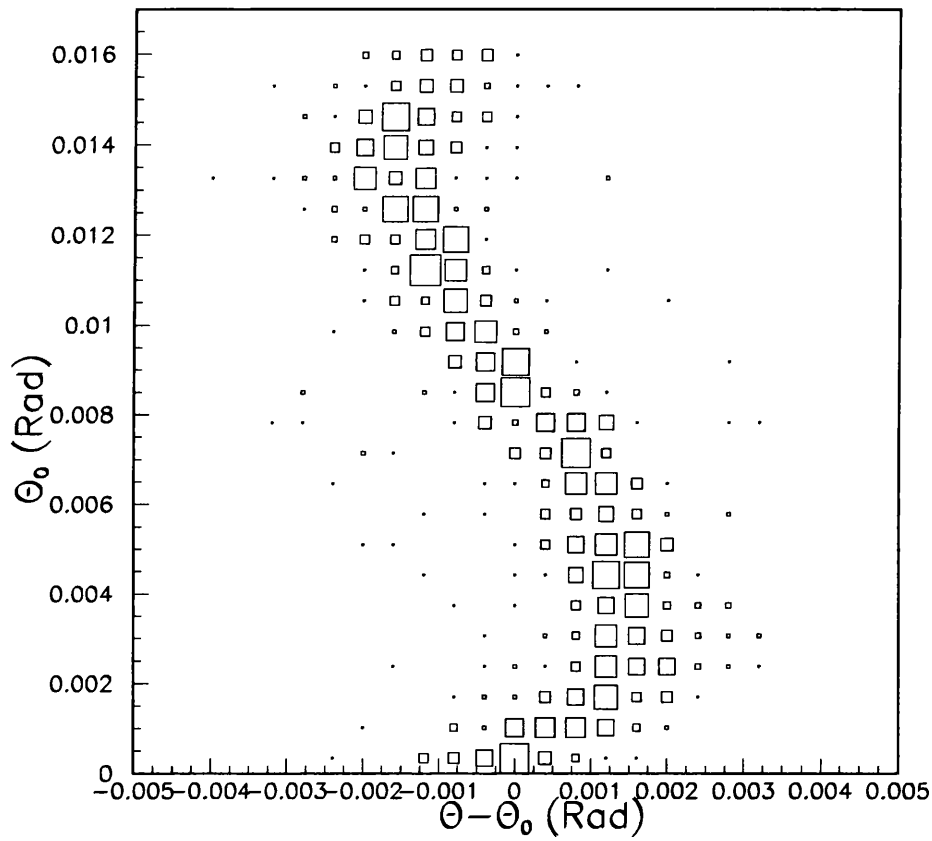
Figure 2.11: The polar angle of the reconstructed barycentre, θ, as a function of the true polar angle, θ_0

2.3.3 Photon Identification

The clustering algorithm described above builds big clusters, often merging energy from photons and hadronic interactions. A second clustering scheme has been devised to identify and reconstruct photons which is better adapted to hadronic Z^0 decays. For the sake of efficiency, it is applied only to the previously identified electromagnetic clusters. It is based on the fact that electromagnetic showers originating from a photon generally start in the first segment of depth of the ECAL and that, unlike the cell patterns of hadronic clusters, storeys receiving energy from a photon have a compact arrangement and most of them share a face with another storey associated to the same photon.

The storeys of the first segment in depth of the ECAL are scanned in order of decreasing energy. A storey without a more energetic neighbour defines a new cluster. Other storeys are assigned to the cluster of their highest energy neighbour, where two storeys are considered neighbours only when they share a common face. The same procedure is then applied to the storeys of the second and third segments in depth, except when processing a storey, the algorithm looks first for a neighbour in the previous segment. The clusters found in this way are retained as photon candidates if there is no charged track impact at a distance of less than 2 cm from the cluster barycentre.

The position of a photon impact point is computed in two steps. A first approximation is given by the cluster barycentre (the energy weighted mean of the coordinates of each storey centre). This position is then corrected for the finite size of the calorimeter cells using the parametrisation of the S-shape curve described above.

In order to reduce the sensitivity of the energy measurement to hadronic backgrounds and clustering effects, the photon energy is computed from the energy collected in the four central towers of the cluster, and the expected value of the energy fraction in the four towers, F_4. This fraction is computed from the parameterisation of the shower shape for a single photon in the calorimeter.

Figure 2.12 shows three views of a reconstructed hadronic event. The left-hand diagram shows an end-on view of the detector with some of the subdetectors labelled. The upper right inset is also an end-on view, but is magnified to show only the ITC and VDET. The lower right view is a side-on projection. Coordinates measured in the TPC are shown as small crosses, with the reconstructed tracks shown as coloured lines through them. Energy deposits in the individual ECAL storeys are shown as coloured squares, with the total energy deposition in towers indicated by a histogram. Pad hits in the HCAL are shown as white squares and the total energy deposition represented by a histogram. On the left-hand side of the end-on view, a muon track is seen passing right through the HCAL and registering in the muon chambers.
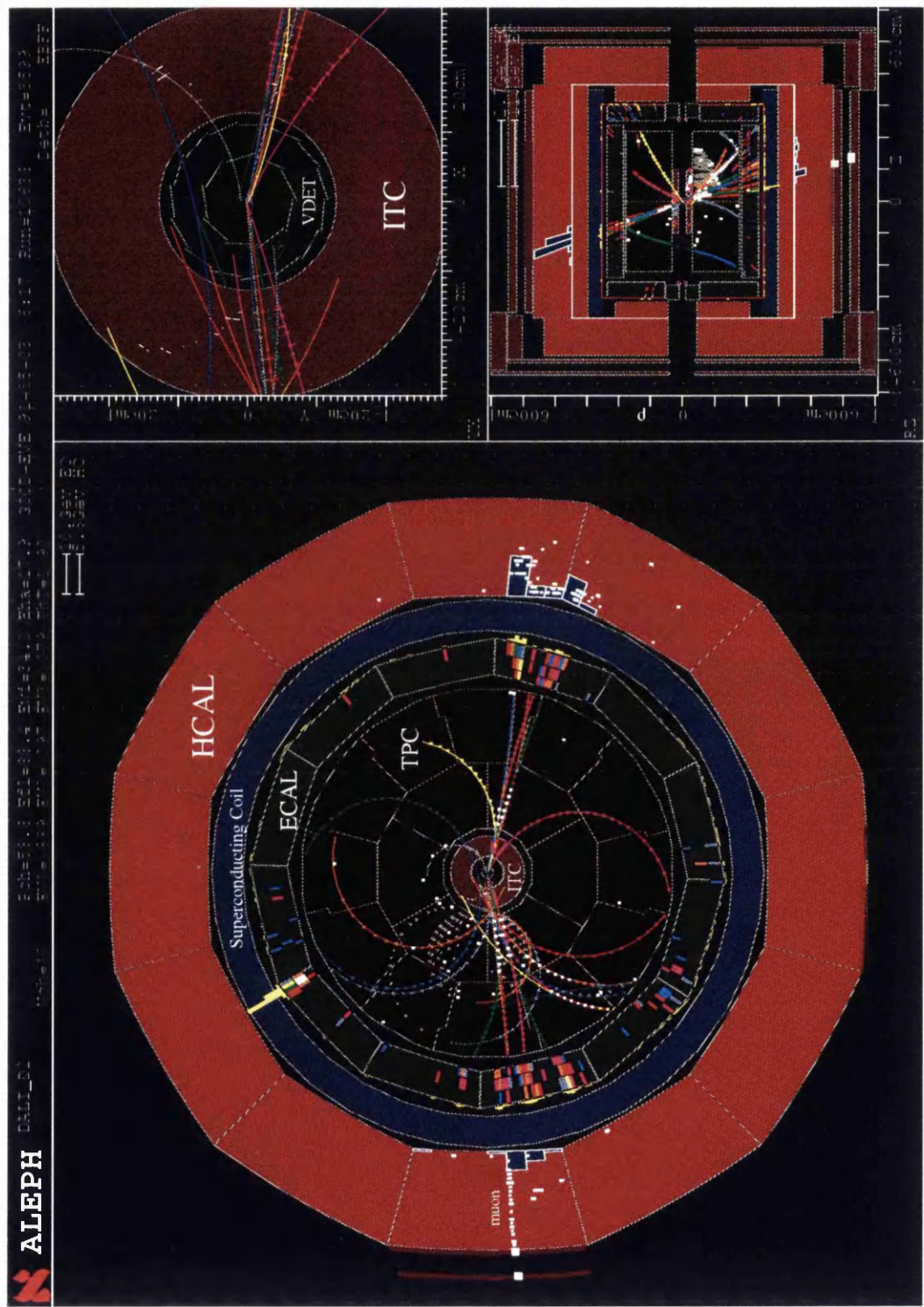
Figure 2.12: A hadronic event in the ALEPH detector

Chapter 3

Calculation of the Photon + n-Jets Cross Section

3.1 Introduction

This chapter discusses in some detail the perturbative and non-perturbative components of the cross section for hadronic events containing an energetic photon emitted by a quark. A new, 'democratic' photon selection algorithm is described which eliminates the difficulties in matching the theoretical and experimental phase space definitions which plagued the two-step cone algorithms used previously (Section 1.6). This algorithm also allows the selection of photons embedded in hadronic jets, where the non-perturbative fragmentation contribution to the cross section is dominant. It is shown that the production rate of events comprising one hadronic jet and one jet containing an energetic photon which was emitted from a quark is particularly sensitive to the (uncalculable) quark-to-photon fragmentation function.

3.2 Calculations in Perturbative QCD

As was introduced in Chapter 1, calculations in QED and QCD are usually performed using perturbation theory: Feynman diagrams are constructed and evaluated up to a fixed order of the appropriate coupling constant, α or α_s. However, in evaluating

Feynman diagrams that contain loops, divergent integrals over loop momenta can occur. To make sense of these, the divergent expressions are first made 'temporarily finite' through some *regularisation* procedure which introduces additional parameters (for example, an ultra-violet momentum cut-off, Λ, or a non-integral space–time dimension, $D = 4 - 2\epsilon$). In this way, the divergences can be re-expressed in a well-defined way (although still with divergent limits). Such regularised divergences are then removed by absorbing them into the definitions of physical quantities through a *renormalisation* procedure — an arbitrary prescription which introduces a new dimensional scale, μ, on which, at finite order, the renormalised quantities such as the coupling constants, now depend explicitly. It is essential, however, that the observable quantity which is being calculated should not depend on this artificial renormalisation scale, thus any change in μ must be compensated by a change in the coupling constant. This constraint gives rise to the so-called *renormalisation group equations*.

Most calculations in fixed order QCD perturbation theory are performed using dimensional regularization of ultra-violet divergences. In this approach, a reduced number of space–time dimensions, $D < 4$ are used. Integrals of the form

$$\frac{\mathrm{d}^4 k}{(2\pi)^4}$$

become

$$(\mu)^{2\epsilon} \frac{\mathrm{d}^{4-2\epsilon} k}{(2\pi)^{4-2\epsilon}}$$

where $\epsilon = 2 - D/2$. Divergences now appear as poles, which in the popular *modified minimal subtraction* ($\overline{\mathrm{MS}}$) renormalisation scheme [32], can be subtracted to leave a finite result.

3.3 The Photon + n jet Cross Section

In lowest order, the $e^+e^- \to n$ jets $+\gamma$ cross section is given by [33]

$$\mathrm{d}\sigma^{\mathrm{LO}}\left(n\,\mathrm{jets} + \gamma\right) = \Theta \left\{ \mathrm{d}\hat{\sigma}_0\left(n\,\mathrm{partons} + \gamma\right) \right\}, \tag{3.1}$$

where $d\hat{\sigma}_0$ is evaluated in the tree approximation and Θ represents any experimental cuts applied (for example, on the photon energy and polar angle). In this way the theoretical cross section can be easily matched to an experimental measurement. At this order, each parton is identified as a hadronic jet, and the photon as a photon.

At next-to-leading order, in addition to QCD corrections to the n parton processes including a photon, the possibility of a parton fragmenting into a photon is introduced, giving a cross section

$$
\begin{aligned}
d\sigma^{\text{NLO}} (n\,\text{jets} + \gamma) \;=\; \Theta \Bigg\{ & d\hat{\sigma}_1 \, (n\,\text{partons} + \gamma) \\
& + \int d\hat{\sigma}_0 \, ([n+1]\,\text{partons} + \gamma) \\
& + \sum_a \frac{d\hat{\sigma}_0 \, ([n+1]\text{partons})}{dE_a} \, dE_a \, dz \, dE_\gamma \, \delta \left(E_\gamma - z E_a \right) D_{a\to\gamma}(z) \Bigg\}.
\end{aligned}
\tag{3.2}
$$

The first term in this expression describes the virtual one-loop corrections to the tree-level n-partons + photon process; the second represents the tree-level emission of an additional parton. In both these cases a prompt photon is produced in the hard process. The final term is a contribution from the lowest order $(n+1)$ parton process where one of the partons fragments into a photon, the photon obtaining a fraction z of its parent parton's momentum. The sum runs over all partons, a, with each contributing according to its parton-to-photon fragmentation function, $D_{a\to\gamma}(z)$, the probability density for finding a photon in a parton of type a.

Although each individual contribution to this cross section is divergent, the physical cross section remains finite: the virtual graphs (represented by the first term in Equation 3.2) contain singularities due to soft gluon radiation and collinear parton emission which cancel against poles from the bremsstrahlung process (the second term in Equation 3.2) once the phase space of the additional parton is integrated out. In order to make this cancellation of poles more explicit, the divergent part of the bremsstrahlung cross section can be isolated and included with the contribution from the virtual graphs [34]. After these purely QCD infrared poles have cancelled there remain quark–photon singularities which occur as the quark and photon become collinear. These 'mass' singularities are factorisable, thus can be subtracted and absorbed into a redefined set

of fragmentation functions (using the factorisation theorem [35]), so that

$$
\begin{aligned}
\mathrm{d}\sigma^{\mathrm{NLO}}\left(n\,\text{jets} + \gamma\right) \;=\; &\Theta\left\{\mathrm{d}\hat{\sigma}_1^{\mathrm{R}}\left(n\,\text{partons} + \gamma\right)\right.\\
&+ \int \mathrm{d}\hat{\sigma}_0^{\mathrm{R}}\left([n+1]\,\text{partons} + \gamma\right)\\
&\left.+ \sum_a \frac{\mathrm{d}\hat{\sigma}_0\left([n+1]\text{partons}\right)}{\mathrm{d}E_a}\,\mathrm{d}E_a\,\mathrm{d}z\,\mathrm{d}E_\gamma\,\delta\left(E_\gamma - zE_a\right)\mathcal{D}_{a\to\gamma}(z)\right\}
\end{aligned}
$$

where each term is now finite. The resolved parton cross sections, $\mathrm{d}\hat{\sigma}^{\mathrm{R}}$, are defined such that every parton pair is 'resolved', that is $s_{ij} \equiv (p_i + p_j)^2 > s_{\min}$ for each pair of partons, i and j.

Working with the formalism of the $\overline{\mathrm{MS}}$ renormalisation scheme using $4 - 2\epsilon$ dimensions, the next-to-leading order effective quark fragmentation function, $\mathcal{D}_{\mathrm{q}\to\gamma}$, for a quark of electric charge e_{q} is related to the lowest order 'bare' fragmentation function, $D_{\mathrm{q}\to\gamma}$ by

$$
\mathcal{D}_{\mathrm{q}\to\gamma}(z) = D_{\mathrm{q}\to\gamma}(z) - \frac{1}{\epsilon}\left(\frac{4\pi\mu^2}{s_{\min}}\right)^\epsilon \frac{1}{\Gamma(1-\epsilon)}\left(\frac{\alpha e_{\mathrm{q}}^2}{2\pi}\right)[z(1-z)]^{-\epsilon}\,P_{\mathrm{q}\to\gamma}(z),
$$

where

$$
P_{\mathrm{q}\to\gamma}(z) = \frac{1+(1-z)^2 - \epsilon z^2}{z}
$$

The $1/\epsilon$ divergence present in the above can, in turn, be factorised into the bare fragmentation function, $D(z)$, at the arbitrary factorisation scale μ_F:

$$
\mathcal{D}_{\mathrm{q}\to\gamma}(z) = \underbrace{D_{\mathrm{q}\to\gamma}\left(z,\mu_F\right)}_{\text{Non-Pert. Comp.}} + \underbrace{\left(\frac{\alpha e_{\mathrm{q}}^2}{2\pi}\right)\left\{\left(\frac{1+(1-z)^2}{z}\right)\log\left(\frac{s_{\min}z(1-z)}{\mu_F^2}\right) + z\right\}}_{\text{Perturbative Component}}. \tag{3.3}
$$

$\mathcal{D}(z)$ should, however, remain independent of the unphysical factorisation scale, μ_F, since it arises only through a shuffling of terms between the non-perturbative fragmentation function, D, and the perturbative contribution to $\mathcal{D}$. This implies that $D(z,\mu_F)$ must satisfy an evolution equation determined by the perturbative component of $\mathcal{D}$:

$$
\frac{\partial D_{\mathrm{q}\to\gamma}(z,\mu_F)}{\partial \log(\mu_F^2)} = \left(\frac{\alpha e_{\mathrm{q}}^2}{2\pi}\right)\left(\frac{1+(1-z)^2}{z}\right). \tag{3.4}
$$

Thus a measurement at any given factorisation scale can be related to a measurement

at any other given scale.

Due to the manner in which soft and collinear poles are regulated in the $\overline{MS}$ scheme, an artificial pole has been introduced in the perturbative component of $\mathcal{D}$ at $z = 1$. This means that the non-perturbative component, $D(z, \mu_F)$, must contain a similar divergence to cancel this, so that overall, $\mathcal{D}(z)$ is well-behaved as $z \to 1$. Also, this effective fragmentation function depends on the parton resolution parameter, $s_{\min}$, but when the fragmentation contribution is combined with the resolved $(n + 1)$ parton $+ \gamma$ cross section, the individual $s_{\min}$ dependencies cancel.

At this order, the effective gluon fragmentation function receives no correction, since there is no gluon-photon collinear singularity. That is

$$\mathcal{D}_{g \to \gamma}(z) = D_{g \to \gamma}(z).$$

However, in higher order calculations, the gluon fragmentation function becomes coupled with the quark fragmentation function through $g \to q \to \gamma$ splittings and has a similar dependence on the factorisation scale. The first process in which this fragmentation function enters is photon + 2-jet production.

3.4 The 'Democratic' Photon Isolation Algorithm

As was stated in Chapter 1, previous analyses of photon + jet events at LEP looked only at events where the photon was almost completely isolated from the hadronic debris, thus virtually eliminating the fragmentation contribution [17, 18]. The elaborate two-step photon isolation procedure used in these analyses caused problems when trying to compare the measured photon + jet rates with those predicted by theoretical calculations, prompting the proposal of a new 'democratic' algorithm [33]. This approach considers photon emission as an integral part of the showering process, suggesting that all the final particles in the event, including the photon, should be clustered into jets using a suitable jet-finding algorithm. Events are selected only if they contain a photon possessing a required minimum fraction, z_γ, of the associated

jet's energy:

$$z_\gamma \equiv \frac{E_\gamma}{E_\gamma + E_{\text{had}}} > z_{\text{cut}},$$

where E_γ is the photon energy and E_{had} is the energy of all accompanying hadrons in the 'photon jet'. A $z_{\text{cut}} \sim 1$ corresponds to an almost completely isolated photon (*i.e.* the photon *is* the jet). By varying z_{cut}, photons can be selected with the desired degree of isolation.

There are several distinct jet-finding algorithms in use at LEP, the majority of which are termed *successive recombination algorithms*. The essence of these is that a test variable, y_{ij} is constructed from all possible pairs of particles in the event with momenta p_i and p_j. The pair with the smallest y_{ij} are then combined to form a single *pseudo-particle*, provided y_{ij} is less than some threshold parameter, y_{cut}. This is then repeated until no further pairings are possible, the remaining pseudo-particles being the jets.

The Durham, or k_T, algorithm [36] is currently the most popular scheme, on the grounds that:

- it is 'infra-red safe' [37] (it gives equivalent results when either an arbitrarily soft particle is added to the event or an already present particle is split into two almost collinear particles),

- it allows the resummation of the large logarithms appearing in jet-rate calculations,

- it leads to a more intuitive association of particles into jets.

In the Durham scheme, the resolution parameter, y_{ij}, is based on the minimum k_T of each particle with respect to the direction of the other. It is defined as

$$y_{ij} = \frac{\min\left(E_i^2, E_j^2\right)}{E_{\text{c.m.}}^2} 2 \left(1 - \cos\theta_{ij}\right),$$

where $E_{i,j}$ and θ_{ij} are respectively the energies and relative angle between the particle pairs in the e^+e^- centre of mass frame. Particle pairs are combined by adding their
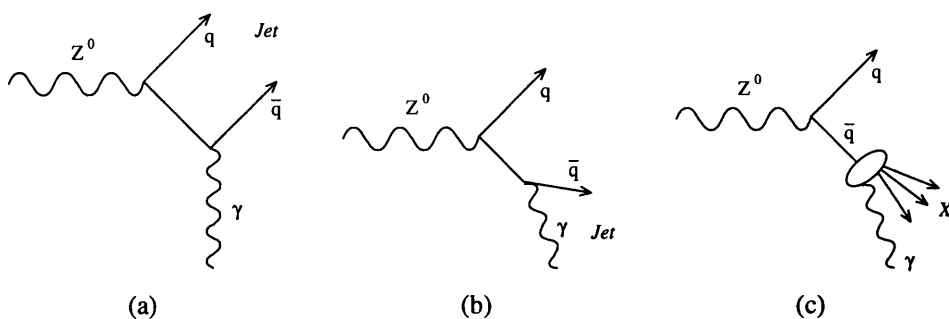
Figure 3.1: The three lowest order contributions to the 1-jet + photon cross section.

4-momenta according to:

$$E_{\text{new}} = E_i + E_j$$

$$\vec{p}_{\text{new}} = \frac{E_{\text{new}}}{|\vec{p}_i + \vec{p}_j|} (\vec{p}_i + \vec{p}_j),$$

the so-called E-0 scheme.

3.5 The Photon + 1-jet Cross Section

Given that there is no $(e^+e^- \rightarrow \gamma + 1 \text{ parton})$ process, the tree-level contribution to the photon + 1-jet cross section (Equation 3.1) and its one-loop correction terms (the first term in Equation 3.2) vanish. The first non-trivial contributions to the cross section are thus from $e^+e^- \rightarrow q\bar{q}\gamma$ and $e^+e^- \rightarrow q\bar{q}$, where one of the quarks fragments into a photon. In the first case, the two quarks can either combine to form a single jet leaving the photon completely isolated (shown schematically in Figure 3.1a), or the photon may be combined with a soft quark to produce a jet (Figure 3.1b). Figure 3.1(c) represents the $e^+e^- \rightarrow q\bar{q}$ contribution where one of the quarks produces a photon during fragmentation. The quark-to-photon fragmentation function is thus present in the lowest order contributions to the 1-jet + photon cross section making the 1-jet + photon rate especially sensitive to it.

The contribution from the $e^+e^- \rightarrow q\bar{q}\gamma$ process to the photon + 1-jet rate can be

obtained by integrating the differential cross section (for massless quarks of charge e_q)

$$\frac{1}{\hat{\sigma}_0} \frac{d^2\sigma}{dx_q dx_{\bar{q}}} = \left(\frac{\alpha e_q^2}{2\pi}\right) \frac{x_q^2 + x_{\bar{q}}^2}{(1 - x_q)(1 - x_{\bar{q}})},$$

where the parton energy fractions are given by $x_q = 2E_q/\sqrt{s}$, $x_{\bar{q}} = 2E_{\bar{q}}/\sqrt{s}$ and $x_\gamma = 2 - x_q - x_{\bar{q}}$. In terms of these energy fractions, the scaled pair invariant masses are given by

$$y_{q\gamma} = 1 - x_{\bar{q}}, \quad y_{\bar{q}\gamma} = 1 - x_q, \quad y_{q\bar{q}} = 1 - x_\gamma,$$

where $y_{ij} \equiv s_{ij}/s$ (s_{ij} is the parton resolution parameter introduced above). By demanding that $s_{ij} > s_{\min}$ for all partons i and j, the singularities in the matrix element along $x_q = 1$ (collinear anti-quark and photon) and $x_{\bar{q}} = 1$ (collinear quark and photon) are avoided.

Working with the Durham scheme and a jet resolution parameter $y_{cut} \leq 1/3$, for photons with an energy fraction greater than z_{cut}, the 1-jet + photon region is defined by

$$1: \quad \min\left(\frac{x_q}{x_{\bar{q}}}, \frac{x_{\bar{q}}}{x_q}\right) \cdot y_{q\bar{q}} < y_{cut}$$

$$2: \quad \min\left(\frac{x_q}{x_\gamma}, \frac{x_\gamma}{x_q}\right) \cdot y_{q\gamma} < y_{cut} \quad \text{and} \quad \frac{E_\gamma}{E_\gamma + E_q} > z_{cut}$$

$$3: \quad \min\left(\frac{x_{\bar{q}}}{x_\gamma}, \frac{x_\gamma}{x_{\bar{q}}}\right) \cdot y_{\bar{q}\gamma} < y_{cut} \quad \text{and} \quad \frac{E_\gamma}{E_\gamma + E_{\bar{q}}} > z_{cut}$$

The corresponding Dalitz plot is shown in Figure 3.2 for a y_{cut} of 0.1 and a z_{cut} of 0.7. In region 1 the quark and antiquark combine to form a jet, while in regions 2 and 3 the photon coalesces with the quark or antiquark respectively to form a mixed electromagnetic / hadronic cluster.

In the region of phase space where the quark or antiquark combine with the photon (regions 2 and 3), the fraction of electromagnetic energy in the cluster, z, is related to x_q and $x_{\bar{q}}$ by

$$z = \frac{2 - x_q - x_{\bar{q}}}{2 - x_{\bar{q}}} \tag{3.5}$$
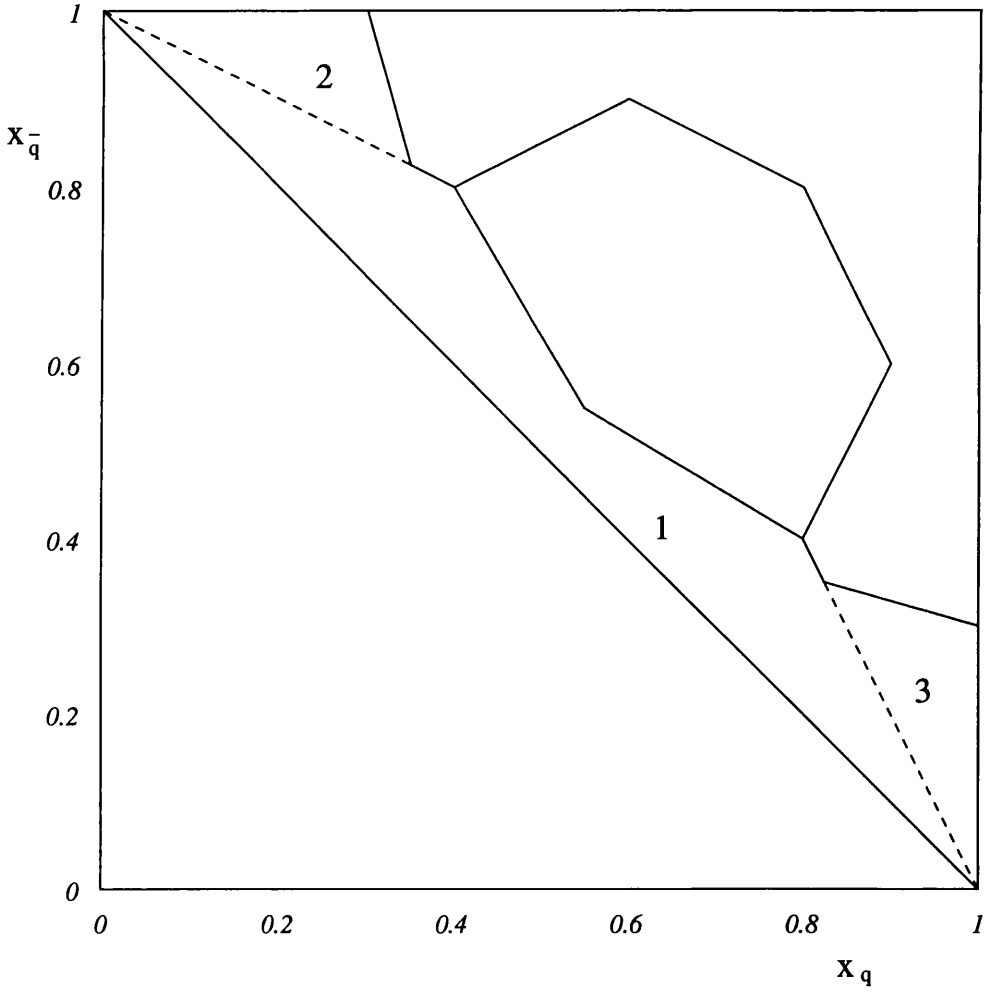
Figure 3.2: Dalitz plot for the $q\bar{q} + \gamma$ final state in terms of the quark and antiquark energy fractions, x_q and $x_{\bar{q}}$. The regions 1, 2 and 3 show the 1-jet + photon phase space for $y_{cut} = 0.1$ and $z_{cut} = 0.7$ in the Durham scheme. Region 1 is where the quark and antiquark combine to form a jet; regions 2 & 3 are where the quark and antiquark, respectively combine with the photon

in region 2 and by Equation 3.5 with x_q and $x_{\bar{q}}$ exchanged in region 3. By integrating over either x_q or $x_{\bar{q}}$ it is possible to obtain the 1-jet + photon cross section as a function of z.

In order to turn this analytic form into a physical cross section, it is necessary to know the process independent quark-to-photon fragmentation function, $D_{q \to \gamma}(z, \mu_F)$ in the $\overline{MS}$ scheme. The next chapter uses the above calculation, in the context of a Monte Carlo program, to measure the non-perturbative component of the fragmentation function from the production rate of photon + 1-jet events.

Chapter 4

A Measurement of the Photon Fragmentation Function

Using the cross section calculations introduced in the previous chapter, this chapter describes a measurement of the non-perturbative contribution to the quark-to-photon fragmentation function. After describing the procedure used to select hadronic events and the subsequent identification of energetic photons, the methods used to estimate the contamination of the selected sample from non-prompt photons are discussed. A procedure is then introduced to correct the data for acceptance limitations of the apparatus and possible reconstruction inefficiencies. A simple form for the non-perturbative contribution to the quark-to-photon fragmentation function is fitted to the data.

4.1   Selection of Photon Events

Hadronic Event Selection

Hadronic events from $Z^0 \to q\bar{q}$ decays are selected by demanding they contain at least four charged tracks originating from within a cylinder, centred on the interaction point, of radius 2 cm and a length of ± 10 cm along the beam direction. Each track should have a polar angle θ such that $|\cos\theta| < 0.95$, and comprise at least four reconstructed TPC coordinates. The total charged energy in the event must exceed 10% of the centre

of mass energy. In addition, events must contain at least 15 reconstructed objects (either charged or neutral), with the total visible energy greater than 40% of the centre of mass energy. This ensures that contributions from $Z^0 \rightarrow \tau^+\tau^-$ or $\gamma\gamma$ interactions are negligible (less than 0.05 % and 0.08 % respectively), while selecting hadronic events with an efficiency of 97.3 % [17]. A polar angle cut on the thrust axis of the event, $|\cos\theta_{\text{thrust}}| \leq 0.9$, is applied to ensure that the event is well-contained within the detector.

Photon Identification

As described in Chapter 2, during the reconstruction of an event, storeys in the electromagnetic calorimeter (ECAL) with a significant energy deposition (the threshold is 30 MeV) are grouped together into clusters. These clusters may be large, with energy from photons and hadronic interactions often being merged. Photon candidates are thus selected from more compact clusters, formed after a second, more stringent clustering scheme has been applied (Section 2.3.3). Candidate clusters must not be associated with a charged track and must have an energy of 5 GeV or more. The vector from the interaction point to the barycentre of a cluster should have a polar angle θ_γ such that $|\cos\theta_\gamma| < 0.95$, ensuring the cluster is completely contained within the ECAL. Candidate clusters are further constrained in azimuth to avoid the 'cracks' between individual ECAL modules, ensuring that their energy is measured in a fully efficient region of the calorimeter. Similarly, clusters comprising towers from the overlap area between the barrel and end-cap sections are also excluded, since large correction factors must be applied to energies measured in this region.

The dominant background to the single photon selection is from the decays of energetic π^0's into two photons where the photon depositions overlap in the ECAL (see Section 4.2). This is reduced substantially by demanding that only one 'compact' cluster has been extracted from the original 'large' cluster, thus removing cases where the two decay photons are resolved by the second clustering algorithm.

In some cases the photon clusters overlap to the extent that they are not resolved by the second clustering algorithm. The background is thus further reduced by studying

the energy distribution within the cluster. The matrix of second order moments of the energy weighted coordinates of each storey in the cluster is calculated then diagonalised to give two values, the major and minor moments of the cluster. For single photon clusters observed in $e^+e^- \to e^+e^-\gamma$ and $e^+e^- \to \mu^+\mu^-\gamma$ events, the distribution of the major moment has been found to be different for clusters situated in the barrel and end-cap sections of the calorimeter, as shown in Figure 4.1. A similar discrepancy was observed for fully simulated Monte Carlo events. The energy dependence of the major moments of photon clusters in the above types of event was parameterised using the empirical form

$$A + \frac{1}{B + C \cdot \text{Energy}}.$$

These are shown as the solid lines in Figure 4.1. The distribution of the major moments was 'renormalised' to give a Gaussian distribution, centred on zero and with a width of one, independent of the energy or polar angle of the photon. That is,

$$\sigma_L = \frac{W_{meas} - W_{param}}{\sigma_{W_{param}}}$$

where σ_L is the renormalised major moment, W_{meas} and W_{param} are the measured and parameterised major moments, respectively, and $\sigma_{W_{param}}$ is the width of the parametrised distribution. In the case of Monte Carlo events, the distribution was adjusted to reproduce the data. Photon clusters are kept only if their renormalised major moment, σ_L satisfies $-3 < \sigma_L < 2$.

The efficiency of this photon selection procedure was measured using a sample of almost 23 000 simulated events, each containing a final state radiation (FSR) photon with an energy of at least 5 GeV. This corresponds to a sample equivalent to 2.7 million hadronic Z^0 decays. The efficiency is found to be 55 % and is almost independent of the photon energy. 15 % of the inefficiency comes from photon conversions and the $|\cos\theta_\gamma| < 0.95$ cut, 20 % is due to the requirement that the cluster is not linked to a charged track, near a 'crack', or in the overlap region, and 10 % is caused by the remaining selection criteria (a unique 'compact' cluster for each 'large' cluster, and the cut on the cluster's major moment) but this does reduce the background by a factor of 3 at 20 GeV, falling to a factor of 2 at 30 GeV.
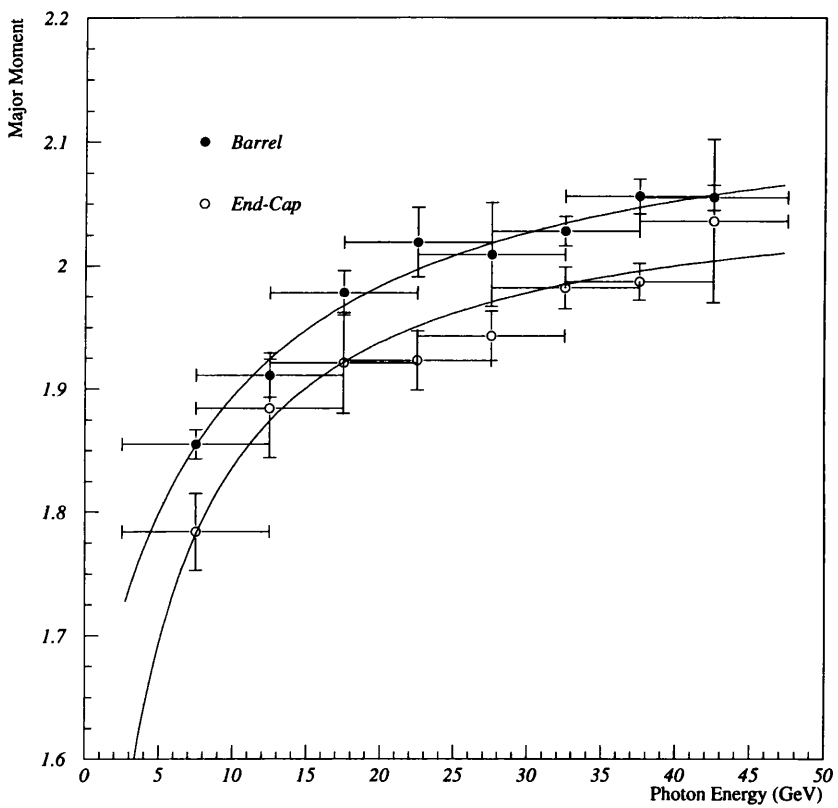
Figure 4.1: The major moment of single photon clusters in both barrel and end-cap regions of the ECAL as a function of the photon energy
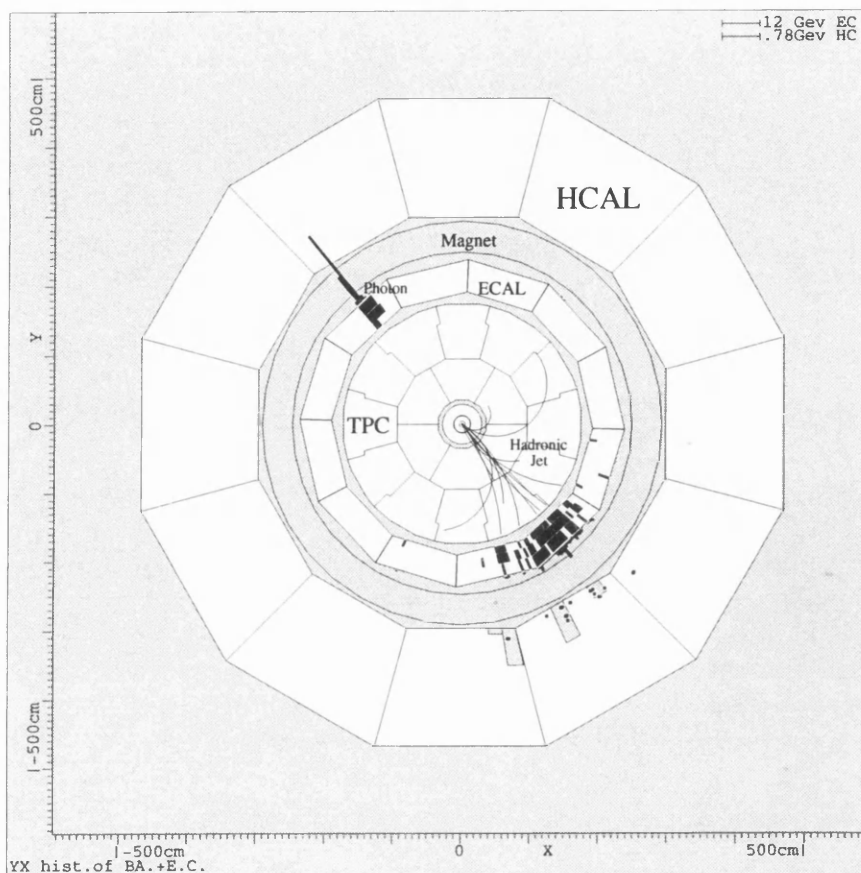
Figure 4.2: A 1-jet + photon event. The HCAL, ECAL and TPC subdetectors are labelled, as is the superconducting magnet coil.

Figures 4.2 and 4.3 show examples of events selected in this manner where the photon is almost completely isolated (that is, $z \sim 1$).

4.2   Background Estimation and Subtraction

As discussed above, the non-FSR background in the selected sample of events arises mainly from the decays of neutral hadrons (π^0, η, ...) into two or more photons where the photon depositions completely overlap in the electromagnetic calorimeter. Their contribution together with initial state radiation (ISR) and misidentified neutral hadrons is determined using events generated with JETSET and passed through a full simulation
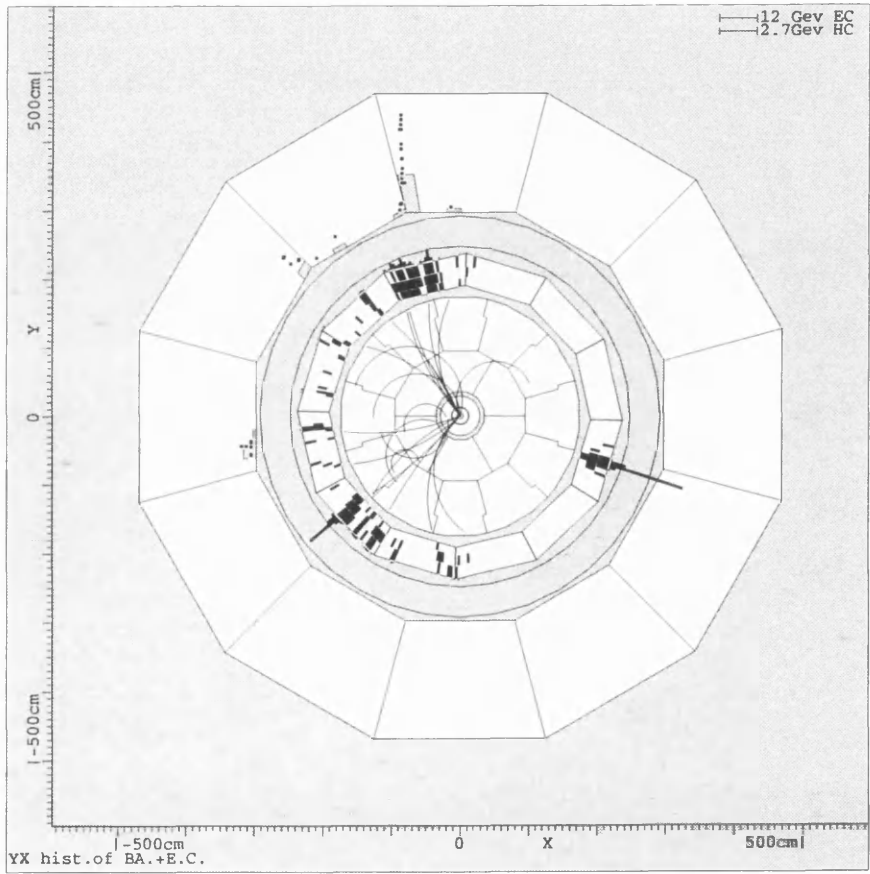
Figure 4.3: A 2-jet + photon event
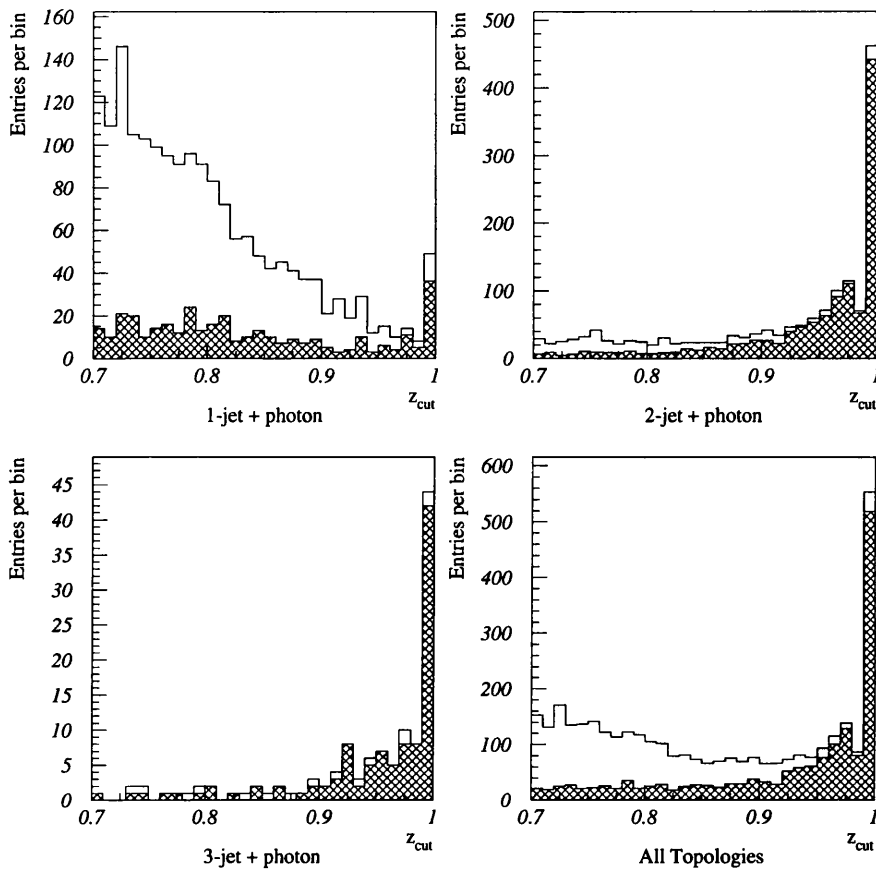
Figure 4.4: The number of events passing the selection criteria for a 'photon + n-jet event'. The contribution from FSR photons is hatched.

of the ALEPH detector. The estimated background is subtracted statistically from the data, bin-by-bin in z_γ. Figure 4.4 shows the relative proportions of FSR 'signal' events to the non-FSR 'background' for the various event topologies over a z_γ range from 0.7 to 1 at a y_{cut} of 0.03. The relative background is seen to be largest in events comprising a 'photon jet' plus one other hadronic jet. 88 % of this background arises from $\pi^0 \to 2\gamma$ decays. Two independent methods were applied to determine the precision of the π^0 simulation in the Monte Carlo model.

In the first, it was noted that according to parton shower models, at least 90 % of π^0's produced with $x_E > 0.7$ ($x_E = E_{\pi^0}/E_{beam}$) originate from primary quark fragmentation or strong decays of resonances [38]. Isospin symmetry would imply that their production rate should be equal to the average of π^+ and π^- in the same kinematic

region. The latter has been measured in ALEPH using charged tracks identified as $\pi^\pm$ by dE/dx measurements for z values up to 0.8 . The result agrees with JETSET predictions to $\pm 6\%$ in the range $0.6 \leq z \leq 0.8$, as shown in Figure 4.5. Assuming the efficiency of identifying $\pi^\pm$ is well simulated, it can be concluded that JETSET describes inclusive π^0 production to an accuracy of $\sim 6\%$ in this z range also.

The second method is less precise, but is valid over the full range of z values. Energetic π^0's (and η's) are reconstructed in 2-jet events when one photon converts in the materials surrounding the interaction region to produce an e^+e^- pair. Candidate pairs are selected if their momenta are greater than 1 GeV and their invariant mass less than 200 MeV. The simulation of such pairs agrees well with the data, both in rate (to 1 % up to 20 GeV) and in radial distribution [39]. After selecting an e^+e^- pair, the photon closest to it was used to determine the invariant mass of the $e^+e^-\gamma$ combination. Figure 4.6 shows the invariant mass distributions obtained for all such combinations with an energy greater than 30 GeV from both the data (609 combinations) and the JETSET simulation (955 combinations). The π^0 and η peaks are clearly visible above a small background. After fitting these spectra using a Gaussian for the π^0 peak and a polynomial for the background, the ratio of the JETSET prediction to the data is found to be 1.04 ± 0.12 for $z > 0.7$.

The remaining background of neutral hadrons (e.g. neutrons, K^0's) misidentified as photons is estimated from the same sample of simulated events. This background is about 2 % for 2-jet topologies and very small for the others, independent of y_{cut}.

These results confirm the validity of the JETSET Monte Carlo for the non-FSR background estimation and its subsequent statistical subtraction.

4.3 Acceptance Corrections

In order to compare the data with QCD matrix element predictions, the measured photon + n-jet rates must be corrected for any detrimental detector and event reconstruction effects, such as the limited geometrical acceptance, photon identification inefficiency, and interactions of particles within the detector. These can be estimated using a sample of fully reconstructed hadronic events, each containing a prompt photon, generated
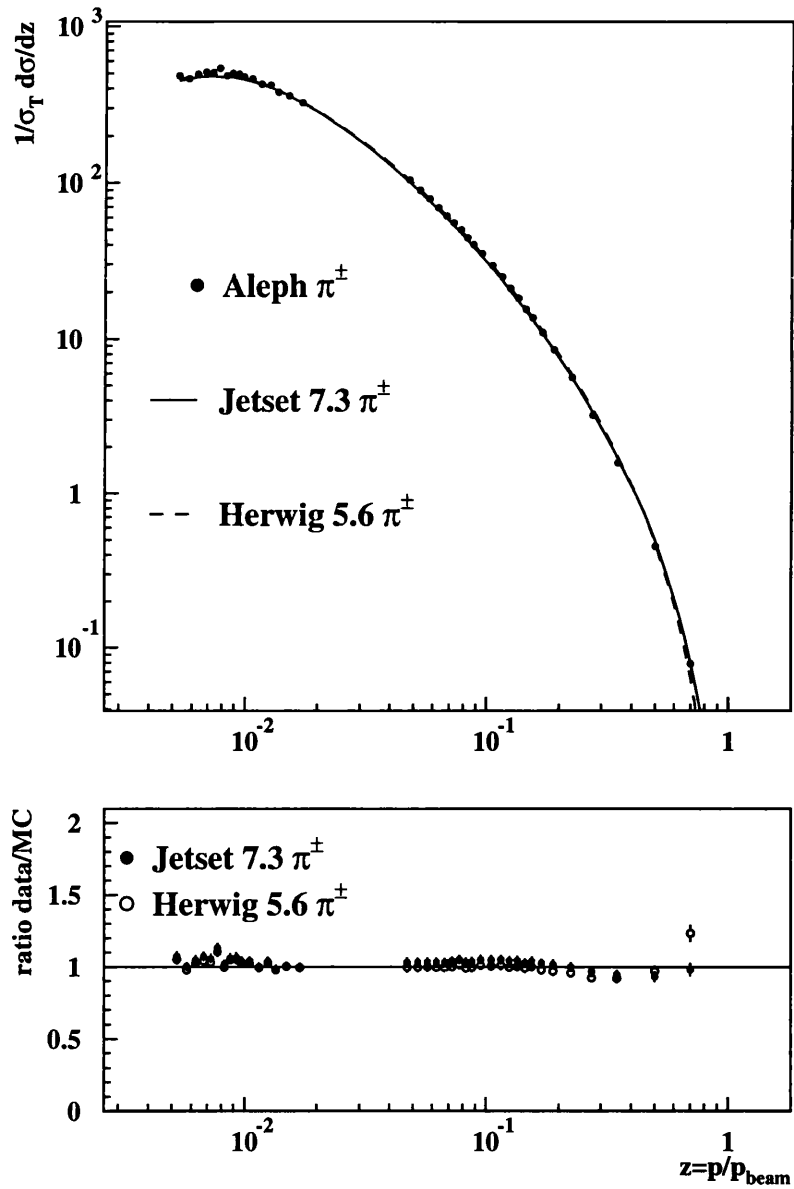
Figure 4.5: Comparison of the measured $\pi^{\pm}$ production rate with the corresponding JETSET and HERWIG predictions.
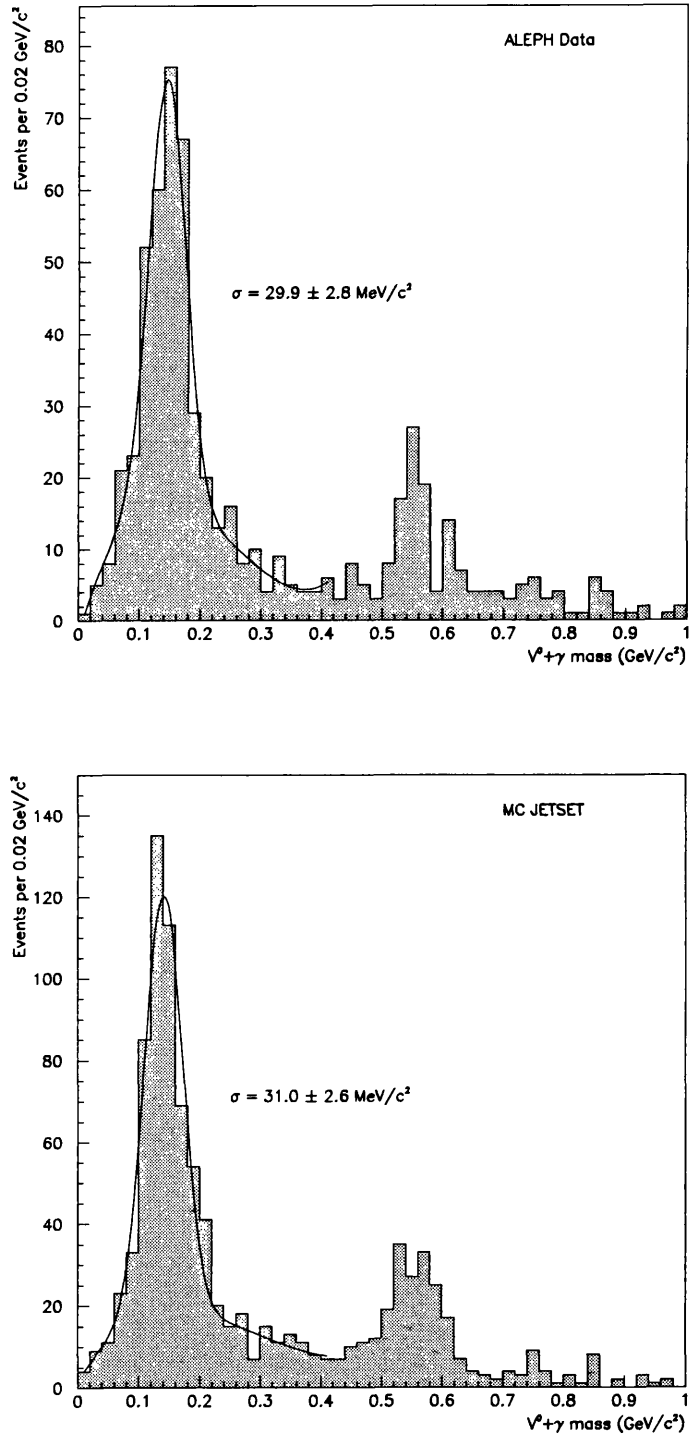
Figure 4.6: The invariant mass of energetic $e^+e^-\gamma$ systems from data (upper) and a JETSET simulation (lower).

with a parton shower Monte Carlo and processed with a detailed simulation of the ALEPH detector. Samples of events generated with ARIADNE 4.2, HERWIG 5.6 and JETSET 7.3 corresponding to 2.7, 2.5 and 2.8 million hadronic events, respectively, were used for this. By comparing the (γ_{FSR} + jets) rates at generator level and the resulting (γ_{Reco} + jets) rates after the detector simulation and event reconstruction, the following matrix equation can be constructed

$$\underbrace{\left(\gamma_{\text{Reco}} + j \text{ jets}\right)}_{\text{Detector Level}} = \sum_i \underbrace{\left(\gamma_{\text{FSR}} + i \text{ jets}\right)}_{\text{Generator Level}} \mathcal{P}_{i \to j}.$$

The leading diagonal components of $\mathcal{P}$ correspond to efficiency and acceptance effects, while the off-diagonal components describe how event topologies are distorted by the finite detector resolution and imperfect event reconstruction. By inverting the above relation, the inverse matrix, $\mathcal{P}^{-1}$, can be applied to the rates measured in data (after subtracting the estimated non-prompt background) to deduce what the undistorted, full-acceptance photon + jet rates would have been.

Applying the principal of 'local parton–hadron duality' (LPHD) [40], whereby the hadronic jets are mapped onto the hard partons of the matrix element calculation, these corrected rates can now be compared with the theoretical predictions. A different matrix, $\mathcal{P}^{-1}$, must be computed for each y_{cut} value and z_γ bin chosen.

The statistical uncertainties in the corrected data rates are evaluated using a simple error propagation of the form

$$\delta(\mathcal{P}^{-1}) = \mathcal{P}^{-1}(\delta\mathcal{P})\mathcal{P}^{-1},$$

where it is assumed that each element of $\mathcal{P}^{-1}$ is independent. Although not strictly correct, the resulting error estimates for the components of $\mathcal{P}^{-1}$ are conservative as they are dominated by the large uncertainties arising from low data statistics.

Since an $\mathcal{O}\left(\alpha\alpha_S\right)$ matrix element calculation can produce a maximum of four partons in the final state, jet clustering was performed using a range of y_{cut} values which restricted the number of jets in the event to be, at most, four (*i.e.* a photon 'jet' plus three others). With the Durham (k_T) algorithm, this corresponds to y_{cut} values

z_γ range	JETSET	ARIADNE	HERWIG
0.70 − 0.75	2.52 ± 0.88	3.02 ± 1.02	2.02 ± 0.76
0.75 − 0.80	1.58 ± 0.80	1.32 ± 0.66	1.62 ± 0.82
0.80 − 0.85	1.46 ± 0.50	1.80 ± 0.58	1.90 ± 0.64
0.85 − 0.90	0.88 ± 0.40	0.98 ± 0.44	1.08 ± 0.48
0.90 − 0.95	0.96 ± 0.36	0.74 ± 0.26	0.90 ± 0.32
0.95 − 1.00	2.74 ± 0.56	2.64 ± 0.52	2.66 ± 0.54

Table 4.1: The fully corrected differential 1-jet + photon rates obtained at a y_{cut} of 0.05, the acceptance correction matrix being derived using each of the three parton shower Monte Carlo models listed

≥ 0.01. This has the consequence of restricting $\mathcal{P}$ to be a 3×3 matrix.

In general, $\mathcal{P}$ was found to be a very symmetric matrix, with much larger components along the leading diagonal than elsewhere. Combined with the restriction that $\mathcal{P}$ was of order 3, this resulted in a stable system when the matrix inversion was performed.

Table 4.1 lists the fully corrected differential one-jet + photon rates obtained using a y_{cut} of 0.05. The acceptance correction was done using each of the Monte Carlo models, JETSET, ARIADNE and HERWIG in turn. Clearly, consistent results were obtained with each.

4.4 Measuring the Quark-to-Photon Fragmentation Function

To obtain an estimate of the possible magnitude of the non-perturbative contribution to the effective quark-to-photon fragmentation function $D_{q \to \gamma}(z, \mu_F)$, a fixed order $\mathcal{O}(\alpha\alpha_S)$ Monte Carlo simulation was performed using the EEPRAD program [15, 33] where only the perturbative contribution to Equation 3.3 was considered. Figure 4.7 shows the measured 1-jet + photon rate, differential in z_γ, with the matrix element predictions obtained using three different values for the factorisation scale, μ_F. Only the first five data bins (from $z_\gamma = 0.7$ to $z_\gamma = 0.95$) should be compared with the predictions, as the final bin ($0.95 < z_\gamma < 1$) contains the contribution from the
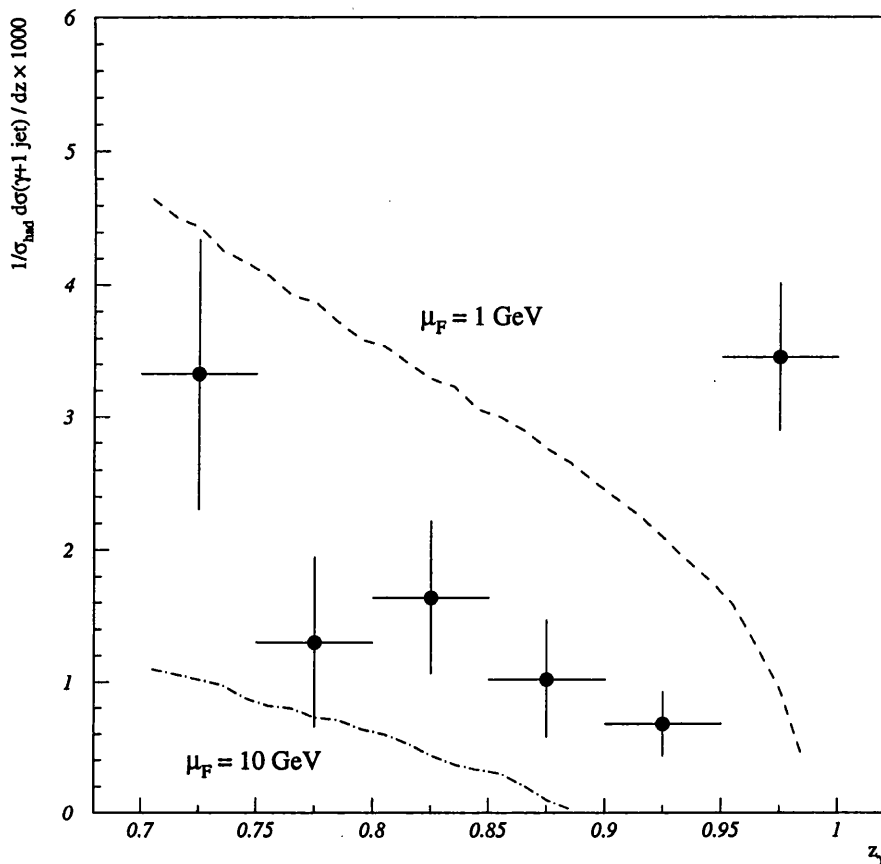
Figure 4.7: The 1-jet + photon cross section, differential in z_γ and normalised to the total hadronic cross section, compared with matrix element predictions obtained using only the perturbative contribution to the effective quark to photon fragmentation function. A y_{cut} of 0.1 was used.

component associated with completely isolated photon production ($z_\gamma \sim 1$) which arises when the quark and antiquark combine to form a jet (Figure 3.1a). This term was not included in the matrix element calculation. As expected from Equation 3.3 the prediction is strongly dependent on μ_F and is divergent for $z_\gamma \to 1$.

The simplest possible non-perturbative contribution to the effective quark to photon fragmentation function which, in the $\overline{MS}$ scheme, satisfies the leading order evolution equation (Equation 3.4), while simultaneously cancelling the divergence at $z = 1$ in
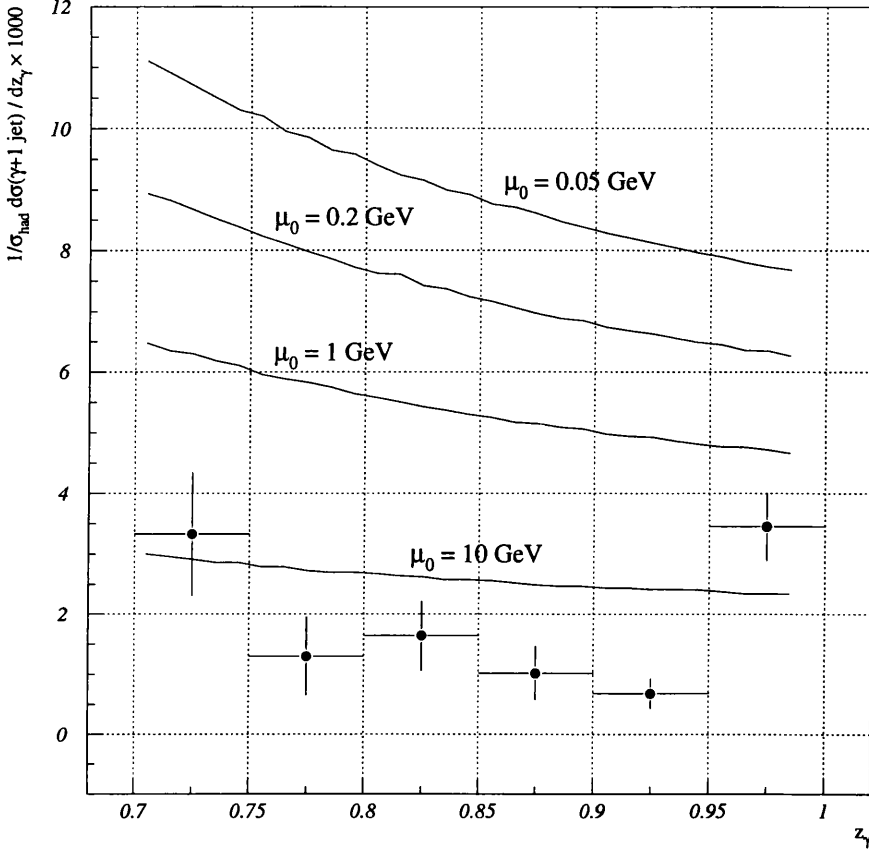
Figure 4.8: The differential 1-jet + photon cross section at a y_{cut} of 0.1. The solid lines indicate predictions from a matrix element calculation, including a simple non-perturbative component, using a range of values for μ_0, the scale below which the physics becomes non-perturbative.

the perturbative contribution, is given by

$$D_{q\to\gamma}(z, \mu_F) = \left(\frac{\alpha e_q^2}{2\pi}\right) \frac{1 + (1-z)^2}{z} \log\left(\frac{\mu_F^2}{\mu_0^2(1-z)^2}\right), \qquad (4.1)$$

Figure 4.8 shows the effect of adding this non-perturbative component to the effective quark to photon fragmentation function using various choices for the scale μ_0, while keeping μ_F fixed at 10 GeV. As expected, the $z \to 1$ divergence has now been removed.

Since a low value of μ_0 gives a matrix element prediction which describes the shape of the data well but has a very poor overall normalisation with respect to the data, a
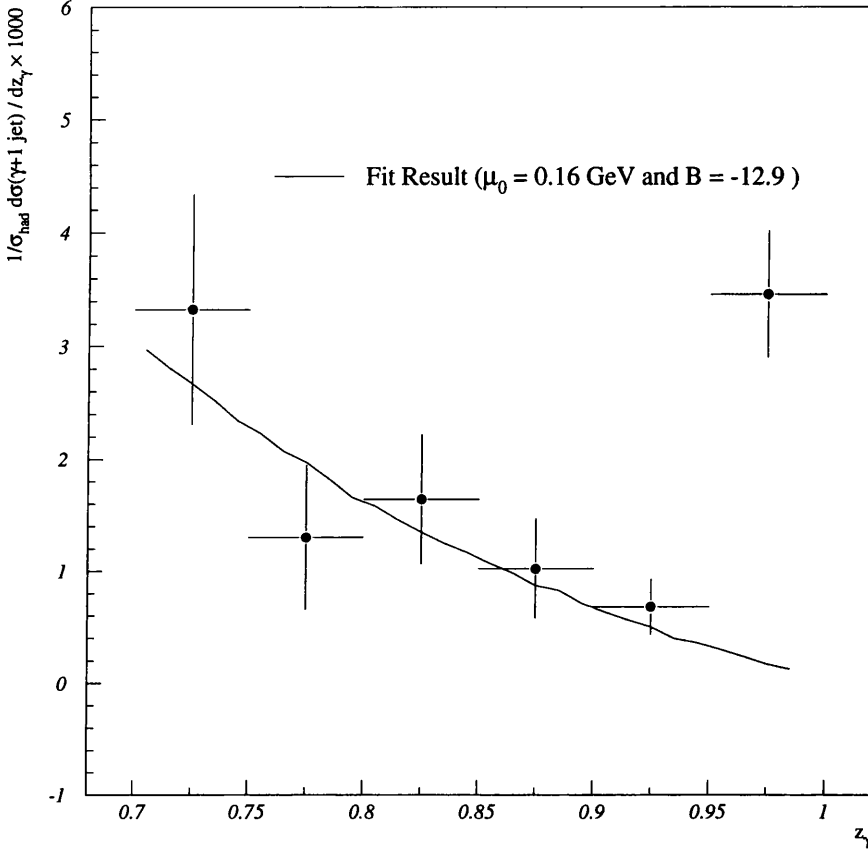
Figure 4.9: The 1-jet + photon cross section, differential in z_γ, at a y_{cut} of 0.1. The solid line is the best fit obtained, allowing μ_0 and B to vary, but keeping μ_F fixed at 10 GeV (Equation 4.2).

constant term was added to the non-perturbative component given in Equation 4.1 such that it still satisfies the evolution equation.

$$D_{q \to \gamma}(z, \mu_F) = \left(\frac{\alpha e_q^2}{2\pi} \right) \left\{ \frac{1 + (1-z)^2}{z} \log \left(\frac{\mu_F^2}{\mu_0^2(1-z)^2} \right) + B \right\} \qquad (4.2)$$

A χ^2 minimisation fit was then performed to the data, allowing μ_0 and B to vary. The best fit was obtained with $\mu_0 = 0.16 \pm 0.20\,GeV$ and $B = -12.9 \pm 2.9$. This result is shown in Figure 4.9.

To test the independence of this result over y_{cut}, the fit was repeated at three other

y_{cut}	Fit Results		
	B	μ_0	$\chi^2/3$
0.01	-12.0 ± 3.0	0.24 ± 0.31	0.90
0.05	-12.5 ± 3.0	0.20 ± 0.25	0.33
0.1	-12.9 ± 2.9	0.16 ± 0.20	0.35
0.3	-12.9 ± 2.7	0.16 ± 0.18	0.65

Table 4.2: Fit results for the non-perturbative component of the quark-to-photon fragmentation function (Equation 4.2) over a range of y_{cut} values

y_{cut} values. Consistent values were found, as listed in Table 4.2. Figure 4.10 shows the predicted rates at various y_{cut} values using the values $B = -12.4$ and $\mu_0 = 0.20\,GeV$. Good agreement is seen with the data over a wide range of y_{cut} values.

4.5 Summary

From a sample of almost 1.2 million hadronic Z^0 decays, a 'democratic' approach has been applied to select events comprising a 'photon jet' plus one other hadronic jet, a topology particularly sensitive to the quark-to-photon fragmentation function. After statistically subtracting the estimated non-FSR background, the data were corrected for any detrimental detector effects and reconstruction inefficiencies. Within the theoretical framework of the $\overline{MS}$ renormalisation scheme, an $\mathcal{O}(\alpha\alpha_S)$ matrix element calculation has been used to measure the quark to photon fragmentation function at leading order in the high z region. This measurement provides a better description of quark bremsstrahlung in electron-positron collisions then was hitherto available and should be of use in describing the bremsstrahlung contribution to prompt photon production in high energy hadron-hadron collisions.
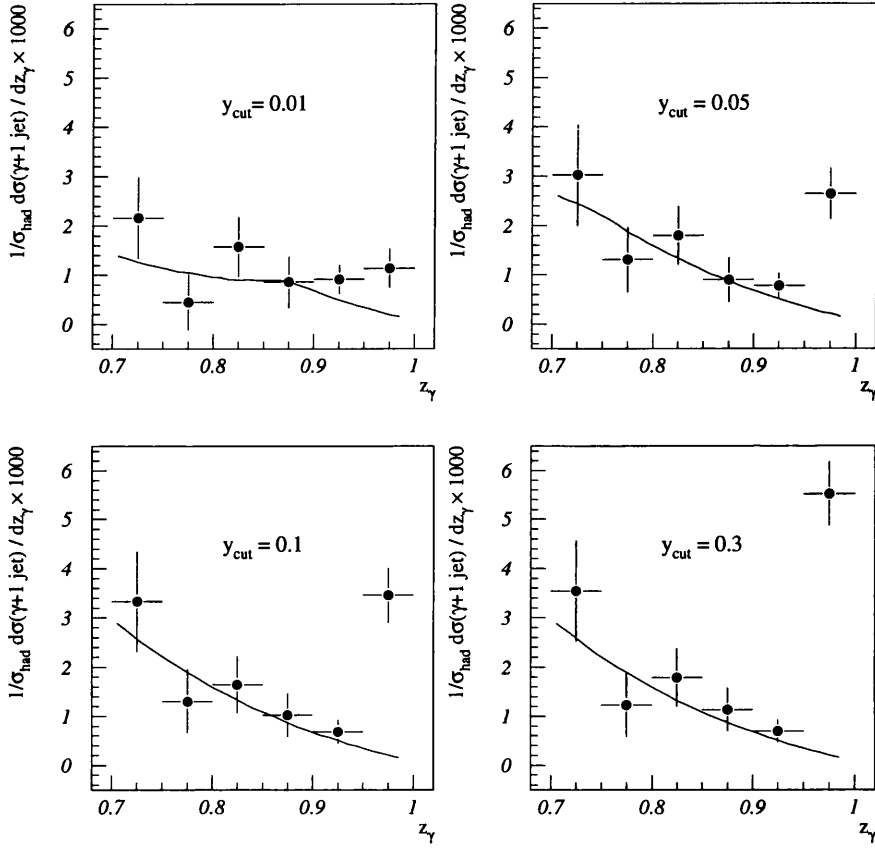
Figure 4.10: The normalised 1-jet + photon differential rate at y_{cut} values of 0.01, 0.05, 0.1 and 0.3. The solid line shows the matrix element prediction obtained using the non-perturbative component determined at $y_{cut} = 0.1$.

Chapter 5

Isolated Photon Production in

Hadronic Events

As discussed in Chapter 1, all previous studies of quark bremsstrahlung at LEP were confined to isolated photons. Comparisons were made with parton shower models and QCD matrix element calculations [17, 18]. Although large discrepancies were observed between the measured $\gamma + 1$ jet rate and the corresponding theoretical predictions, some collaborations proceeded to make measurements of the electroweak couplings of u- and d-type quarks to the Z^0 boson [19], as outlined in Chapter 1. The multi-jet rates ($\gamma+ \geq 2$ jets) were, however, satisfactorily described. The comparisons with QCD parton shower models gave reasonable agreement for all the measured event properties. The disagreement with the matrix element calculations for the one-jet + photon rate is precisely in the region of phase space (well-separated energetic jet and photon) where one might expect this type of calculation to work best, certainly at least as well as, if not better than, parton shower models. This discrepancy between the calculations and the data raised questions about how best to match the theoretical definitions of isolated photons and partons with what is measured in the experiments. The result was the proposal of a new 'democratic' algorithm, introduced in Chapter 3.

This chapter applies the democratic algorithm to select events containing isolated photons ($z_{cut} \sim 1$), where the fragmentation contribution to the cross section is small, rather than photons embedded in hadronic jets (as in the previous chapter), and repeats

some of the comparisons made in previous analyses where events were selected using the two-step isolation cone approach.

5.1   Photon + 1-jet Events

Working to $\mathcal{O}(\alpha\alpha_S)$, events with a jet containing an energetic photon and one other hadronic jet can be formed via the three diagrams shown in Figure 3.1. If the photon is required to be well isolated from the hadronic part of the event, then only the process shown in Figure 3.1(a) contributes. At lowest order, this process is independent of both α_S and the quark to photon fragmentation function, depending only on electroweak coupling constants.

To test the agreement between the data and the $\mathcal{O}(\alpha\alpha_S)$ prediction for this process, the plots showing the differential 1-jet + photon cross sections obtained in the previous chapter were modified to show the effect of the additional component near $z_\gamma = 1$ (Figure 3.1a). The $0.95 < z_\gamma \leq 1$ bin in the data distribution was split into two bins: $0.95 < z_\gamma \leq 0.99$ and $0.99 < z_\gamma \leq 1$. The process corresponding to Figure 3.1(a) was included in the $\mathcal{O}(\alpha\alpha_S)$ calculation. The comparison is shown in Figure 5.1 using four different y_{cut} values. Particularly at higher y_{cut} values, the data point corresponding to the z_γ range $0.95 < z_\gamma \leq 0.99$ is considerably higher than the prediction. It was suggested [41] that this could be caused by the radiation of several soft gluons which become associated with the photon during jet clustering, with the overall effect that the resulting z_γ is changed by a significant amount. Since the $\mathcal{O}(\alpha\alpha_S)$ calculation can accommodate the radiation of at most one gluon, this possibility cannot be included in the matrix element prediction.

This effect was investigated with a parton shower Monte Carlo model. Using only events containing a FSR photon, the final 'on-shell' partons were clustered into jets and the democratic photon isolation criteria applied. The same procedure was applied to the hadrons produced after the fragmentation phase of the model. Figure 5.2 shows the resulting z_γ values for the FSR photons at parton level versus those obtained at hadron level. Clearly this 'smearing' effect is only present at the hadron level, thus ruling out the suggestion that it is due to multiple soft gluon radiation; it is more likely
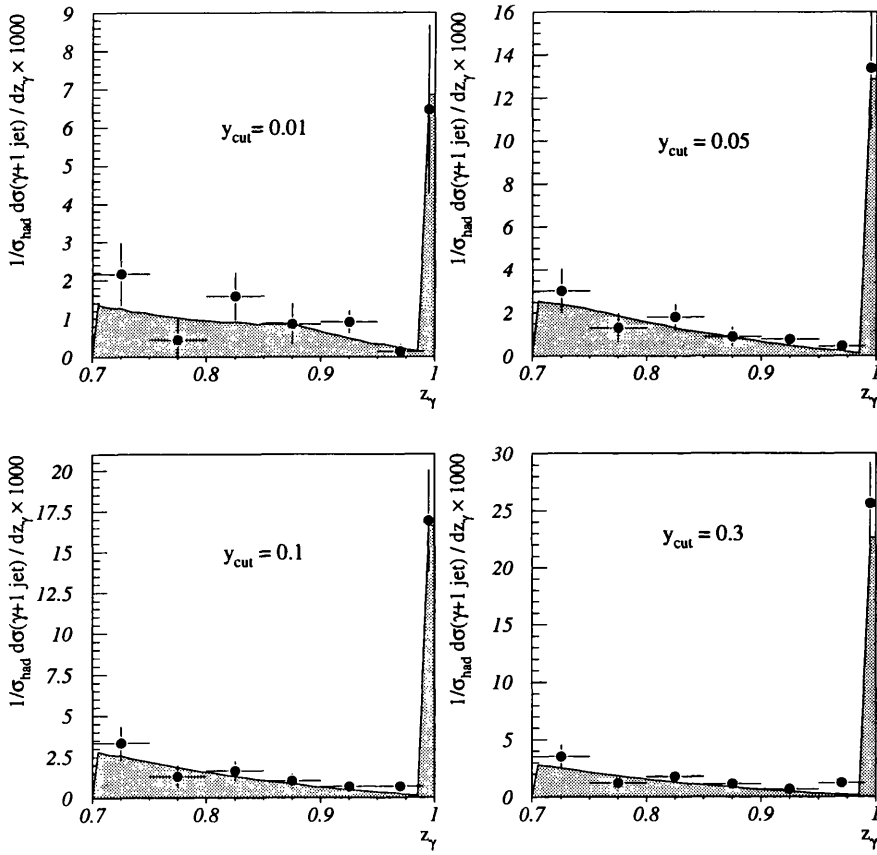
Figure 5.1: The 1-jet + photon rate, differential in z_γ, at four y_{cut} values. The component for isolated photon production ($z_\gamma \sim 1$) is included in the matrix element prediction
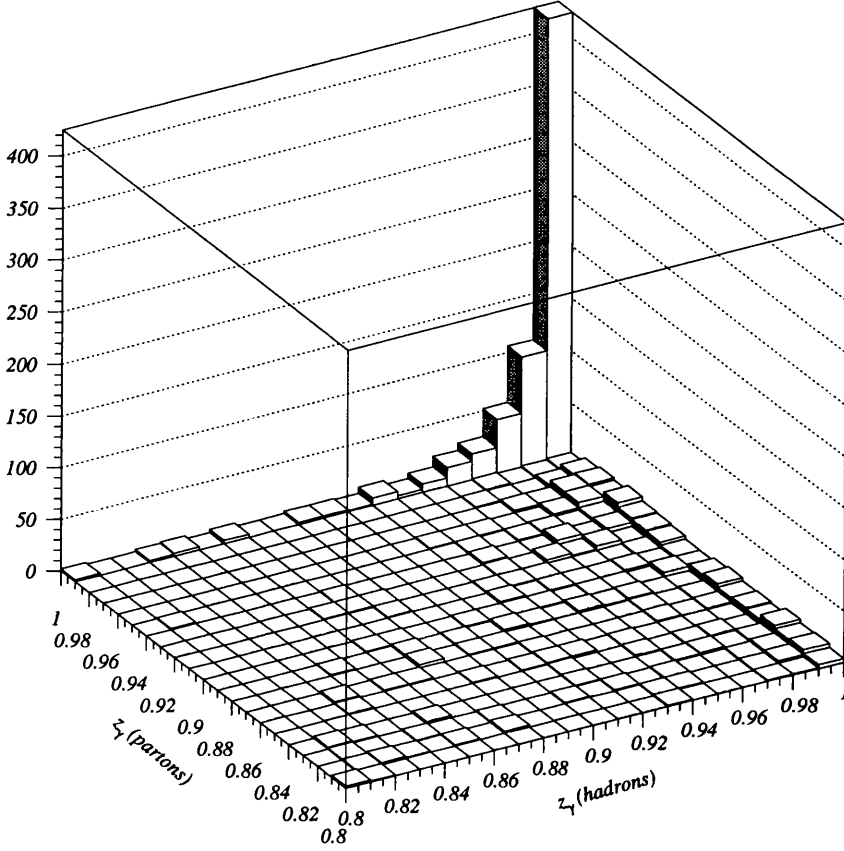
Figure 5.2: The resulting z_γ of FSR photons with jets clustered using 'on-shell' partons and hadrons.

to be due to a misassociation of soft hadrons during the jet clustering. Unfortunately, this excludes the possibility of comparing the measured rates of completely isolated photons ($z_\gamma > 0.99$) with those predicted by the $\mathcal{O}(\alpha\alpha_S)$ calculation, as any 'smearing' effect will cause an apparent reduction in the measured rates.

To overcome this, the measured differential rate was integrated between $z_\gamma = 0.95$ and $z_\gamma = 1$, ensuring that any smearing from $z_\gamma \sim 1$ was included, and the results compared with the equivalent predictions. However, this procedure means that not only the isolated photon component is present, but also a contribution from the quark to photon fragmentation function (both perturbative and non-perturbative components). Figure 5.3 shows the differential 1-jet + photon cross section, integrated from $z_\gamma = 0.95$
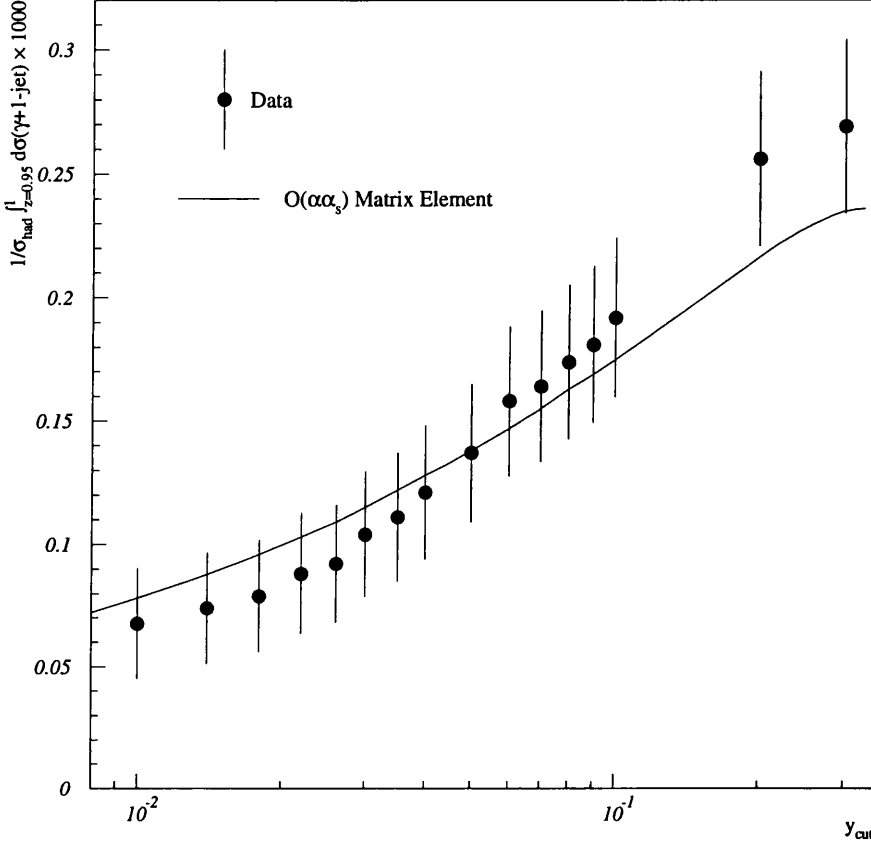
Figure 5.3: The differential 1-jet + photon cross section, integrated from $z_\gamma = 0.95$ to $z_\gamma = 1$. The solid line represents the $\mathcal{O}\left(\alpha\alpha_S\right)$ prediction, using the previously fitted quark to photon fragmentation function, extrapolated to $z_\gamma = 1$.

to $z_\gamma = 1$, over a range of y_{cut} values. Overall, good agreement is found between the matrix element calculation and the data, although a discrepancy is observed at higher y_{cut} values. This may be attributable to missing higher order corrections [41].

5.2   Photon + 2 and 3-jet Events

Unlike the photon + 1-jet case, tree-level diagrams exist for the $e^+e^- \to \gamma + 2$ and 3 parton processes, therefore the quark-to-photon fragmentation function appears only at next-to-leading order. The cross section for $\gamma+ \geq 2$ jets is thus dominated by the

α_S	R_3^γ
0.160	0.156
0.165	0.163
0.170	0.168
0.175	0.187

Table 5.1: Calculated values for R_3^γ as a function of α_S at a $y_{\rm cut}$ of 0.01

lowest order contribution, which occurs only for $z_\gamma \sim 1$. However, since the leading order QCD corrections to the cross section calculation involve the resolved parton one-loop q$\bar{\rm q}\gamma$ and bremsstrahlung q$\bar{\rm q}\gamma g$ matrix elements, the complete cross section now depends on α_s.

In an analogous manner to the 1-jet + photon case, the $\mathcal{O}\left(\alpha\alpha_S\right)$ matrix element predictions for the 2- and 3-jet + photon rates were compared with the data by integrating the differential cross section from $z_\gamma = 0.95$ to $z_\gamma = 1$, ensuring that any 'smearing' of the $z_\gamma \sim 1$ component was also taken into account. Figure 5.4 shows this comparison where an $\alpha_s(M_{Z^0}^2)$ value of 0.12 (the current LEP average value [42]) was used in the matrix element calculation. At lower $y_{\rm cut}$ values, the agreement is not good: the 2-jet + photon rate is over-estimated, whilst the predicted 3-jet + photon rate is well below that observed in the data. However, since the matrix element calculations are to first order in α_s, the effective value of the strong coupling constant need not necessarily be the same as that obtained from measurements of quantities calculated to second order in α_s or with resummed calculations.

To determine a more suitable value of α_s to substitute in the calculation, the relative 2- and 3-jet + photon rates were studied. The ratio

$$R_3^\gamma = \frac{\sigma(3\ {\rm jet} + \gamma)}{\sigma(2\ {\rm jet} + \gamma) + \sigma(3\ {\rm jet} + \gamma)}$$

is a measure of the first order α_s relevant for this work and is independent of the total cross section. Using a $y_{\rm cut}$ value of 0.01, the value of R_3^γ measured in the data is 0.166 ± 0.025. Table 5.1 lists the values obtained from the matrix element calculation as a function of α_s.
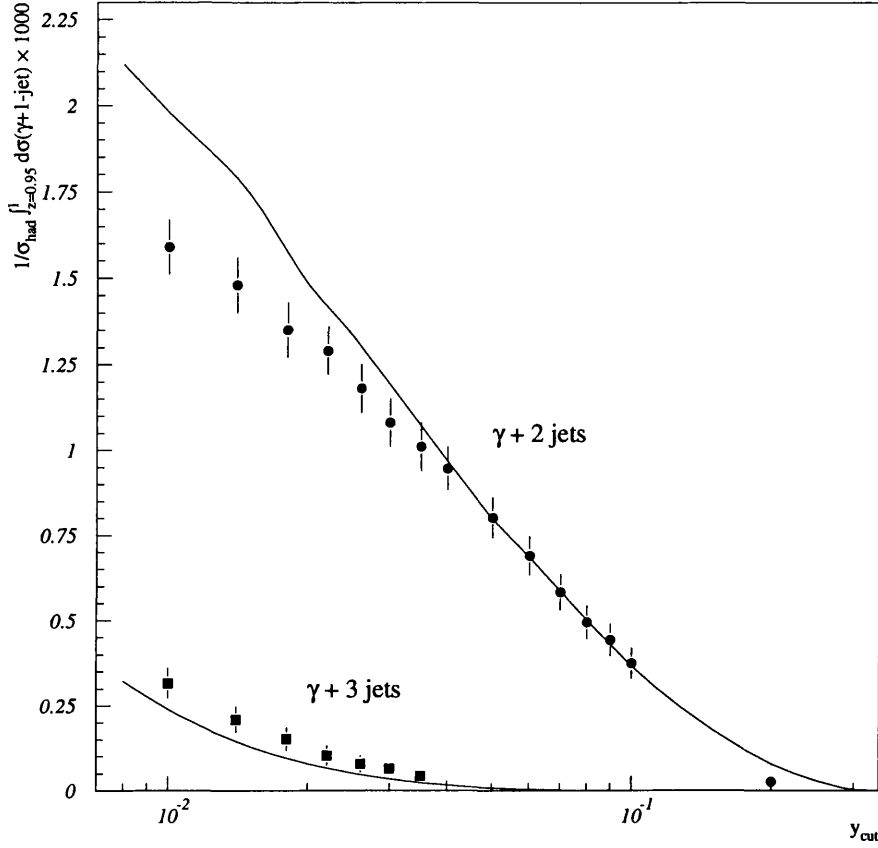
Figure 5.4: The photon + 2- and 3-jets rates showing the $\mathcal{O}\left(\alpha\alpha_S\right)$ prediction using a value of $\alpha_S = 0.120$

Using an α_s value of 0.17 in the matrix element calculation gives much better agreement with the measured photon + jet rates (Figure 5.5). This value of α_s is in agreement with values found by the OPAL and L3 collaborations when determining the electroweak coupling constants of quarks using the method outlined in Chapter 1 [19] and that obtained by the OPAL collaboration in a fit to the jet rates in hadronic events [43]. The higher α_s value is effectively compensating for the missing higher order contributions to the matrix element calculation and other scheme-dependent factors [44], suggesting that the $\mathcal{O}\left(\alpha\alpha_S\right)$ matrix element calculation really is modelling the isolated photon production well.
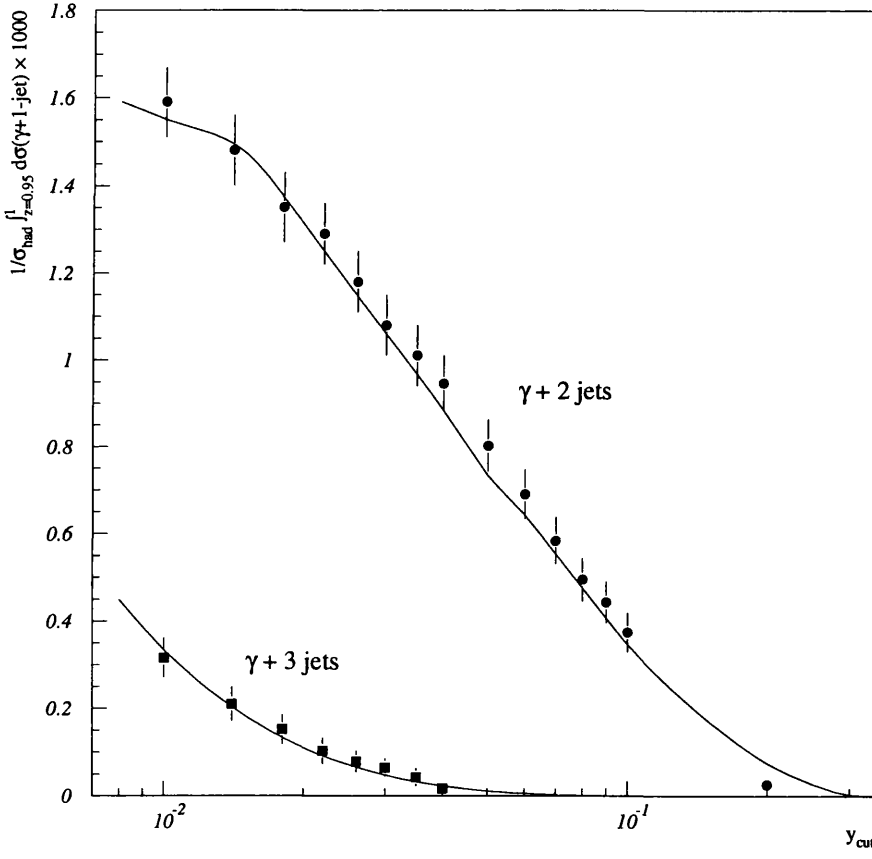
Figure 5.5: The photon + 2- and 3-jets rates compared to an $\mathcal{O}\left(\alpha\alpha_S\right)$ prediction obtained using the 'first order' strong coupling constant, $\alpha_S = 0.170$

5.3   Comparisons With Parton Shower Models

As discussed in Chapter 1, several different models exist which attempt to describe the production of hadronic events. These models have many parameters whose values are fixed by 'tuning' them to give a good description of measured event shape variables and particle production rates. Since the processes of photon and gluon emission from quarks are so similar, once the hadronic model has been fixed there is virtually no freedom to adjust the photon production rate. Whereas the hadronic distributions sum over the quark and gluon contributions, photons probe specifically the quark evolution. Thus comparing the predicted photon production rates from the various models with those measured in the data provides a good test of how best to model the parton evolution mechanism.

Figure 5.6 shows the photon + 1, 2 and 3-jet rates obtained at various y_{cut} values using a z_{cut} of 0.99 compared with predictions from three parton shower Monte Carlo programs. In the photon + 1-jet case, ARIADNE describes the data reasonably well, but HERWIG and JETSET do not. All three models under-estimate the photon + 2-jet rate, although HERWIG and ARIADNE are considerably better than JETSET . All three models describe the photon + 3-jet rate reasonably well, but the large statistical errors on the data make it difficult to draw any conclusions.

5.4   Comparisons With Previous Analyses

As has already been mentioned, the 'democratic' photon isolation method was introduced to remove ambiguities in matching the phase space definitions between the theoretical calculations and the experimental measurements. Good agreement has been found between an $\mathcal{O}\left(\alpha\alpha_s\right)$ matrix element calculation and the experimental data for each event topology, unlike the previous analyses where large discrepancies were observed, particularly in the photon + 1-jet case.

This can be illustrated further by considering the total photon + jets rate. Figure 5.7 shows this as a function of y_{cut} with the corresponding $\mathcal{O}\left(\alpha\alpha_s\right)$ matrix element prediction using α_s values of 0.12 and 0.17. The agreement with the $\alpha_s = 0.17$ prediction is
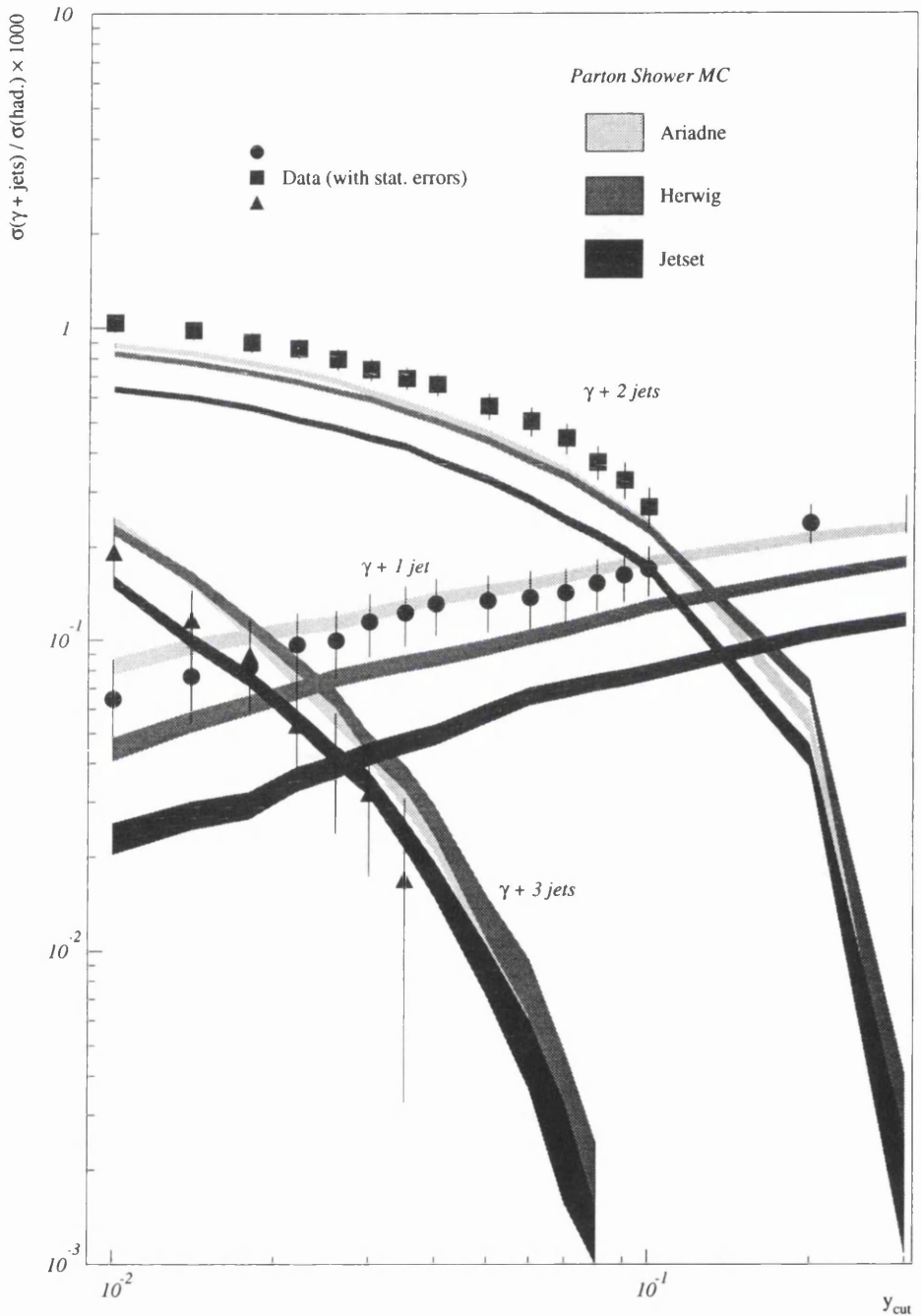
Figure 5.6: The photon + 1, 2 and 3-jet rates over a range of y_{cut} values, using a photon z_{cut} of 0.99, with predictions from parton shower models. The shaded bands represent the statistical errors on the model predictions
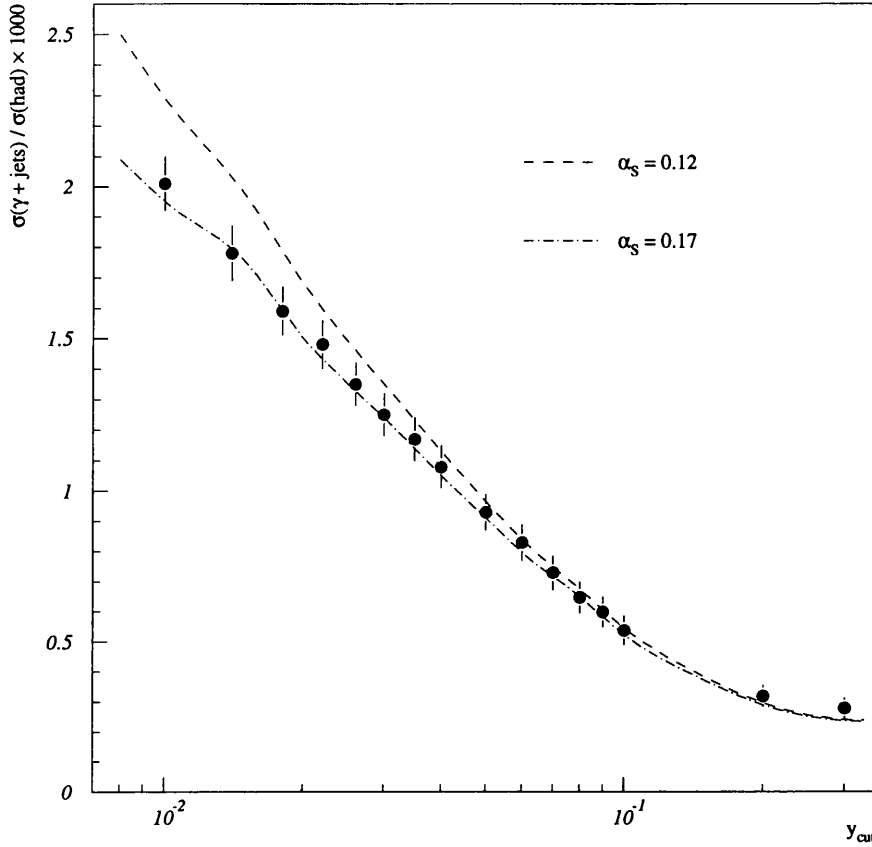
Figure 5.7: The total photon + jets rate as a function of y_{cut} compared with predictions from an $\mathcal{O}(\alpha\alpha_S)$ matrix element calculation at $\alpha_s = 0.12$ and $\alpha_s = 0.17$. Photon isolation was performed using the 'democratic' algorithm with a $z_{cut} = 0.95$.

good over the full range of y_{cut} values. An equivalent comparison with several $\mathcal{O}(\alpha\alpha_S)$ matrix element calculations using the 2-step 'cone' algorithm is shown in Figure 5.8 (taken from Reference [17]). Particularly at lower y_{cut} values the agreement is very poor, showing clearly the merits of using the democratic approach.

Figures 5.9 and 5.10 compare the total rates predicted by parton shower Monte Carlo models with those measured in the data as a function of y_{cut} using both the democratic and cone isolation methods respectively (where Figure 5.10 was taken from Reference [17]). The overall trends in the models are seen to be consistent between schemes, with ARIADNE predicting more photon + jets events than HERWIG which in turn predicts more than JETSET. The agreement with the data, however, is not

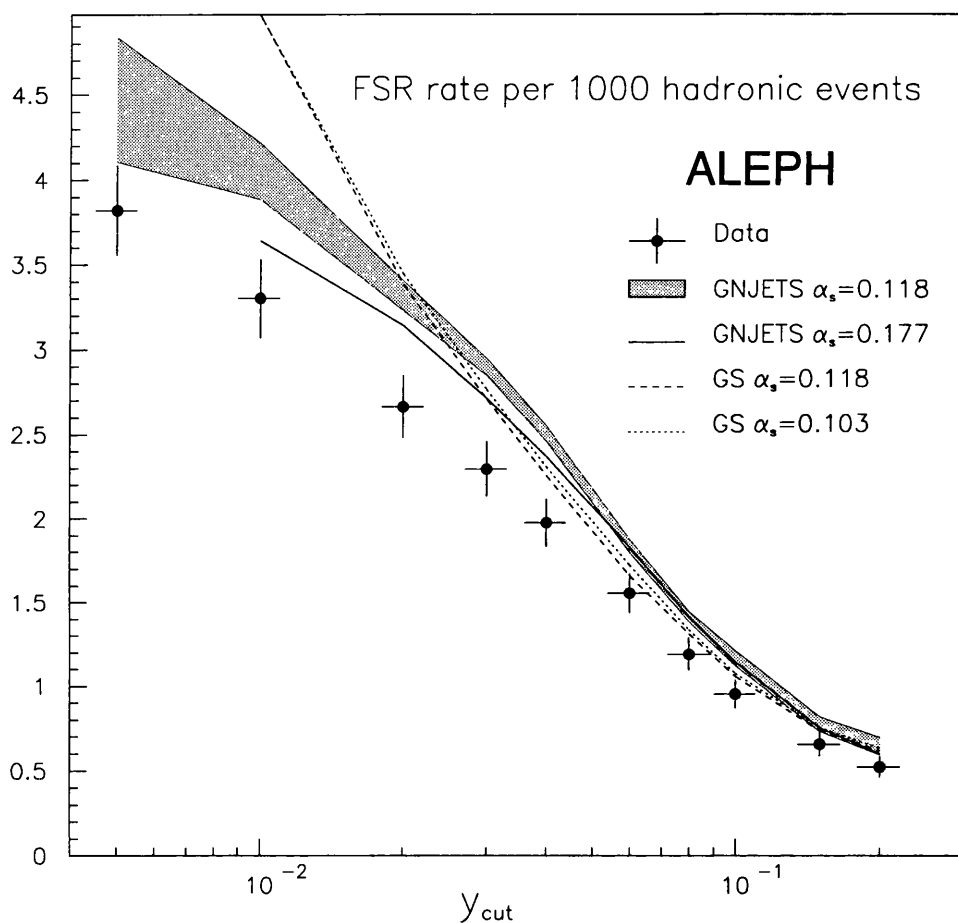Figure 5.8: The total photon + jets rate as a function of y_{cut} compared with predictions from various $\mathcal{O}\left(\alpha\alpha_S\right)$ matrix element calculations using the 'cone' isolation algorithm. GNJETS is the Monte Carlo model based on the matrix element calculation by Kramer & Spiesberger [16]; GS is the 'cone algorithm' Monte Carlo implementation of the calculation by Glover & Stirling [15].

consistent: using the democratic scheme, ARIADNE predicts the total rate rather well whilst JETSET and HERWIG underestimate it, but with the cone algorithm both ARIADNE and HERWIG overestimate the data with JETSET underestimating it.

5.5 Summary

The 'democratic' photon isolation algorithm has been applied to select *isolated* photons in hadronic events, as opposed to those embedded within jets of hadrons. To allow comparisons to be made with predictions from a QCD matrix element calculation, it was necessary to study the integrated cross section, from $z_\gamma = 0.95$ to $z_\gamma = 1$ since a smearing effect due to a misassociation of soft hadrons during jet clustering was observed in the $0.95 < z_\gamma \leq 0.99$ range. Unlike previous analyses which used the two-step cone isolation algorithm, good agreement was found between the measured 1-jet + photon rate and that predicted by an $\mathcal{O}(\alpha\alpha_S)$ calculation. Good agreement between the data and predictions for the photon + 2- and 3-jet rates was also observed, after substituting a value of $\alpha_S(M_Z^2) = 0.17$ into the matrix element calculation to compensate for the missing higher order terms.

Although good agreement was found between the theoretical calculation of the photon + jet rates, no attempt was made to measure the electroweak couplings of u- and d-type quarks to the Z^0 boson. The precision now currently achievable by tagging heavy flavour decays of the Z^0 and subsequently measuring the decay widths $\Gamma(Z^0 \to b\bar{b})$ and $\Gamma(Z^0 \to c\bar{c})$, < 2% and ~ 8% respectively [47, 48], means that the corresponding results quoted in Reference [19] (with precisions of 19% and 10%) from isolated photon production are not competitive.

Comparisons were also made with parton shower Monte Carlo models. None of the models was seen to describe the individual jet rates satisfactorily, but ARIADNE did predict the *total* isolated photon + jet rate well.

Figure 5.9: The total photon + jets rate as a function of y_{cut} compared with predictions from three parton shower Monte Carlo models. Photons were isolated using the democratic algorithm.

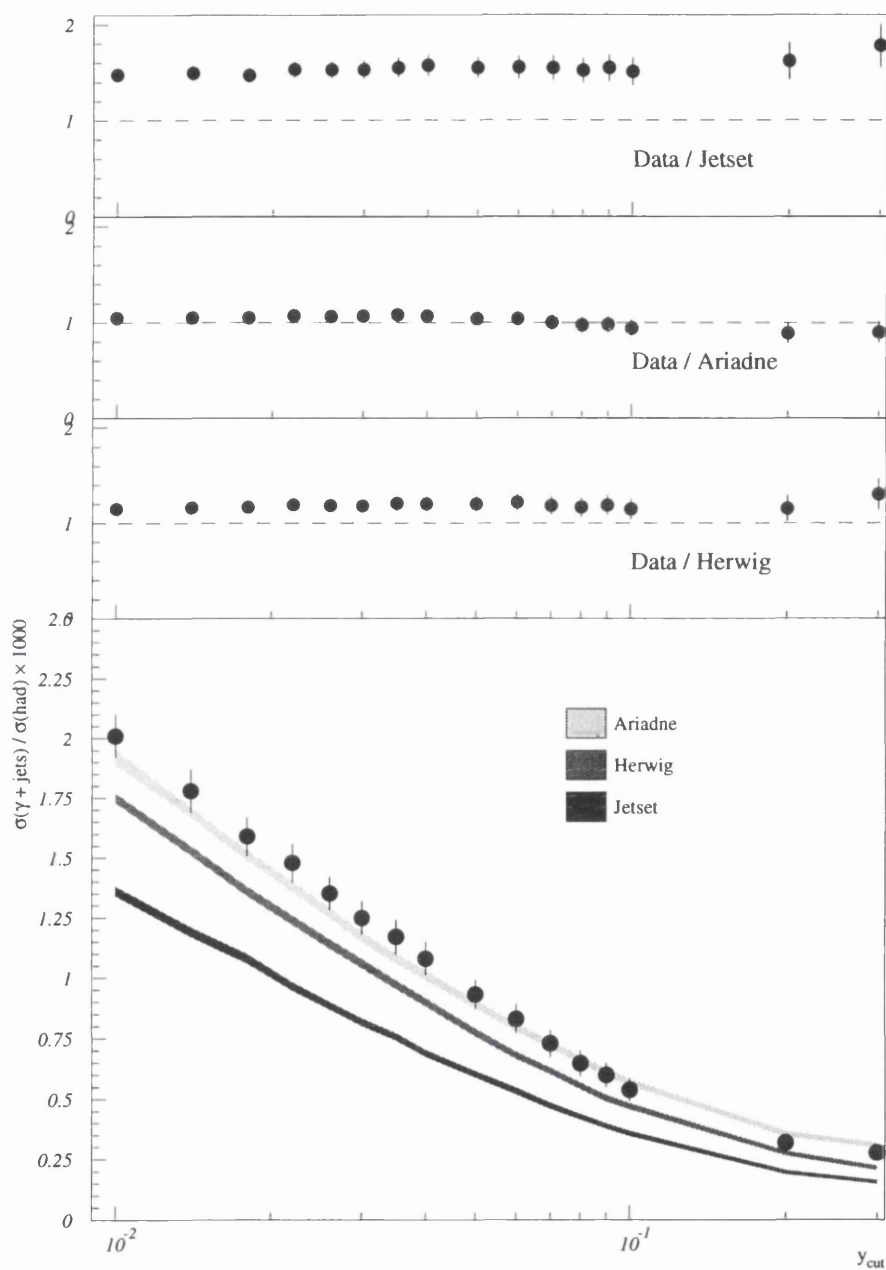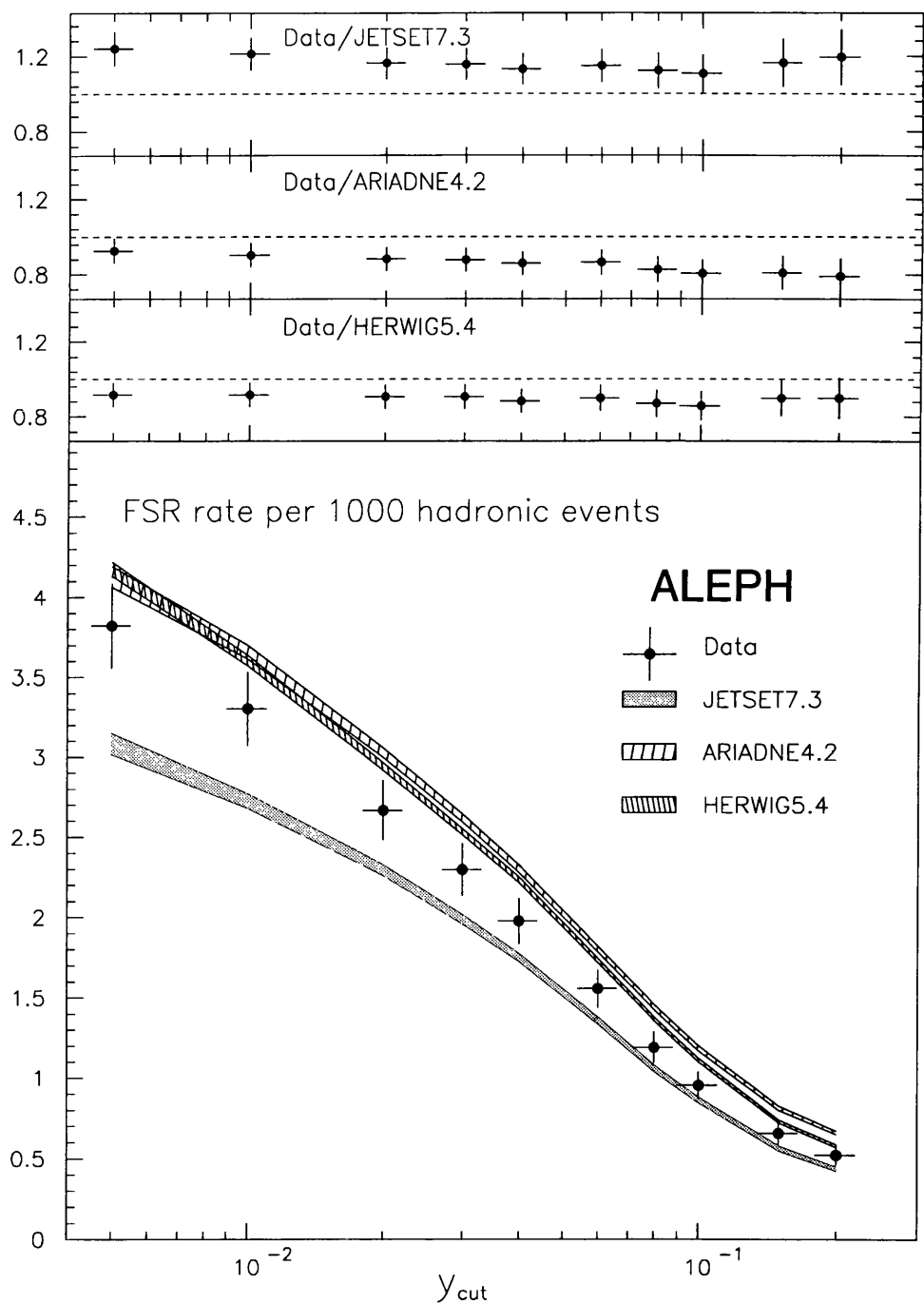Figure 5.10: The total photon + jets rate as a function of y_{cut} compared with predictions from three parton shower Monte Carlo models. Photons were isolated using the cone algorithm.

Chapter 6

Fragmentation in Events Containing an Isolated Photon

6.1 Introduction

Some recent studies of hadronic events at LEP have been aimed at 'tuning' parton shower Monte Carlo models to describe correctly the event shape variables and inclusive particle production rates observed in the data [45, 46]. The tuned models have then been used to generate events at lower centre of mass energies and the predictions compared with data taken at other, lower energy experiments, resulting in plots such as those shown in Figure 6.1 (taken from Ref. [45]; the variable thrust, sphericity and aplanarity are defined in Section 6.2). It was thus possible to examine how well the models are able to explain the variation of event properties over a wide e^+e^- centre of mass energy range from 14 to 91 GeV.

Isolated photons in hadronic events are usually radiated by quarks during the early stages of a parton shower, before any hadronisation effects begin [14]. Such photons, carrying no colour charge, play no part in the subsequent fragmentation process and emerge from the event essentially unchanged from their creation. Energy and momentum conservation imply that the energy available to produce the hadronic final state in these events is less than in events which do not comprise an isolated photon. Comparing the hadronic part of such events with parton shower model predictions offers
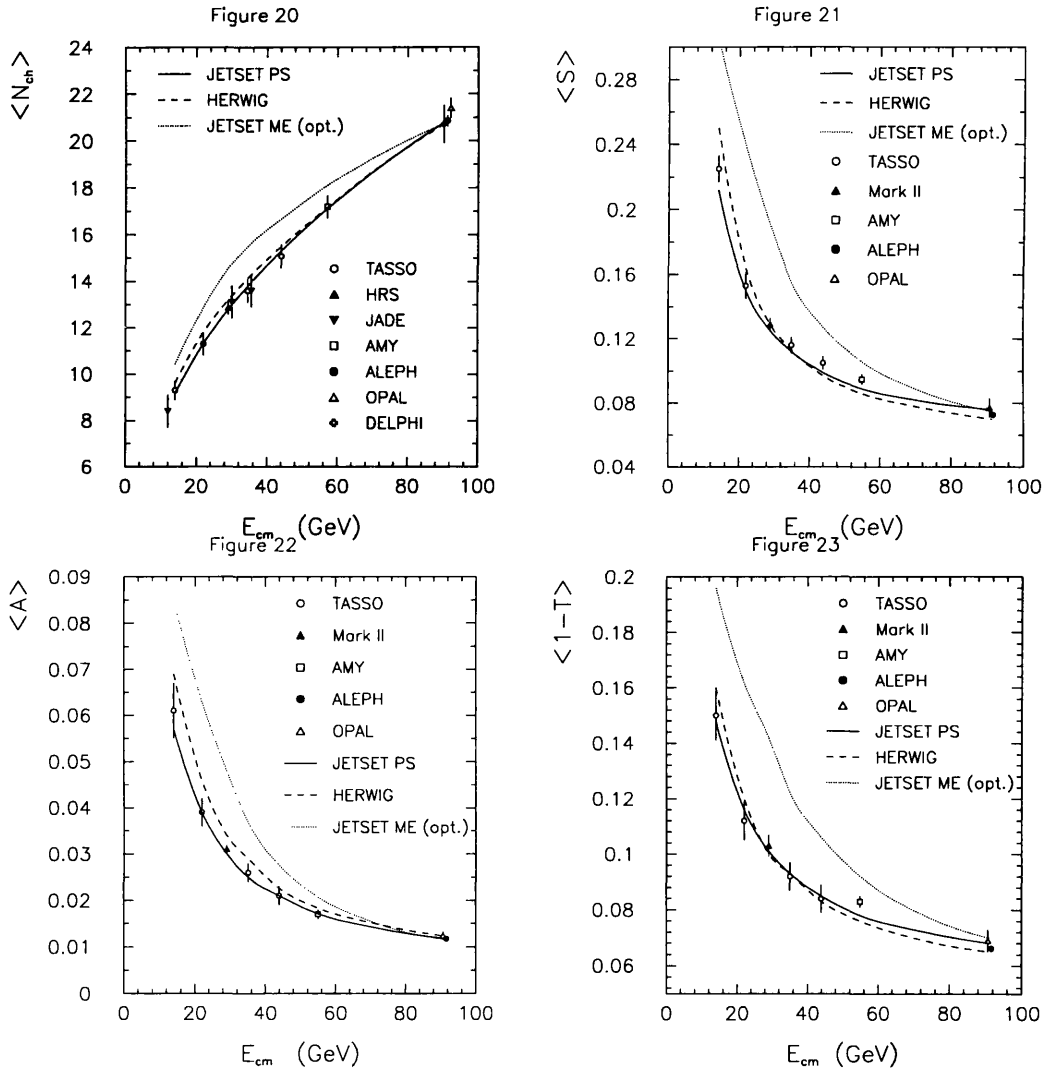
Figure 6.1: Predictions for the mean charged particle multiplicity, sphericity, aplanarity and (1 – thrust) from some Monte Carlo models ('tuned' at 91 GeV) compared with data taken at LEP and from other e^+e^- colliders operating at lower centre-of-mass energies (taken from Ref. [45].

an alternative possibility to test the energy dependence of hadronisation models, with the advantage that all the data are taken using the *same* apparatus.

Specifically, if the Z^0 is produced at rest in the detector, it has 4-momentum $(M_Z, \vec{0})$. If a photon is subsequently radiated with 4-momentum $(E_\gamma, \vec{p}_\gamma)$ then the remaining hadrons must have a 4-momentum of $(M_Z - E_\gamma, -\vec{p}_\gamma)$. In the centre of mass frame of the hadrons, the hadronic 4-momentum is $(E_{had}, \vec{0})$. Equating the invariant mass of the hadronic system in the detector and hadronic c.m. frames, one obtains

$$
\begin{aligned}
E_{had}^2 &= (M_Z - E_\gamma)^2 - \vec{p}^2 \\
&= M_Z(M_Z - 2E_\gamma).
\end{aligned}
$$

For $0 \le E_\gamma \le M_Z/2$, one obtains $0 \le E_{had} \le M_Z$. Thus by boosting into the centre of mass frame of the hadronic system in events containing an isolated photon, it is possible to study hadronic systems over a large range of centre of mass energies.

6.2 Centre of Mass Energy Dependence of Hadronic Systems

To study the properties of hadronic systems at various energies, the four variables illustrated in Figure 6.1 were used: namely, the average multiplicity of charged particles, the average sphericity, the average planarity and the average (1 − thrust). Sphericity $S = 3(Q_1 + Q_2)/2$ and aplanarity $A = 3/2Q_1$ are computed from the eigenvalues $Q_1 < Q_2 < Q_3$ of the normalised 3×3 sphericity tensor $M_{\alpha\beta} = \sum_i p_{i\alpha} \cdot p_{i\beta} / \sum_i p_i^2$, where α, β denote the x,y,z momentum components of particle i. The thrust value is defined as

$$
T = \max\left(\frac{\sum_i |\vec{p}_i \cdot \vec{n}|}{\sum_i |\vec{p}_i|}\right)
$$

where $\vec{n}$ is the thrust axis.

Events comprising an isolated photon were selected using the democratic method, jet clustering being performed with the 'Durham' algorithm ($y_{cut} = 0.001$) and a photon z_{cut} of 0.99. A low y_{cut} and high z_{cut} combination was chosen to maximise the number

of selected events, whilst keeping the contamination from non-FSR backgrounds low. Figure 6.2 shows the comparison between the data and predictions from three parton shower models (JETSET 7.3, ARIADNE 4.1 and HERWIG 5.6). All quantities, except the average charged particle multiplicity, exhibit a decrease with increasing hadronic centre of mass energy. This is expected since the jets of the dominant 2-jet structure become narrower as the initiating quark and anti-quark become more energetic, and the strong coupling constant α_s decreases with increasing energy. The average multiplicity of charged particles increases with increasing energy since more energy is available to create hadrons. The agreement between the data and the models is good, although the statistical errors are large.

Figure 6.3 shows the same data points as Figure 6.2 but the Monte Carlo model predictions were obtained by generating events at lower centre of mass energies using the parameter values 'tuned' at 91 GeV. Although the models give a good description of the mean charged particle multiplicity, they do not predict the three other quantities so well. The open points in Figure 6.3 are predictions from HERWIG where the Z^0 was forced to decay only to u- and c-type quarks, as events containing an isolated photon are predominantly of this type. These points do not differ significantly from those obtained using the full five-flavour sample.

Since it is the predictions for the event shape-type variables which disagree with the data but not those for the average charged particle multiplicities (which should depend only on the available rest-mass), it would appear that by radiating a photon the partons are disturbed to the extent that the remaining hadronic system can no longer be described analogously to an $e^+e^- \rightarrow$ hadrons event at a lower centre of mass energy. This may be because the hadronic system in $Z^0 \rightarrow \gamma +$ hadrons events is more analogous to a hadronic system produced in a $\gamma\gamma$ collision than in a purely hadronic Z^0 decay, since the $Z^0 - \gamma$ coupling is not point-like. This is illustrated schematically in Figure 6.4. Unfortunately, the hadronic events arising from the process shown in Figure 6.4(c) tend not to be well contained in the detector, making a comparable analysis difficult.
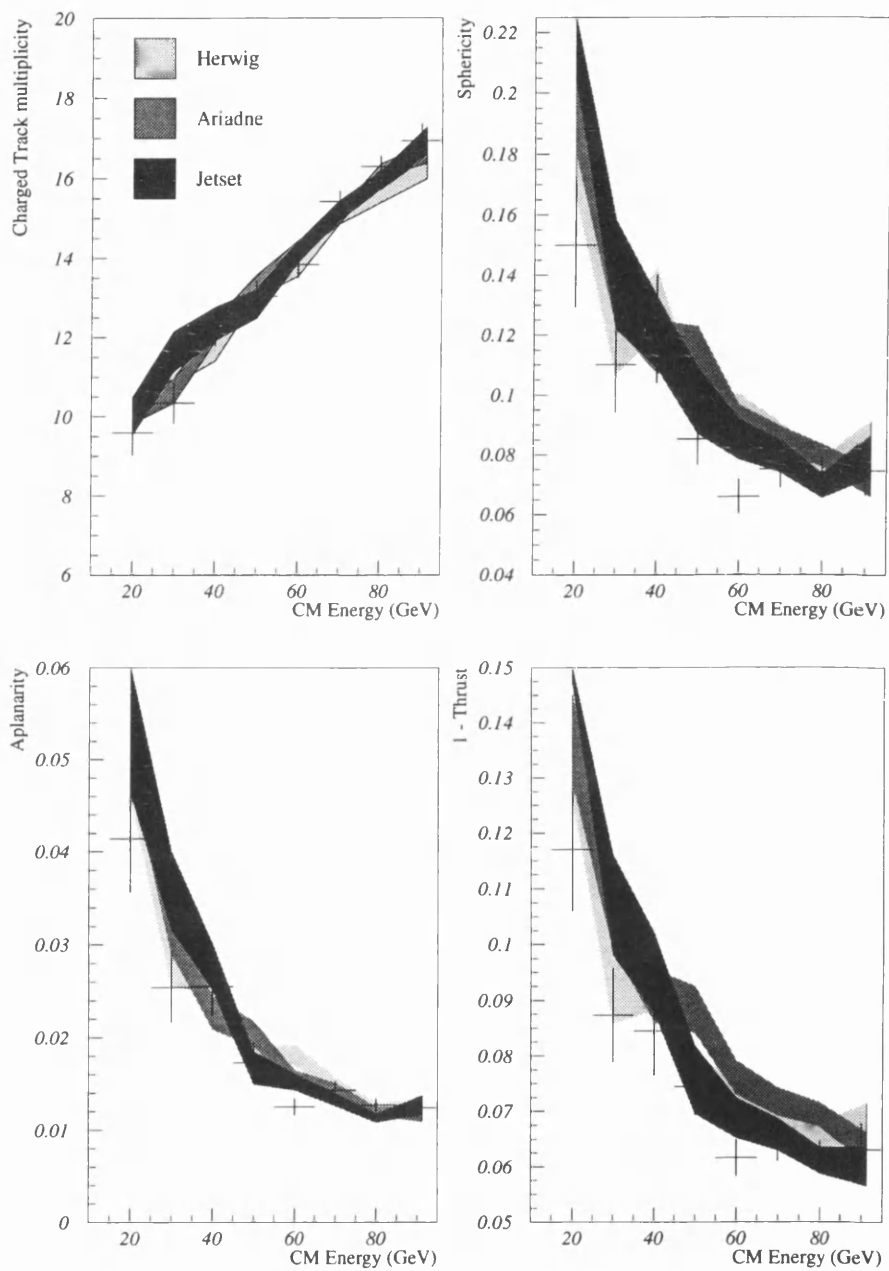
Figure 6.2: Comparison between data and parton shower models for various quantities over a range of hadronic centre of mass energies. In all cases the hadronic system is obtained from events comprising an isolated photon.
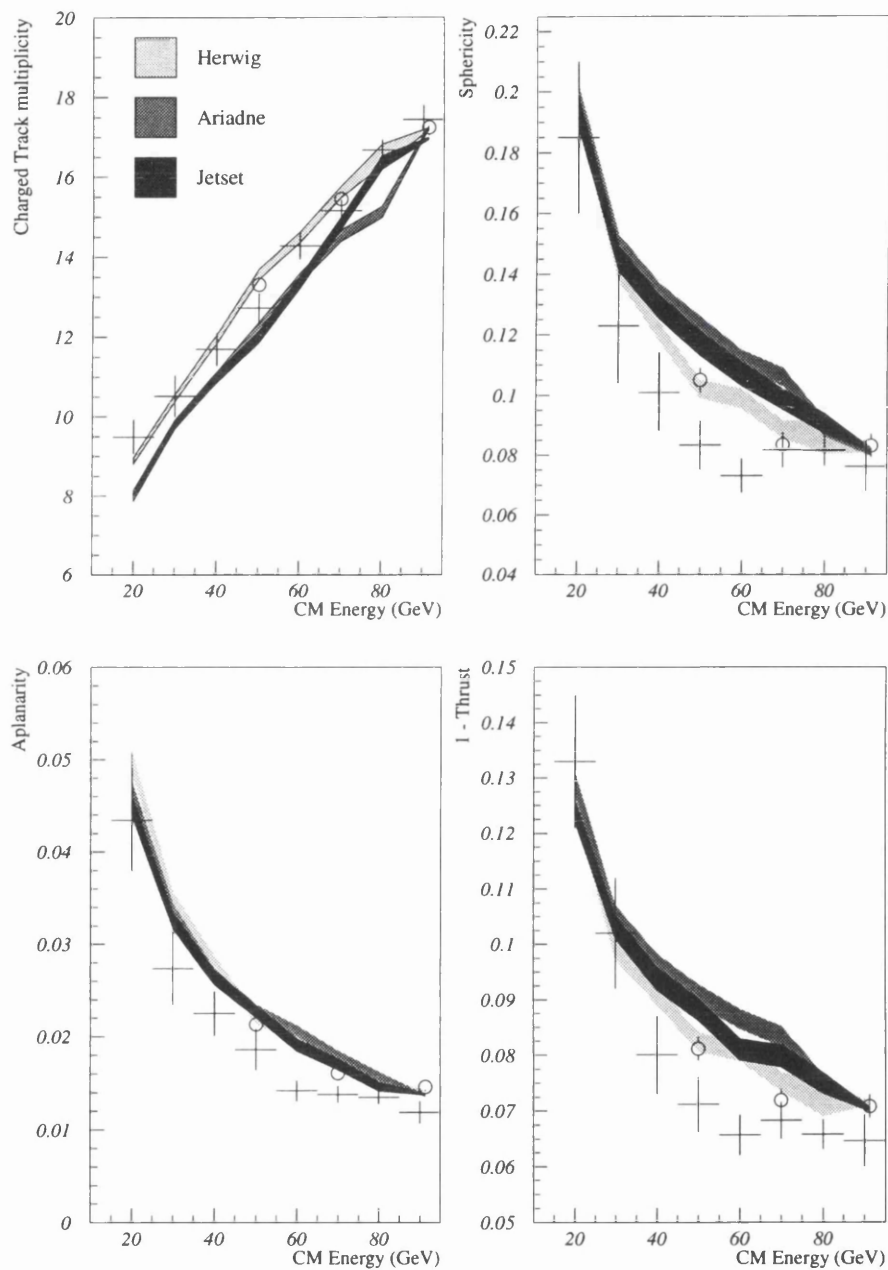
Figure 6.3: Comparison between data and parton shower models for various quantities over a range of hadronic centre of mass energies. In the case of the data, the hadronic system is obtained from events comprising an isolated photon, but the Monte Carlo events were generated at the given c.m. energy. The open points represent Herwig events comprising only u and c type quarks.

Figure 6.4: Some production mechanisms for hadronic final states: (a) Purely hadronic Z^0 decay; (b) $Z^0 \to \gamma +$ hadrons; (c) $\gamma\gamma \to$ hadrons

Chapter 7

Summary and Conclusions

7.1 Measurement of the Quark to Photon Fragmentation Function

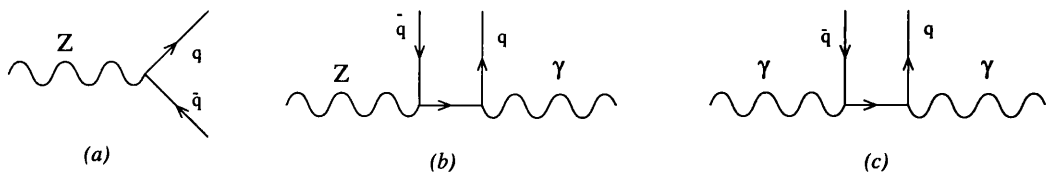Previous analyses of photon emission in hadronic events [17, 18] looked only at *isolated* photon production, the photons being accompanied by essentially no hadronic energy. This was thought necessary to keep the dominant background from energetic π^0 decays into two overlapping photons manageable, since π^0's are usually accompanied by additional hadronic debris. Comparisons were made with predictions from various parton shower Monte Carlo models, with the hope of gaining some insight into the parton evolution mechanism. Comparisons with $\mathcal{O}\left(\alpha\alpha_S\right)$ matrix element calculations were complicated by ambiguities in matching the phase space definitions between theory and experiment, a consequence of the elaborate two-step photon isolation algorithm which was used. However, many features of the data were well described by the calculations, giving confidence that the process was well measured and understood.

It was recently suggested [33] that a safer approach would be to cluster 'democratically' *all* the particles in an event into jets, then look for photons possessing a substantial fraction of their associated jet's energy. Assuming local parton–hadron duality, the jets of particles can be mapped onto the partons of the matrix element calculation, removing any phase space matching ambiguities. However, by allowing hadronic energy to accompany the photon, the perturbatively divergent possibility that

the photon was radiated collinearly from a quark is introduced. This is expected to happen only at late times, so that in practice the quark has already hadronised and this final state collinear divergence can be regularised and subsequently factorised into a perturbative component and a non-perturbative quark to photon fragmentation function, $D_{q \to \gamma}$. Given that there is no $e^+ e^- \to \gamma + 1$ parton process, the first non-trivial contributions to the photon + 1-jet rate come from $e^+ e^- \to q\bar{q}\gamma$ and $e^+ e^- \to q\bar{q}$, where one of the quarks fragments, producing a photon. The photon + 1-jet rate is thus especially sensitive to $D_{q \to \gamma}$.

Selecting photons accompanied by hadronic energy introduces a large background from energetic $\pi^0 \to \gamma\gamma$ decays where the photon clusters overlap in the electromagnetic calorimeter, particularly in the 1-jet + photon case. After checking that the JETSET Monte Carlo model, which had previously been tuned to describe various measured event shape variables and charged particle production rates, gave an accurate description of the energetic π^0 production rate, the non-FSR background in the selected sample was estimated and subtracted statistically in bins of z_γ. The measured photon + jet rates were then corrected for incomplete geometrical acceptance, reconstruction inefficiencies and photon conversion losses.

Working to $\mathcal{O}(\alpha\alpha_S)$ within the formalism of the $\overline{\text{MS}}$ renormalisation scheme , an analytical form for $D_{q \to \gamma}$ cannot be derived, although its evolution in terms of μ_F, an unphysical scale which divides the perturbative and non-perturbative contributions, is known. The simplest form for $D_{q \to \gamma}$ which satisfies this evolution equation, whilst simultaneously cancelling any unphysical singularities in the perturbative contribution and removing any overall dependence on μ_F from the cross section is given by

$$D_{q \to \gamma}(z, \mu_F) = \left(\frac{\alpha e_q^2}{2\pi} \right) \frac{1 + (1 - z)^2}{z} \log \left(\frac{\mu_F^2}{\mu_0^2 (1 - z)^2} \right) + B$$

where B fixes the initial value of D when $\mu_F = \mu_0$. With μ_F fixed at a value of $10 \, \text{GeV}$, a χ^2 minimisation fit was performed to the data over the range $0.7 \le z_\gamma \le 0.95$, where μ_0 and B were free parameters. The minimum χ^2 was found with $\mu_0 = 0.20 \pm 0.25 \, \text{GeV}$ and $B = -12.4 \pm 2.95$. This result was found to be valid over a large range of y_{cut} values.

7.2   Isolated Photon Production

To test the $\mathcal{O}\left(\alpha\alpha_S\right)$ matrix element calculation predictions for isolated photon produc-
tion, which in the case of one-jet + photon events depends only on the electroweak
quark couplings and not on α_S, the previously measured quark to photon fragmentation
function was extrapolated from $z_\gamma = 0.95$ to $z_\gamma = 1$. The data, however, showed
evidence that a fraction of the isolated photon component ($z_\gamma > 0.99$) was populating
the $0.95 \leq z_\gamma \leq 0.99$ bin. A study of the resulting z_γ of FSR photons before and
after hadronisation using a parton shower model showed that this 'smearing' effect
was due to misassociation of soft hadrons with the 'photon jet' during jet clustering.
To overcome this, the integrated rate from $z_\gamma = 0.95$ to $z_\gamma = 1$ was compared with
the corresponding prediction, although this introduced a contribution from the frag-
mentation component. In general, good agreement was found between the data and
the matrix element calculation, indicating that the 'democratic' algorithm has indeed
removed the difficulties in matching the phase space definitions between theory and
experiment inherent in the previous cone-based algorithms.

In the case of events comprising an isolated photon plus two or more hadronic jets,
the fragmentation component does not contribute to the cross section at lowest order,
but only appears at next to leading order. The dominant contribution is therefore from
isolated photon production. As for the 1-jet + photon events, the integrated rate from
$z_\gamma = 0.95$ to $z_\gamma = 1$ was compared with the equivalent matrix element predictions.
Using a value of $\alpha_S = 0.12$, the matrix element prediction over-estimated the rate of
2-jet + photon events, and under-estimated the 3-jet + photon rate. Increasing α_S to
0.17 resulted in much better agreement, suggesting that the larger α_S value is effectively
compensating for missing higher order terms in the $\mathcal{O}\left(\alpha\alpha_S\right)$ cross section calculation.

Similar comparisons were also made with the parton shower models JETSET, HER-
WIG and ARIADNE. In the case of events comprising an isolated photon plus one
hadronic jet, ARIADNE was in good agreement with the data over a wide range of y_{cut}
values, but HERWIG and JETSET underestimated the rate considerably. All three models
underestimated the 2-jet + photon rate, although the ARIADNE and HERWIG predictions
were somewhat better than JETSET. The 3-jet + photon rate was well described by all

three models, but the low statistics make a comparison between the models difficult. ARIADNE also gave the best agreement with the total photon + jets rate. A possible explanation for the apparently better agreement of ARIADNE compared to JETSET and HERWIG may lie in the fact that both JETSET and HERWIG employ a parton shower model to generate a set of partons which are subsequently hadronised, but ARIADNE uses a model based on radiating dipoles to generate the partons. The probability of parton radiation in the dipole model is calculated from exact first order matrix elements which are equivalent to the Altarelli–Parisi splitting functions used in the parton shower models only in the limit where one parton retains its energy.

Although the ambiguities in matching the phase-space definitions between theory and experiment appear to have been resolved through the use of the democratic algorithm, no attempt was made to measure the electroweak couplings of u- and d-type quarks to the Z^0 boson. The precision now currently achievable by tagging heavy flavour decays of the Z^0 and subsequently measuring $\Gamma_{b\bar{b}}$ and $\Gamma_{c\bar{c}}$ ($< 2\%$ and $\sim 8\%$, respectively [47, 48]) means that the results quoted in Reference [19] (with precisions of 19% and 10%) obtained from measurements of isolated photon production are not competitive.

7.3 Hadronisation in Events Including an Isolated Photon

Isolated photons in hadronic events are generally radiated during the early stages of the parton evolution, taking no further part in the subsequent hadronisation process. They thus have the effect of removing energy from the partons, with the result that the hadronic system is produced at a lower energy than would otherwise have been the case. Comparisons of some event variables measured in the hadronic centre of mass frame of events comprising an isolated photon with equivalent predictions from some parton shower models show good agreement over a range of hadronic centre of mass energies. Similar comparisons using simulated events generated at lower centre of mass energies show good agreement for the mean charged particle multiplicity, which

depends only on the energy available to produce hadrons, but event shape variables are not in such good agreement. The hadronic system in events containing an isolated photon attributable to quark bremsstrahlung cannot therefore be described analogously to hadronic events produced at lower centre of mass energies.

7.4   Possible Future Developments

As was illustrated in Chapter 1 of this thesis, there is currently a large discrepancy between the inclusive prompt photon production rate measured at hadron-hadron colliders and the rates predicted from next-to-leading order QCD calculations, particularly when the photon has a low transverse momentum (Figures 1.4 and 1.5). It would be interesting to see if including the quark-to-photon fragmentation function measured in Chapter 4 in the calculations could reduce this discrepancy.

As more data are collected with the ALEPH detector (after the end of the 1994 data taking period, almost 4 million Z^0 decays will have been collected in all — almost four times the sample used in the present analysis), a measurement of the quark coupling constants from the $Z^0 \to$ hadrons and $Z^0 \to$ hadrons $+ \gamma$ cross sections, as described in Chapter 1, may become interesting, as might a measurement of the $Z^0 \to b\bar{b}\gamma$ cross section. A significant discrepancy between the latter quantity and its standard model prediction could be evidence for decays of the Z^0 into a Higgs boson and a photon

$$e^+ e^- \to Z^0 \to h\gamma$$

where the h subsequently decays into $b\bar{b}$.

As described in Chapter 5, the 2-jet + photon rate is dominated by the lowest order contribution to the cross section which occurs at $z_\gamma \sim 1$. However, the fragmentation function contribution comes from the lowest order $e^+ e^- \to q\bar{q}g$ process which is potentially sensitive to the gluon fragmentation function. A measurement of the non-perturbative component of this, $D_{g \to \gamma}(z, \mu_F)$ may be used as input to other calculations, in much the same way as the quark-to-photon fragmentation function.

References

[1] The LEP Collaborations; Preprint CERN/PPE/93-157

[2] F. Abe *et al*; Fermilab–Pub–94-097-E (April 1994), Submitted to Phys. Rev. D

[3] G. Arnison *et al* (UA-1 collab.); Phys Lett. **122B** (1983) 103
M. Banner *et al* (UA-2 collab.); Phys Lett. **122B** (1983) 476

[4] S. Glashow; Nuc. Phys. **22** (1961) 579
A. Salam; in *'Elementary Particle Theory'*, W. Svartholm *(editor)*, Almquist and Wiksell, Stockholm, 1968
S.Weinberg; Phys. Rev. Lett. **19** (1967) 1264.

[5] see *Z Physics at LEP 1, Vol. 3*, ed. G. Altarelli *et al*; CERN 89–08 (Vol. 3)

[6] Ya.I. Azimov *et al*; Phys. Lett. **B165** (1985) 147

[7] A. Krzywicki & B. Petersson; Phys. Rev. **D6** (1972) 924
J. Finkelstein & R.D. Peccei; Phys. Rev. **D6** (1972) 2606
F. Niedermayer; Nucl. Phys. **B79** (1974) 355
A. Casher *et al*; Phys. Rev. **D10** (1974) 732

[8] R.D. Field & R.P. Feynman; Nuc. Phys. **B136** (1978) 1

[9] B. Andersson *et al*; Physics Reports **97** (1983) 31
X. Artru; Physics Reports **97** (1983) 147

[10] B.R. Webber; Nucl. Phys. **B238** (1984) 492
G. Marchesini & B.R. Webber; Nucl. Phys. **B310** (1988) 461

[11] T. Sjöstrand; Comp. Phys. Comm. **39** (1986) 347

   T. Sjöstrand & M. Bengtsson; Comp. Phys. Comm. **43** (1987) 367

[12] L. Lönnblad; Comp. Phys. Comm. **71** (1992) 15

[13] G. Marchesini *et al*; Comp. Phys Comm. **67** (1992) 465

[14] E. Laermann, T.F. Walsh, I. Schmidtt & P.M. Zerwas; Nuc. Phys. **B207** (1982) 205.

[15] E.W.N. Glover & W.J. Stirling; Phys. Lett. **B295** (1992) 128

[16] G. Kramer & H. Spiesberger; Preprint DESY 92–022

   M. Glück *et al*; D0–TH 94/02

   Contribution to the 27th International Conference on High Energy Physics, Glasgow (July 1994)

   P. Aurenche *et al*; Nucl. Phys. **B399** (1993) 34

   E.L. Berger & J. Qiu; Phys. Lett. **B248** (1990) 371

[17] D. Buskulic *et al* (ALEPH collab.); Z. Phys. **C57** (1992) 17

[18] P.D. Acton *et al* (OPAL collab.); Z. Phys. **C54** (1992) 193

   P. Abreu *et al* (DELPHI collab.); Z. Phys. **C53** (1992) 555

   O. Adriani *et al* (L3 collab.); Phys. Lett. **B292** (1992) 463

[19] P.D. Acton *et al* (OPAL collab.); Z. Phys. **C58** (1993) 405

   O. Adriani *et al* (L3 collab.); CERN–PPE/92–209

[20] F. Abe *et al* (CDF collab.); Fermilab–Conf–94/148-E

   Contribution to the 27th International Conference on High Energy Physics, Glasgow (July 1994)

[21] S. Myers, *The LEP Collider, From Design to Approval and Commisioning*; CERN 91–08

[22] The ALEPH Handbook, editor W. Blum (1989)

[23] D. Decamp *et al*; Nucl. Instrum. Methods **A294** (1990) 121

[24] H.G. Moser *et al*; Nucl. Instrum. Methods **A315** (1992) 121

[25] E. Iarocci; Nucl. Instrum. Methods **A217** (1983) 30

[26] D. Bédérède *et al*; to be published in Nucl. Instr. Meth. A

[27] B. Bloch; Talk presented at ALEPH plenary meeting, 7th May 1993

[28] A. Belk *et al*; IEEE Trans. Nucl. Sci. **36** No. 5 (1989) 1534

[29] W. von Ruden; Contribution to the Real Time '89 Conference, Williamsburg Virginia (May 1989)

[30] V. Blobel; DESY R1-88-01

[31] J.F. Renardy *et al*; IEEE Trans. Nucl. Sci. **36** No. 5 (1989) 1464

[32] G. Altarelli *et al*; Nucl. Phys. **B160** (1979) 301

[33] E.W.N. Glover & A.G. Morgan; Z. Phys. **C62** (1994) 311

[34] W.T. Giele & E.W.N. Glover; Phys. Rev. **D46** (1992) 1980

[35] W. Furmanski *et al*; Phys. Lett. **B97** (1980) 437
G. Curci *et al*; Nucl. Phys. **B175** (1980) 27

[36] S. Catani *et al*; Phys. Lett. **B269** (1991) 432

[37] N. Brown & W.J. Stirling; Z. Phys. **C53** (1992) 629

[38] P. Reeves; ALEPH collaboration internal note 93–148 (Physics note 93–128)

[39] V. Bertin; Private Communication

[40] Ya.I. Azimov *et al*; Z. Phys. **C27** (1985) 65

[41] E.W.N. Glover & A.G. Morgan; Phys. Lett. **B324** (1994) 487

[42] The LEP collaborations; Conference contribution CERN/PPE/93-157

[43] P.D. Acton *et al* (OPAL collab.); Z. Phys. **C55** (1992) 1

[44] D.T. Barclay, C.J. Maxwell & M.T. Reader; Durham Preprint DTP/93/68

[45] D. Buskulic *et al* (ALEPH collab.); Z. Phys. **C55** (1992) 209

[46] M. Akrawy *et al* (OPAL collab.); Z. Phys. **C47** (1990) 505

[47] D. Buskulic *et al* (ALEPH collab.); Phys. Lett. **B313** (1993) 535

[48] D. Buskulic *et al* (ALEPH collab.); Preprint CERN-PPE/94-017